

**Centrifuge experiments with magmatic systems: from melt segregation
to pluton emplacement**

Dissertation
zur Erlangung des Doktorgrades
der Geowissenschaften

vorgelegt beim Fachbereich Geophysik
der Johann Wolfgang Goethe-Universität
in Frankfurt am Main

von
Mélanie Forien
aus Gien (Frankreich)

Frankfurt am Main, den 25 März 2011

vom Fachbereich Geowissenschaften der
Johann Wolfgang Goethe - Universität als Dissertation angenommen.

Dekan: Prof. Dr. R. Pütz

Gutachter :

1. Prof. Dr. H. Schmeling
2. Prof. Dr. J-L. Vignerese
3. PD. Dr. N. Bagdassarov

Datum der Disputation : 25 März 2011

"[...] la géologie expérimentale a enfin reçu définitivement droit de cité dans la science. Son but, comme on le sait, est d'imiter, par les procédés du laboratoire, les phénomènes géologiques et les produits variés qu'ils ont engendrés dans les diverses régions de l'écorce terrestre. Une foule de problèmes ont déjà été élucidés par son intervention toute-puissante et l'on doit attendre les plus grands progrès de son complet développement."

Stanislas MEUNIER (1843-1925)

Table of contents

ACKNOWLEDGMENTS	9
ABSTRACT.....	11
ABSTRAKT.....	17
RÉSUMÉ	22
INTRODUCTION.....	25
CHAPTER I - PRINCIPLES AND METHODS.....	31
I.1 - PRINCIPLES OF THE MODELING.....	33
<i>I.1.1 - Centripetal and centrifugal force</i>	<i>33</i>
<i>I.1.2 - Sedimentation principle.....</i>	<i>35</i>
I. 2 - CENTRIFUGES	36
<i>I.2.1 - How a centrifuge works technically</i>	<i>36</i>
<i>I.2.2 - Centrifuge used in this study.....</i>	<i>38</i>
CHAPTER II - PLUTON EMPLACEMENT: THE NESTED DIAPIRS.	41
II.1 - INTRODUCTION	43
II.2 - EXPERIMENTAL PROCEDURE.....	44
<i>II.2.1 - Set-up of experiment 1 - without initial perturbations</i>	<i>45</i>
<i>II.2.2 - Set-up of experiment 2.....</i>	<i>45</i>
<i>II.2.3 - Set-up of experiment 3.....</i>	<i>46</i>
<i>II.2.4 - Set-up of experiment 4.....</i>	<i>47</i>
<i>II.2.5 - Set-up of experiment 5.....</i>	<i>47</i>
II.3 - EXPERIMENTAL RUN AND RESULTS OF THE EXPERIMENTS	48
<i>II.3.1 - Experiment 1 - without initial perturbations</i>	<i>48</i>
<i>II.3.2 - Experiment 2</i>	<i>49</i>

II.3.3 - Experiment 3.....	49
II.3.4 - Experiment 4.....	52
II.3.5 - Experiment 5.....	55
II.4 - SUMMARY	55
CHAPTER III - THE SETTLING AND COMPACTION OF OLIVINE.....	59
III.1 - INTRODUCTION	61
III.2 - EXPERIMENTAL AND ANALYTICAL TECHNIQUES	61
III.2.1 - Experimental strategy	61
III.2.2 - Experimental techniques.....	61
III.2.3 - Analytical techniques	63
III.3 - RESULTS	65
III.3.1 - Crystal distribution after static annealing.....	65
III.3.2 - Porosity profiles through the olivine layer.....	65
III.3.3 - Grain growth	72
CHAPTER IV - CRYSTAL - MELT SETTLING IN A MAGMA CHAMBER.....	79
IV.1 - INTRODUCTION.....	81
IV.2 – CENTRIFUGE EXPERIMENTS.....	81
IV.2.1 – Centrifuge furnace	81
IV.2.2 - Sample preparation	82
IV.2.3 - Analytical methods.....	82
IV.2.4 - Results.....	83
IV.3 - NUMERICAL SIMULATION	89
IV.3.1 - General description.....	89
IV.3.2 - Mathematical model.....	91
IV.3.3 - Input parameters.....	93
IV.3.4. Results.....	94

CHAPTER V - DISCUSSION	99
V.2 – EMPLACEMENT OF NESTED DIAPIRS.....	101
V.3 – ORTHO- AND ADCUMULATE TIME FORMATION	104
V.3.1 - <i>Settling velocity in olivine cumulate</i>	104
V.3.2 - <i>Pressure dissolution and precipitation - chemical compaction.....</i>	106
V.3.3 - <i>Formation times of gravitational cumulates in layered intrusions.</i>	109
V.4 - CRYSTAL SETTLING-FLOATING PROCESS IN A MAGMA CHAMBER.....	112
V.4.1 - <i>Structure of centrifuge samples</i>	113
V.4.2 - <i>Compositional trends of the major and trace elements</i> <i>concentrations in the glass layer 1.</i>	114
V.4.3 - <i>Evolution of the compaction</i>	115
V.5 - COMPARISON WITH NATURAL EXAMPLES.....	116
V.5.1 - <i>The Great Kavir</i>	116
V.5.2 - <i>The Odenwald Crystalline Complex</i>	116
V.5.3 - <i>The Muskox intrusion</i>	117
CONCLUSION	123
REFERENCES.....	129
LEBENSLAUF	147

Acknowledgments

I am pleased to thank my PhD supervisors, Nick Bagdassarov and Carlo Dietl, for their patience, their scientific rigor and their help. Moreover, they have given me full freedom and support during the course of my research work, for which I am thankful. That allowed to me to have an autonomy that I have lot of appreciated during my thesis.

I would also like to associate in this acknowledgement, Max Schmidt from ETH Zürich, as well as, Hemin Koyi from Uppsala University to have given me a warm welcome in their respective laboratories. I enjoyed create new contacts, at during these research works, with Paula Ardia, Remco Hin, Lukas Martin, Luca Caricchi, Marion Louvel, Jessica Langlade, Mattia Pistone, and Steffi Burchardt. It was a pleasure to work with these people and to benefit from their knowledge.

Although I have not had the opportunity to meet him, I would like thanks Giulio Solferino for the interesting discussions on compaction of olivine from basaltic melt. Thanks also to Stefan Berres for his collaboration on the crystal settling in magma chamber.

My thanks to Beverley Tkaltec and Mickael Laumonier for providing helpful suggestions for improving this thesis. Any “linguistic crimes” are mine alone.

My thanks to my friends and colleagues Marek Naser, Shuranita Kanjilal, Marcus Beuchert, Guillaume Richard, Meysam Shahraki, Ingo Wölbern, Anne Bublitz, Alexander Löwer, for the great time I had in our group. I enjoyed the atmosphere, their friendship, and their moral support.

My thanks to Christine Ruhland and Ingrid Hörnchen for help on administrative matters. My thanks also to Ralph Strobl, and after him, Stephan Ketterbach and the computer pool for their help when I had some problems with my computer was down.

Last but not least, I wish to thank my family who has always supported me, Julie and Jean for real friendship, and most of all Alban for enjoying life together with me.

This thesis has been supported by the German Research Foundation (DFG) by the financial project BA 1444/16-1. Their support is gratefully acknowledged.

Abstract

During rising to the Earth's surface and cooling, magmas which consist of melt plus suspended crystals and/or bubbles have to be transported from their source region to the emplacement sites. The transport process operates on two length scales: (1) segregation, which is marked by a small-scale movement of melt on centimeter to decimeter scale (it operates mostly within the source region); and (2) magma ascent on kilometer scale, which takes place within the continental crust from the magma source to the site of final emplacement. The present thesis aims to model different aspects of ascent and segregation of magma via three series of centrifuge experiments. Under the scope of the present thesis there are laboratory investigations of several processes occurring during melt segregation (crystal settling and compaction processes), as well as during ascent of magmas and emplacement of plutons. With the help of three different sets of centrifuge experiments rates of these three magmatic processes have been evaluated.

In the first series of the centrifuge experiments, the diapiric ascent of buoyant material from two source layers at different depths was studied. Through five models, the hypothesis of ascending diapirs was tested and it was demonstrated whether a rising diapir ascends straight upward or if its ascent might be deviated by another buoyant, softer – and consequently easier to travel through – layer which is located within the overburden strata. The background for this question is the frequent occurrence of concentrically zoned plutons, possibly formed by magma chamber inflation. We were interested under which conditions they can be formed.

For this purpose we placed perturbations on top of both the buoyant layers; either with a set-off of both the protrusions (for three of these experiments), or with both protrusion sitting directly on top of each other (for one of the experiments). In the first experiment, we omitted the perturbations, to test which pathways diapirs take which grow from natural Rayleigh-Taylor instabilities. Three others experiments differed in the viscosity contrast between the overburden and the buoyant material. As buoyant material we used PDMS (polydimethylsiloxane), a Newtonian silicone with the density 964 kg/m^3 and viscosity $2.5 \cdot 10^4 \text{ Pa s}$. The overburdens were all non-Newtonian materials. The viscosity contrasts at the applied strain rate of 0.011 s^{-1} were for exp. 1 and exp. 2

~0.73, for exp. 3 ~0.06, and for exp. 4 and for exp. 5 ~0.25. All experiments were conducted at 700 g

Due to the different viscosity contrast m (overburden viscosity / buoyant viscosity) we found that the number of diapirs increases with decreasing m values. This means, that the softer the overburden is, the less resistance it exhibits against the rising buoyant material. Consequently, a softer overburden leads to more diapirs rising. Nevertheless, the size of the individual diapirs does not depend on m . Rather, the size of the resulting diapir is a function of the position of the perturbations on top of each layer. Only when the protrusions sit directly on top of each other the lower diapir can use the stem of its precursor (i.e. the upper PDMS layer) as ascent path and we end up with one large diapir whose head forms a tabular body at the top of the model. In all other experiments, either without perturbation, or with offset perturbations, the diapirs rising from the lower PDMS layer do not use the upper layer for their rise and simply pierce through it. Consequently, we did not achieve nested, large diapirs, but small diapirs of mushroom shape consisting only either of the upper (yellow) or lower (blue) PDMS. The reason for the lower buoyant layer not using the upper buoyant layer as pathway is simple: The upper layer is deformed into rim synclines and significantly thinned due to the rise of diapirs from the lower PDMS layer. Therefore, these soft, but strongly deformed layers are not any longer suitable pathways for rising diapirs. Instead piercing through the entire model irrespective of the material they are traveling through is the more convenient way for the rising diapirs from the lower PDMS layer. Only in the case of the lower diapir growing directly underneath the upper one, the first one can profit from the straight stem of the latter one and uses it for its rise. Consequently, the resulting diapir is a concentrically expanded tabular body. Typical for this type of experiment is the incorporation of a lot of overburden material into the stem of this composite buoyant body.

The observed ascent and emplacement behavior of diapirs have their counterparts in geologic objects. Diapiric structures as those derived from the models without perturbation and where the perturbation are offset, i.e. small individual not nested diapirs developing from source layers at different depths, occur within Great Kavir Basin (Iran), where numerous salt diapirs grew from several salt horizons, which show a similar spatial distribution. The resulting structure observed in the model where the two perturbations situated directly above each other, is close to what is observed in

composite batholiths such as the Flasergranitoid Zone within the Bergsträßer Odenwald Crystalline Complex (Germany).

The second series of models were aimed to study crystal settling within a magma. For this purpose experiments with an artificial magma of 30 vol% olivine in 70 vol% basaltic melt were conducted to elucidate the formation mechanisms and time scales of gravitational cumulates. The settling experiments were performed in a centrifuging piston cylinder at 200-1500 g, 1270-1280°C, and 0.8-1.1 GPa on previously annealed and texturally equilibrated samples. The mechanical settling of the dense olivine suspension occurs at about 1/6 the speed of simple Stokes settling and a sedimentation exponent n of 4.1 in agreement with predictions from analogue systems (Cabane et al., 2005). The porosity (ϕ_m) of the resulting orthocumulate is about 52 % and formation times of olivine orthocumulates result to $0.1-2.5 \text{ m}\cdot\text{day}^{-1}$ (for an initial crystal content of the melt of 1% and grain sizes of 2 to 10 mm).

After mechanical settling, olivine grains rest in contact with each other, and further compaction occurs through pressure dissolution at grain contacts, olivine re-precipitation where olivine is in contact with melt, and concomitant expulsion of excess liquid from the cumulate layer. Under the centrifugation at 400 g for 50 h, porosities as low as 31 % have been achieved in olivine MORB aggregates. The olivine content at the bottom of the gravitational cumulate is $1-\phi_m \sim \log(\Delta\rho \cdot h \cdot a \cdot t)$, where $\Delta\rho$ is the density difference between crystals and melt, h the crystal layer thickness, a the acceleration, and t the time of centrifuging, hence compaction is proportional to effective stress integrated over time. Crystal size distribution curves and the grain size growth exponent $n \sim 3.6$ indicate that diffusion controlled Oswald ripening is the dominant crystal growth mechanism in concentrated magmatic suspensions (Hanitzsch and Kahlweit, 1969; Lifshitz and Slyozov, 1961; Hillert, 1965). This fact demonstrates that pressure dissolution resulting in chemical compaction is also controlled by diffusion.

The above relationship, combined with the proper scaling of compaction rate to the grain size, allows the calculation of formation times for adcumulates. If chemical compaction is limited by dissolution-precipitation process (Boudreau and McBirney, 1997; Shimizu, 1995), then the natural olivine adcumulates of ½ m thickness with 70-75 vol% olivine at the base as it is observed in the Rhum layered intrusion, would have typical formation times of 0.3-3 years for grain sizes of 2-10 mm. This time scale is in agreement with the characteristic cooling times of sills or magma chambers of km size.

Thus, gravitational settling and compaction is a feasible cumulate forming process for dense cumulus in mafic magma chambers.

The last series of centrifuge experiments have been carried out in order to better understand the relations between cumulus texture and evolution of the chemical composition at grain boundaries and in the interior of a magma chamber during the crystal-melt settling-floating process. The settling-floating experiments were conducted in a system composed of two pyroxene-gabbro with the help of a centrifuging furnace at 1235°C under atmospheric pressure during 6 hours (Dorfman, Bagdassarov and Dingwell, Bagdassarov et al., 1996). The major variable in these experiments is the applied acceleration during the runs, which varied between 1g to 1000g. The grains in the partially molten gabbro samples have a size of approximately 100µm. One experiment at 1290°C with higher degree of partial melting is conducted in order to appreciate the influence of temperature on cumulate and settling-floating compaction.

During the centrifuging process, the crystals have been segregated according to their buoyancy: plagioclase crystals floated to the top and magnetite crystals sank to the bottom of the capsule. It is in experiments at 500g and 1000g that the most important separation of heavy and light crystals and the melt phase is observed.

The analyses revealed that the chemical evolution of the melt, and its chemical pattern in space, is similar for the coupled experiments at 100g and 200g and for the couple of experiments of 500g and 1000g. More precisely, the vertical evolution of the major and trace elements in the melt phase demonstrates that in a region close to the cumulate layer (between 0 and 2 mm from the container bottom) the variation of these elements depends on the distance from the capsule bottom. At larger distances from the container bottom in the interior of the sample the concentrations become constant. Some variations of the melt chemical composition appear in the horizontal direction. The variation in chemical composition of the melt close to the container walls are due to the wall effect during the centrifugation process.

In order to describe the compaction evolution with time, a numerical experiment of the sedimentation process of the crystals was made and compared with the centrifuge modeling results. The numerical and centrifuge modeling results agree quite well: the stratification of the compacted layer in the runs is reproduced in numerical models. Moreover, on the base of the numerical and centrifuge modeling a sedimentation exponent describing a deviation of settling in concentrated suspensions from Stokes sedimentation has been evaluated. The settling model of a concentrated suspension can

predict a realistic evolution of the cumulus layer compaction for a time scale of several years. The combination of centrifuge experiments and numerical modeling demonstrates that in magma chambers there are correlations between cumulus textures and the evolution of chemical composition at grain boundaries during the stage when crystals come into mechanical contact with each other in a cumulus layer.

Finally, formation time and melt fraction evolution of Muskox layered intrusion have been revisited using the hindered sedimentation model calculations. The results on the time formation of the intrusion as well as the porosity loss with time are in agreement with previous results of the compaction model (Tharp et al., 1998).

Keywords: centrifuge modeling; diapir emplacement; composite pluton; grain settling; gravitational cumulate; chemical compaction; magma chamber.

Abstrakt

Magma (Schmelze mit darin enthaltenen Feststoffen und Gasen) steigen in aller Regel aus einer Quell- oder Schmelzregion auf, um in einem höheren Krustenniveau eine Magmenkammer zu bilden. Der Transportvorgang geschieht auf zwei Größenskalen: (1) Schmelzsegregation ist ein kleinmaßstäblicher Prozess, der im Zentimeter- bis Dezimeterbereich und vor allem im Quellbereich stattfindet; (2) der Magmenaufstieg ist ein großmaßstäblicher Prozess, der die gesamte Erdkruste umfassen kann: zwischen Schmelz- und Platznahmeregion liegen oft viele Kilometer. Diese Arbeit untersucht verschiedene Prozesse, die während der Schmelzsegregation (Absinken von Kristallen und Kompaktions-Prozesse), des Magmenaufstiegs und der Plutonplatznahme stattfinden. Unter Verwendung von drei verschiedenen Zentrifugen und mit Hilfe von drei Experimentreihen habe ich versucht, diese Mechanismen genauer zu verstehen.

Mit der ersten Experimentalreihe wurde der diapirische Aufstieg eines auftriebigen Materials aus zwei unterschiedlichen Quellschichten in unterschiedlicher Tiefe simuliert. Mit Hilfe von fünf Modellen sollte gezeigt werden, ob ein aufsteigender Diapir einfach senkrecht nach oben wandert, oder ob er eine darüberliegende niedrigviskose Lage für seinen Weg durch das Auflager benutzt. Hintergrund dieser Fragestellung ist das häufige Vorkommen konzentrisch-zonierter Plutone, die möglicherweise durch Magmenkammerexpansion entstanden sind. Wir sind an den Prozessen, die solche Plutone formen, interessiert.

Daher konstruierten wir Modelle mit zwei auftriebigen Lagen, die in vier von fünf Fällen mit Protrusionen versehen waren. Bei drei Versuchen waren die Protrusionen gegeneinander vertikal versetzt, in einem Fall saßen sie direkt übereinander. Beim ersten Experiment ließen wir die Protrusionen weg, um zu testen, welchem Aufstiegs Pfad Diapire folgen, die aus natürlichen Rayleigh-Taylor-Instabilitäten erwachsen. Außerdem waren bei drei Experimenten die Viskositätskontraste zwischen Auflager und auftriebiger Lage deutlich unterschiedlich. Als auftriebige Material benutzten wir PDMS (Polydimethylsiloxan), ein Newtonisches Silikon mit einer Dichte von 964 kg/m^3 und einer Viskosität von $2,5 \cdot 10^4 \text{ Pa s}$. Die Auflagermaterialien waren allesamt nicht-Newtonisch. Der Viskositätskontrast (bei der angewandten Strainrate von $0,011 \text{ s}^{-1}$) war

in den Experimenten 1+2 $\sim 0,73$, in Experiment 3 $\sim 0,06$ und in den Experimenten 4+5 $\sim 0,25$. Alle Experimente wurden bei 700 g durchgeführt.

Wir haben herausgefunden, dass die Diapiranzahl direkt abbbhängig ist vom Viskositätskontrast m (1981) (Auflagerviskosität / Viskosität des auftriebigen Materials). Dabei gilt: Je weicher das Auflager, desto mehr Diapire. Andererseits wird die Größe der einzelnen Diapire nicht durch m kontrolliert. Vielmehr ist die Diapirgröße eine Fuktion der Anordnung der Protrusionen zueinander. Nur wenn beide Protrusionen direkt übereinander sitzen, kann der untere Diapir den Stamm des oberen für seinen Aufstieg nutzen. Dann entsteht ein Riesendiapir aus beiden auftriebigen Lagen mit einem großen tabularen Kopf. In allen anderen Experimenten, mit und ohne Protrusion, durchstoßen die Diapire, die aus der unteren PDMS-Lage wachsen, die obere PDMS-Lage, ohne sie für ihren Aufstieg zu nutzen. Entsprechend entstanden bei keinem dieser Experimente große, ineinander verschachtelte Diapire, sondern klein, pilzförmige, die jeweils nur aus dem Material der oberen (gelb) oder unteren (blau) PDMS-Lage bestanden. Der Grund für das einfache Durchstechen der oberen PDMS-lage durch die aufsteigenden Diapire ist denkbar einfach: die obere PDMS-Lage wird durch den Aufstieg der unteren so stark verformt und ausgedünnt, dass sie keinen einfach zu nutzenden Förderkanal für die blauen PDMS-Diapire darstellt und nicht besser geeignet ist für den Aufstieg dieser Diapire als das nicht-Newtonische Auflager. Nur in dem Experiment, bei dem die untere Protrusion direkt unter der oberen lag, kann der untere Diapir den Stamm des oberen tatsächlich für seinen Aufstieg nutzen. Hier entsteht dann auch ein „Schachtel-Diapir“ mit einem sehr breiten, tabularen Kopf und ebenfalls sehr breitem Stamm, der außerdem viel Auflagermaterial enthält.

Für beide beobachteten Strukturtypen gibt es Analoga in der Natur: Kleine Salzdiapire, die sich aus unterschiedlichen Quellniveaus speisen gibt es im Großen Kavir-Becken im Iran. Die räumliche Verteilung dieser kleinen Salzintrusionen ähnelt der, die wir in unseren Experimenten beobachten konnten. Diapir-in-Diapir-Strukturen, die entstehen, wenn ein aufsteigender Intrusivkörper den Förderkanal eines entsprechenden darüberliegenden Intrusivkörpers nutzt, finden wir im Kristallinen Bergsträßer Odenwald, wo wir vermutlich den Stammbereich eines solchen verschachtelten Plutonkomplexes betrachten.

Die zweite Versuchsreihe Zentrifugen-assistierter Setzungs-Experimente mit 30 Vol.-% Olivin und 70 Vol.-% basaltischer Schmelze wurde durchgeführt, um Aufschluss über die Bildungsmechanismen und die Zeiträume gravitativer

Akkumulationen zu erhalten. Die Setzungs-Experimente wurden in einem zentrifugierten Kolben-Zylinder bei 200- bis 1500-facher Erdbeschleunigung (g), 1270-1280°C und 0,8-1,1 GPa an Proben durchgeführt, die zuvor aufgeglüht und strukturell gleichgerichtet wurden. Das mechanische Absinken der dichten Olivin-Kristalle erfolgt bei etwa einem Sechstel der Geschwindigkeit eines normalen Stokes-Sinkvorgangs mit einem Sedimentations-Exponenten $n = 4,1$ in Übereinstimmung mit Voraussagen von analogen Systemen (Cabane et al., 2005). Die Porosität (ϕ_m) der resultierenden ortho-Akkumulate beträgt rund 52 % und die Bildungsdauer der Olivin-ortho-Akkumulate liegt bei 0,1-2,5 m/d (für einen Anfangsgehalt von 1 % Kristallen in der Schmelze und Korngrößen zwischen 2 und 10 mm).

Nach der mechanischen Setzung liegen die Olivin-Körner übereinander und weitere Kompaktion tritt ein durch Auflösung an den Kornkontakten durch den Druck der Körner, erneute Abscheidung von Olivin an Stellen, wo noch Kontakt zur Schmelze besteht, sowie gleichzeitige Verdrängung überschüssiger Fluide aus der akkumulierten Schicht. Durch Zentrifugieren bei 400 g für eine Dauer von 50 Stunden wurden niedrige Porositäten von bis zu 31 % erreicht. Der Olivinegehalt am Boden des gravitativen Akkumulats beträgt $1-\phi_m \sim \log(\Delta\rho \cdot h \cdot a \cdot t)$, wobei $\Delta\rho$ für den Dichteunterschied zwischen den Kristallen und der Schmelze steht, h für die Schichtmächtigkeit, a für die Beschleunigung und t für die Zeitdauer des Zentrifugierens steht. Die Kompaktion ist demnach proportional zur effektiven Spannung integriert über die Zeit. Kurven der Kristallgrößen-Verteilung und ein Wachstums-Exponent von $n = 3,6$ deuten darauf hin, dass die durch Diffusion kontrollierte Ostwald-Reifung der vorrangige Mechanismus für das Kristallwachstum darstellt (Hanitzsch and Kalhweit, 1969; Lifshitz and Slyozov, 1961; Hillert, 1965). Daraus folgt, dass druckbedingte Lösung, die zur chemischen Kompaktion führt, ebenfalls durch Diffusion kontrolliert wird.

Der oben dargestellte Zusammenhang in Kombination mit der notwendigen Skalierung der Korngröße erlaubt die Berechnung der Bildungsdauer von Akkumulaten. Wenn chemische Kompaktion auf Auflösung und Wiederanlagerung beschränkt ist (Boudreau and McBirney, 1997; Shimizu, 1995), hätten natürliche Olivin-Akkumulate von einem halben Meter Mächtigkeit und mit einem Olivinanteil von 70-75 Vol.-% an der Basis (wie in der geschichteten Rhum Intrusion beobachtet) typische Bildungsdauern von 0,3-3 Jahren bei Korngrößen von 2-10 mm. Dieser Zeitraum ist gut vergleichbar mit charakteristischen Abkühlraten von Sills oder Magmakammern.

Gravitatives Absinken und Kompaktion ist demzufolge ein plausibler Bildungsmechanismus für Akkumulate dichter Mineralien in mafischen Magmen.

Die letzte Versuchsreihe von Zentrifugen-Experimenten wurde mit dem Ziel durchgeführt, ein besseres Verständnis der Zusammenhänge zwischen der Kumulus-Textur und der Entwicklung der chemischen Zusammensetzung an den Korngrenzen sowie im Inneren der Magmakammer während der Sink- und Fließvorgängen zwischen Kristallen und Schmelzen zu erlangen. Die Versuche zu den Sink- und Fließvorgängen wurden mit Hilfe eines Zentrifugen-Ofens bei 1235°C unter Atmosphärendruck über 6 Stunden (Dorfman, Bagdassarov and Dingwell, Bagdassarov et al., 1996) in einem System durchgeführt, das aus zwei natürlichen Pyroxen-Gabbro-Proben bestand. Die hauptsächliche Variable in diesen Versuchen war die Beschleunigung während der Durchläufe, die von 1 g bis 1000 g variiert wurde. Die Körner in den partiell geschmolzenen Gabbro-Proben hatten eine Größe von etwa 100 µm. Ein Experiment bei 1290°C mit einem höheren Grad der Aufschmelzung wurde durchgeführt, um den Einfluss der Temperatur auf die Akkumulate und die Sink-Fließ-Kompaktion abzuschätzen.

Während des Zentrifugierens wurden die Kristalle ihrem Auftrieb entsprechend abgeschieden: Plagioklas-Kristalle strömen nach oben, während Magnetit Kristalle zum Boden der Kapsel sinken. Die Experimente bei 500 g und 100 g wiesen die deutlichste Trennung von schweren und leichten Kristallen sowie der Schmelzphase auf.

Die Analyse ergab, dass die chemische Entwicklung der Schmelze, die vertikale und horizontale Verteilung, für die Experimente bei 100 g und 200 g sowie für die Experimente bei 500 g und 1000 g jeweils gleichartig ist. Genauer gesagt, zeigt die vertikale Entwicklung der Haupt- und Spurenelemente in der Schmelzphase, dass die Variation dieser Elemente in einer Region nahe der akkumulierten Schicht (zwischen 0 und 2 mm vom Kapselboden) vom Abstand zum Kapselboden abhängt. Bei größeren Abständen vom Behälterboden erreichen die Konzentrationen im Inneren der Probe einen konstanten Wert. Lateral treten einige Unterschiede in der chemischen Zusammensetzung der Schmelze auf. Änderungen der chemischen Zusammensetzung in der Nähe der Behälterwände hängen unmittelbar mit Wandeinflüssen während der Zentrifugierens zusammen.

Um den Verlauf der Kompaktion mit der Zeit zu beschreiben, wurde eine numerische Modellierung der Sedimentationsprozesse der Kristalle durchgeführt und mit den Zentrifugen-Experimenten verglichen. Beide Modellierungsansätze stimmen gut überein: Die Strukturen innerhalb der kompaktierten Schichten aus den Zentrifugen-Versuchen konnten in den numerischen Modellen gut reproduziert werden. Darüber hinaus konnte auf der Basis der numerischen Modellierung und der Zentrifugen-Versuche ein Sedimentations-Exponent untersucht werden, der die Abweichungen des Sinkverhaltens in konzentrierten Suspensionen von der Stokes-Sedimentation beschreibt. Das Setzungsmodell einer konzentrierten Suspension kann einen realistischen Verlauf der Kompaktion der Kumulus-Schicht für einen Zeitraum von mehreren Jahren voraussagen. Die Kombination der Zentrifugen-Experimente mit der numerischen Modellierung zeigt, dass, während der Phase, in der die Kristalle in der akkumulierten Schicht mechanischen Kontakt zueinander erhalten, in Magmakammern Wechselbeziehungen zwischen der Kumulus-Textur und der Entwicklung der chemischen Zusammensetzung an den Korngrenzen bestehen.

Abschließend wurden die Bildungsdauer und die Entwicklung des Schmelzanteils einer geschichteten Muskox Intrusion mit Hilfe von Berechnungen eines Modells beeinträchtigter Sedimentation aufgegriffen. Die Ergebnisse zur Bildungsdauer der Intrusion, wie auch der Verlust der Porosität mit der Zeit stimmen mit früheren Ergebnissen des Kompaktionsmodells (Tharp et al., 1998) überein.

Schlüsselwörter: *Zentrifugenmodellierung; Diapir-Einlagerung; Mischpluton; Kornabsenkung; gravitative Akkumulation; chemische Kompaktion; Magmakammer.*

Résumé

Cette thèse cherche à expliquer (1) la mise en place des plutons et (2) les mécanismes de ségrégation et de compaction dans les intrusions litées. Pour cela, trois séries d'expériences en centrifugeuses ont été menées, chacune d'elle employant une centrifugeuse différente. La première est une centrifugeuse industrielle utilisée pour effectuer les expériences de mise en place de pluton. Elle possède de grands conteneurs, utiles pour la modélisation analogique. La deuxième est un « piston-cylindre centrifugé » permettant d'atteindre des hautes pressions et température, tout en soumettant une accélération aux échantillons. Enfin, la troisième est un four-centrifuge identique au précédent à l'exception de la pression. Les expériences sont menées à pression atmosphérique dans cette troisième.

Dans la première série, cinq essais modélisent la cinétique et la dynamique d'un matériel moins dense que son encaissant pendant la montée et mise en place de diapirs. Au cours des expériences, on observe les effets de différentes viscosités de l'encaissant ainsi que l'influence de la position des perturbations sur le nombre des diapirs générés. Les expériences soulignent également les chemins des diapirs et les schémas de déformation des couches de l'encaissant.

La deuxième série explique les mécanismes et des temps de formation des cumulâts gravitationnels. Le système de magma basaltique contenant 30 vol% d'olivine utilisé révèle deux processus physiques principaux : le compactage purement mécanique et la compaction chimique induite par le mécanisme de dissolution et reprécipitation.

La dernière série d'expériences traite du mécanisme de séparation des cristaux dans un système composé d'un gabbro naturel à deux pyroxènes. La modélisation analogique et une simulation numérique y sont comparées afin de comprendre les relations entre la texture des cumulâts et l'évolution de la composition chimique aux joints de grains au cours de la séparation melt-cristaux dans une chambre magmatique.

Les résultats expérimentaux obtenus renseignent quant à l'éventuelle formation de cas naturels. Les diapirs de sel naturel, comme certains dans le bassin de Grand Kavir (Iran), ont une distribution spatiale similaire aux diapirs imbriqués obtenus dans nos modèles. Lorsque deux perturbations sont situées l'une en dessous de l'autre, la structure résultante est comparable à des exemples naturels de batholites composites tels

que le complexe cristallin du Bergsträßer Odenwal (Allemagne). De même, des intrusions litées naturelles telles que celles du Muskox ont pu être reproduites par la simulation numérique développée pour les expériences de séparation des cristaux

Mots-clés: Modélisation analogue ; Centrifuge ; Mise en place des diapirs ; Plutons composites ; Décantation des grains ; Cumulâts gravitationnel ; Chambre magmatique.

Introduction

Magmatic systems consist of sills, dykes, and sometimes volcanic pipes, but the main part of a plumbing magmatic system is a magma chamber. Inside a magma chamber, magma undergoes some important chemical and petrological transformations. In fact, several processes may occur, such as fractional crystallization, melt segregation and surrounding rock assimilation, which change the primary magma composition into a large variety of magmatic liquids evolved from the same source. In order to better understand these complex phenomena and their implications to the formation of geological rocks and structures, analogue laboratory modeling and numerical simulations are often used to reconstruct magma chamber evolution (Longo et al, 2006; Montanari et al., 2010). These models enable to reproduce some aspects of petrological and dynamic processes observed in nature by using a laboratory length and time scales. In some laboratory models magma chambers have been modeled with the help of transparent container filled with aqueous solutions of sodium carbonate (Na_2CO_3) imitating crystallization of magma by precipitation process from the aqueous solution. At the top, a special system of circulating cold water provides a vertical thermal gradient, i.e. the temperature profile has been created with temperature decreasing from the top to the base (McBirney 1980, McBirney and Murase, 1984). This type of analogue modeling is too simplistic to imitate adequately crystallization - segregation processes and can only be used for mustering of our intuition about what may happen in magma chambers. However, the application of small scale models requires information on viscosity, density, crystal size and their fractions during the course of crystallization. These data are provided by rock samples and observations in the field, such as orientation and dip angle of crystal layers in magma chambers, fold shapes, their axes directions, and the direction of faults in outcrops. Moreover, only this information permits geologists to better understand the various deformations of the magmatic structures. In addition, an “auscultation” of the structures at depth can be realized with the help of geophysical measurements. One illustration of the efficiency of these techniques is, for example, the compilation of seismic data from surveillance network of Kilauea (Hawaii) that shows the existence of a huge plumbing network in seals and dykes under the main edifice, and the 60-kilometer deep reservoir (Eaton and Murata, 1960).

Judging from Hubbert (1937), analogue models may represent adequately a natural prototype, only, if three aspects of similarity are preserved: geometric similarity, kinematic similarity and dynamic similarity. Since Hubbert's work (1937), several papers have been published on scaling of analogue models in application to geological processes (Hubbert, 1951; Horsfield, 1977; Shemenda, 1983; Richard, 1991; Davy and Cobbold, 1991; Cobbold and Jackson, 1992). In all laboratory experiments on magma chamber simulation, each physical parameter such as temperature gradient, viscosity, density contrast, crystallization temperature interval, yield stress, etc., should be scaled properly preserving the same proportion between laboratory model size and the natural object size. In other words, the dimensionless numbers such as Reynolds number, Péclet number, Luis number, Rayleigh number, etc., describing the process should be the same in laboratory model and in natural object. This may be a problem because a simultaneous satisfaction of all this dimensionless numbers is practically impossible. How to resolve this problem? The solution of the problem may be in realization of a set of laboratory experiments using a wide range of dimensionless numbers and establishing an empirical relationship between two or three of dimensionless numbers which are involved in parameterization of physical processes in magma chambers. Using the empirical relationship between dimensionless numbers it would be possible to make some predictions for natural size objects. Variation of dimensionless numbers in laboratory may cost a lot and some parameters are difficult to vary. Crystal size, viscosity may be varied within two orders of magnitude, but temperature range or density are not. Another parameter which may be vary at a relatively low cost is gravity acceleration. Thus, with the help of a centrifuge in which the centrifugal acceleration and, therefore, the density contrast between phases may be increased by 3 orders of magnitude, the dimensionless numbers including gravity acceleration can be varied additionally. This brings a big advantage by laboratory modeling of magmatic processes. Instead of using analogue liquids which low crystallization-precipitation temperature and small temperature gradients, natural rocks and their melts could be used in laboratory models.

In this thesis, two structures are studied with the help of centrifuge experiments in detail through analogue modeling: nested diapirs and layered intrusions. The nested diapirs consist of a magmatic mass, partially molten (the early plutonic diapir) and intruded by a secondary younger diapir. They are believed by some researchers

(Paterson and Vernon, 1995; Miller et al., 1988) to play an essential role in the construction of huge batholiths, because successive intrusions of diapirs in the same area or in the same magma chamber can prolong significantly the “life time” of a magmatic system (Dietl & Longo 2007). They have frequently been interpreted as concentrically zoned, inflated plutons (e.g. Ramsay, 1989), or as nested diapirs (Paterson and Vernon, 1995). Famous examples include the Ardara pluton in Ireland (Akaad, 1956a, 1956b; King, 1966; Holder, 1979, 1981; Pitcher and Berger, 1972; Sanderson and Meneilly, 1981), the Cannibal Creek granite in Australia (Bateman, 1983, 1985; Castro, 1987), the Papoose Flat pluton in California (Nelson et al., 1978; Sylvester et al., 1978; Hibbard, 1987; Nelson, 1987). According to Paterson and Vernon (1995), nested diapirs display compositional zoning either from more mafic margins (usually tonalite to quartz diorite) to more felsic cores (usually granite or granodiorite), or, less commonly, from a felsic rim to a mafic core. Flattened enclaves are found close to pluton margins, whereas in country rocks, deflection of structures into parallelism with pluton margins is noticeable. Ductile deformation can be observed in the contact metamorphic aureole, as well as an increase of the foliation intensity toward the pluton – country rock contact in both the pluton and the surrounding country rocks (Weinberg and Podladchikov, 1994, 1995). However, formation of these concentrically expanded plutons is disputed. Generally, two intrusion mechanisms are proposed. One mechanism is diapiric ascent and emplacement of the plutons. Diapirism means the upwelling of relative mobile, more buoyant material (e.g., magma), through overlying, denser rocks (Bishop, 1978). When they rise, diapiric plutons obtain an elliptical shape. Several consecutive intrusions into the same body form diapir-in-diapir structures or “nested diapirs” (Paterson and Vernon, 1995). In these structures, the earlier magma bodies might be intruded by subsequent diapirs of different composition. The second process proposed for the formation of concentrically expanded plutons is a combination of dyking as ascent mechanism, and ballooning as emplacement process, *sensu strictu* (Petford, 1996). In this model, magma is transported through a central dyke and stored in a tabular magma chamber, which starts as a sill and becomes inflated while more and more magma is transported upward through the conduit into the developing pluton (e.g. Molyneux and Hutton, 2000; Ramsay, 1989; Paterson and Vernon, 1995). Lister and Kerr (1991) defined dyking as the upward movement of a fluid phase through elastic fracturing of rocks driven by the high magma pressure at the dyke tip. The dyke propagates perpendicular to the least principal stress and may follow weakness zones in

the rock. These conduits have a large lateral extent relative to thickness (ratio length over thickness = 10 to 100, Spera, 1980). Magma chamber inflation or ballooning leads to ductile deformation within the plutons and the host rocks within their structural aureole.

Layered intrusions are formed in magma chamber from a complicated process of crystallization, sedimentation and compaction. The gravitational accumulation of generally downward settling silicates, oxides, or sulfides has been proposed as a dominant mechanism forming cumulate layers sometimes extending over >100 km and involving magma volumes of several km³. The most famous layered intrusions are Skaergaard (Greenland), Bushveld (South Africa), Stillwater (Montana), Muskox (Canada), and Windimura (Australia) (Wager and Brown, 1968), most of them being of huge economical interest due to their high concentration of metals (e.g. Cr, V, Pt, Pd) in specific layers. Whether gravitational settling of crystals out of a suspension followed by pressure driven chemical compaction is the dominant mechanism of the formation of such layering is matter of intensive debate (Irvine 1987). Other cumulate forming mechanisms include density currents (Wagner and Brown 1968; Irvine 1987; Conrad and Naslund 1989), magma chamber recharge and mixing (Gasquet et al. 1995; Lucas and St-Onge 1995), temperature oscillations across a cotectic (Leshner and Walker 1988), in-situ crystallization from a boundary (McBirney and Noyes 1979; Langmir 1989), layers with double diffusive convection (McBirney and Noyes 1979; Chen and Turner 1980; Kerr and Turner 1982; Irvine et al. 1983; Huppert and Sparks 1984; Wilson and Larsen 1985; Wilson et al. 1987; Robin et al. 1987), and preferential or oscillatory nucleation (Wager 1959; Hort et al. 1993), or any combination of the mentioned above processes. Illustrated examples of such magma chamber processes can be found in Parson (1986), Mc Birney and Nicolas (1997), Boudreau and McBirney (1997), and a discussion on cumulate forming mechanisms in Naslund and McBirney (1996). The formation of cumulates has been mostly investigated from field data (Wager et al. 1960; Holness et al. 2005), analogue experiments (Schwindinger, 1999) and numerical modeling (Akatasuka et al. 1999; Hoshide et al. 2006; Tory and Pickard 1977; Tory and Pickard 1986). Mineralogically, cumulate layering is termed cryptic when defined through changes in composition of the constituting mineral(s). Contrasting, phase layering describes the abrupt entrance or exit of cumulus minerals at particular horizons of the sequence. Texturally, cumulates are defined as orthocumulates when grains are just barely in contact and the residual melt fraction crystallized between

the accumulated grains. In contrast, adcumulates are characterized by very small melt fractions crystallized between the accumulated grains (Wager et al., 1960). Orthocumulates are thought to be formed by purely mechanical settling, the maximum solid fraction of the gravitationally settling mineral(s) corresponding to the maximum close packing for a solid with the shape of the crystallizing phase(s). Contrasting, adcumulates (Wager et al., 1960) may involve a first crystal concentration mechanism such as gravitational settling, but densification of the cumulate is driven by chemical compaction during which grains grew at the expense but not from the liquid trapped between early crystals. The latter may then result in an increase of the crystal fraction to up to 90% (Yang, 2000). In Skaergaard, there are levels constituted by up to 90 vol% of plagioclase and in Rhum the mineral content of olivine content of cumulates reaches ~80 vol% (Wager and Brown, 1968). Both types of cumulates can be found together or separated in complexes such as the Rhum intrusion, the Bushveld complex, and the Skaergaard complex.

Nested diapirs and layered intrusion take place at depth and only few outcrops enable them to be investigated in detail (Cactus Flat, Southern California, Alpert, 2006; Turtle Pluton, southeastern California, Allen, 1992; Bushveld and Stillwater complexes, Campbell et al, 1983). Their emplacement mechanisms are based on the same physical principle: their driving force is gravity. In fact, in the case of diapir ascending, the physical mechanism taking place could be compared with that of gravitational instability, inherent to a fluid with a light density under a denser fluid: the Rayleigh-Taylor instability. In the case of cumulate formation, one of the mechanisms occurring during magma cooling is gravitational settling: the density of the crystals being higher than the density of magma, and, hence, the crystals settle at the bottom of magma chamber. If crystals, however, have a lower density than the magma, then the crystals will float on top of magma chamber. Both these emplacement mechanisms take place on an important time scale. Therefore, a centrifuge was used in order to simulate the acceleration of gravity g , substituting the gravitational field by a radial centrifuge field. In the case of nested diapirs, the centrifuge has already been used earlier for modeling and is an important tool in understanding pluton ascent and emplacement (e.g. Dietl and Koyi, 2002, Cruden et al., 1995). The results of Dietl and Koyi (2002) show that nested diapirs can be formed by a combination of diapirism and subsequent “ductile dyking” of buoyant material through the stem of pre-existing diapirs. For modeling of a cumulate

formation, the centrifugation, as a mean to accelerate the crystal settling and cumulate formation in magma chambers at atmospheric pressure, was pioneered by Roeder and Dixon (1977) and Kadik et al. (1989). In both studies a rotating 1-atm furnace was used. Centrifugation under pressure was introduced by Dorfman et al. (1997) by mounting an externally heated autoclave capable of 100 MPa internal gas pressure into a laboratory biocentrifuge. Finally a piston cylinder was mounted onto a centrifuge by Schmidt et al. (2006), extending the range of centrifuging pressures to 1.7 GPa. These capability is especially valuable, because of reducing conditions in a cell and a very fast cooling rate by quenching samples from melting (1600 K) to room temperature.

The first part of the thesis is dedicated to the principles of modeling with a centrifuge, then a short description of specifications of each centrifuge used in this study is presented. The second part deals with the formation of composite plutons under complex conditions, specifically the course of two simultaneously ascending diapirs, which rise from different depths and different lateral positions, has been studied. In the third chapter, experimental results of formation of cumulate layers of olivine from suspensions in basaltic melt are presented. The results are presented in sense of mechanical and chemical compactions. These results allow to consider hindered sedimentation mechanisms and to evaluate formation times of ortho- and adcumulates. The fourth part presents comparison of numerical simulation on hindered crystal settling in a magma chamber with centrifuge experiments. The fifth chapter is dedicated to the discussion about the experimental results and their application to Muskox layered intrusion.

Chapter I

Principles and methods

Table of content

I.1 - PRINCIPLES OF THE MODELING.....	33
<i>I.1.1 - Centripetal and centrifugal force</i>	<i>33</i>
<i>I.1.2 - Sedimentation principle.....</i>	<i>35</i>
I. 2 - CENTRIFUGES	36
<i>I.2.1 - How a centrifuge works technically</i>	<i>36</i>
<i>I.2.2 - Centrifuge used in this study.....</i>	<i>38</i>
<i>I.2.2.1 - Furnace centrifuge (Bayreuth, Germany).....</i>	<i>38</i>
<i>I.2.2.2 - Centrifuging piston cylinder (Zürich, Switzerland).....</i>	<i>38</i>
<i>I.2.2.3 - Centrifuge (Frankfurt, Germany).....</i>	<i>39</i>

I.1 - Principles of the modeling

Nested diapirs and layered intrusions are two natural structures, which are formed due to the same force: gravity. With this respect we have chosen a centrifuge to simulate the important role of gravitational acceleration in our models. Within a centrifuge, gravitational acceleration (g) is (x) times higher than in nature. Therefore, the density contrast between the model materials is increased several (x) times. In the case of diapirs, gravitational instability is modeled. A diapir ascends towards the surface under the influence of buoyancy because it is less dense than the surrounding rocks. In the case of layered intrusion, the separation of melt from a crystal suspension in a magma chamber results from the “negative buoyancy” of the crystals compared to the liquid. During cooling of the magmatic liquid, minerals crystallize gradually (Figure I.1) until complete crystallization of the magma (all the material is solid).

The centrifuge is widely used in analogue modeling because it can be employed to model many geological processes where the driving force is gravity. Application of the centrifuge is based on the sedimentation principle, where the centripetal acceleration causes more dense substances to separate out along the radial direction (i.e. bottom of the sample) and inversely, lighter objects will tend to move to the top.

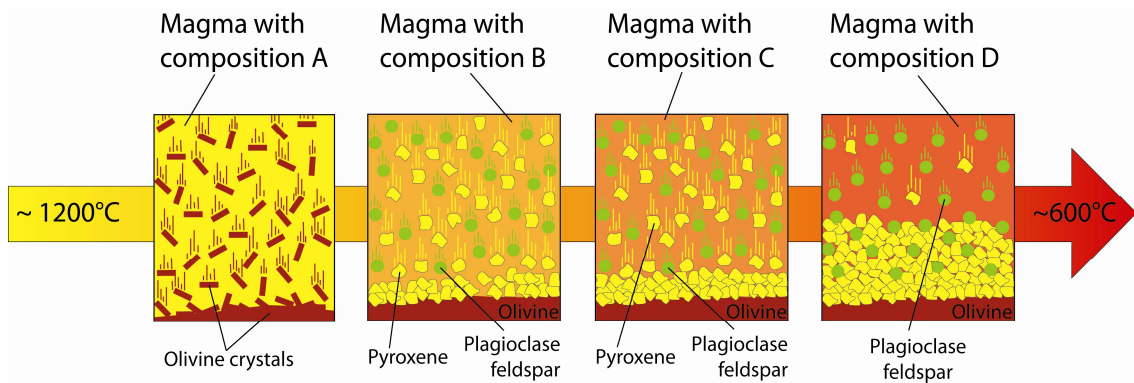


Figure I.1: Schematic representation of the crystallization during cooling of a magmatic liquid.

I.1.1 - Centripetal and centrifugal force

In a centrifuge, an object spins around a central axis. Due to the confinement within the machine, the object moves around the central axis (Figure I.2). The object provides a normal force that pushes the object toward the center of the circle. It is the centripetal force. The centripetal acceleration (a) is given by the formula:

$$a = \omega^2 \cdot r \quad (\text{Eq. I. 1})$$

where $\omega = v/r$ is the angular velocity and r is the radius, as derived from the Newton's second law, $F = m \cdot a$. The physical force F must be applied to an object with a mass m in order to produce acceleration (a). The force necessary to move at the velocity (v) on the circle with a radius (r) is:

$$F = -m \frac{v^2}{r} \quad (\text{Eq. I. 2})$$

The centrifugal force is the opposite force to the centripetal one. During an experiment, the denser materials in the sample have a greater centripetal force because of their larger mass (due to the formula: $F = m \cdot a$). Due to the higher centrifugal force at the bottom of the sample (because is farther from the central axis), the denser materials settle outside the circular pathway, which means at the bottom of the sample. Inversely for lighter materials, their mass is lower; the centripetal force is less important, and then remains closer to the top of the sample where the centrifugal force is weakest.

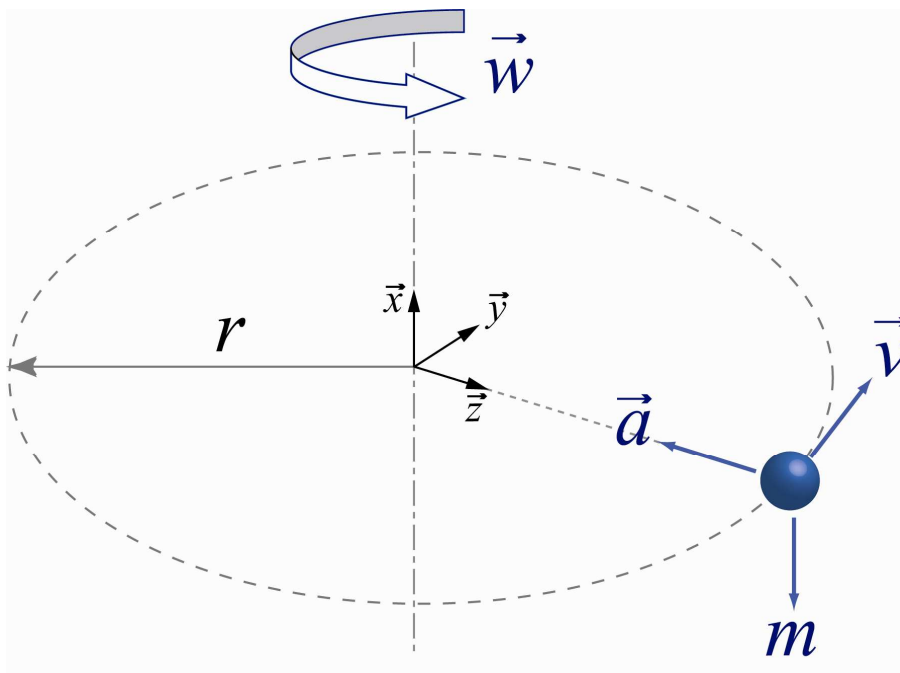


Figure I.2: Velocity and acceleration occurring on an object during the centrifugation. The velocity is tangent to the circle and the instantaneous acceleration always points towards the centre of the circle. The angular velocity is positive for an anticlockwise rotation.

Usually in literature, the value cited for the forces applied to an object during centrifugation is a relative one. In fact, this value is compared to the value that gravity on Earth would have on the same object. This ratio is called relative centrifugal force (RCF) and is equivalent to the centrifugation force divided by gravity force:

$$RCF = \frac{\omega^2 r}{g} \quad (\text{Eq. I. 3})$$

Commonly, the gravitational acceleration constant is expressed by the symbol “g” and is taken to be 9.80 m/s². One example of this principle: if the centrifuge spins at 10000 rotations per minute (rpm), we obtain, at 10 cm from the central axis, an acceleration around one thousand times greater than the gravity.

I.1.2 - Sedimentation principle.

Generally, in a solid suspension within a liquid phase, the particles tend to sink or rise to the surface according to their density and their size. It is because of gravity only:

$$F_d = mg \quad (\text{Eq. I. 4})$$

where F_d is the vertical force or gravitation, m the mass of the particles and g the gravitational acceleration. The particle velocity (v_s) – for a spherical particle in an infinite medium – is calculated according to the formula of Stoke’s (1851):

$$v_s = \frac{g(\rho_s - \rho_l) d^2}{18 \mu} \quad (\text{Eq. I. 5})$$

where $(\rho_s - \rho_l)$ corresponds to the density contrast between the solid (s) and liquid (l) phases, d is the particle size and μ the viscosity of the medium the particles travel through.

This particle settling is, in particular, very slow for fine grained particles in a very viscous liquid such as magma. During centrifugation, the separator power of the gravity field in replacing it by a radial centrifuge field enables the velocity of the particle settling to be increased significantly. When the gravity force is replaced, the centrifugal force becomes the vertical force (Eq. I.3). In the same way, the sedimentation velocity of the particles is modified and looks as follows:

$$v_c = RCF \cdot v_s = \frac{\omega^2 r (\rho_s - \rho_l) d^2}{18 \mu} \quad (\text{Eq. I. 6})$$

I. 2 - Centrifuges

The advantage of centrifuge modeling is that the analogue materials used for centrifuge experiments have a relatively high ratio of their strength to the applied stress. The disadvantage is that a centrifuge experiment is expensive. Furthermore, a centrifuge experiment cannot be observed directly during the course of centrifuging. Centrifuge modeling was first introduced to analogue modeling of geological processes by Bucky (1931). The centrifuge modeling technique took a great step forward in the early 1960's due to the work of Hans Ramberg, who built an entire analogue laboratory around a centrifuge (at University of Uppsala, Sweden). His work led to a better understanding of the role of gravity in deformation of the Earth's crust and lithosphere (Ramberg, 1967, 1981). From this time, centrifuge modeling has been widely used to investigate geological processes (Ramberg, 1970; Dixon, 1974, 1975; Talbot, 1977; Dixon and Summers, 1985; Koyi, 1988; Liu and Dixon, 1991; Koyi and Skelton, 2001). The centrifuge technique has dominated analogue modeling for some three decades, but has now largely been replaced by analogue models deformed in the normal field of gravity, in which much weaker materials are used (Koyi, 1997).

I.2.1 - How a centrifuge works technically

The basic centrifuge consists of a rotor holding the sample and rotating around a motor driven fixed axis. Some centrifuges are equipped with a pressure system, a furnace or are capable of creating a vacuum environment around the rotor. Two types of rotor are usually common in a centrifuge:

- Swinging-bucket rotor (Figure I.3), which is able to rotate within the centrifuge. When the speeds increase, the angle of the rotor perpendicular to the axis of rotation also increases, positioning it in a horizontal configuration. Inversely, as the centrifuge slows down, the rotor returns to a vertical release position. When the bucket swings out, the path length increases, allowing for improved separation of individual particles, particularly in density gradient centrifugation.

- Fixed-angles rotor (Figure I.4), generally simpler in design than the swinging-bucket rotor. The centrifuge samples are held at a specific and constant angle to horizontal plane.

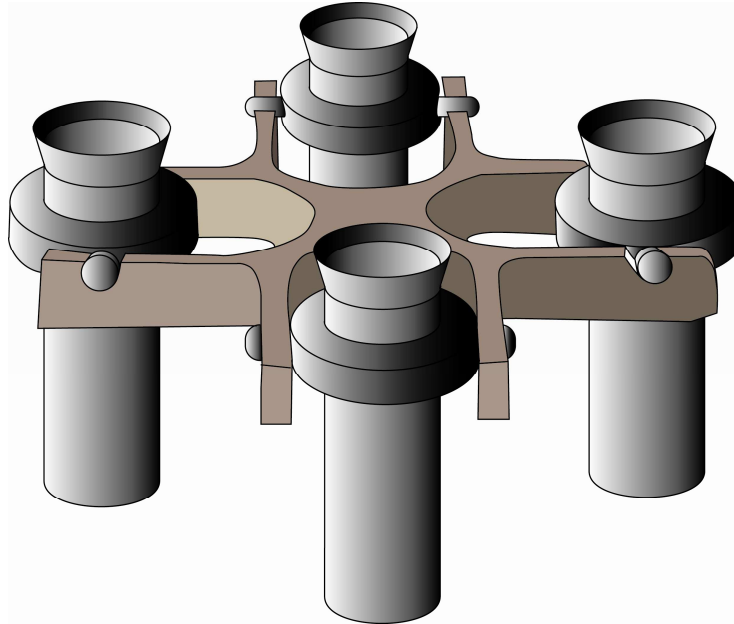


Figure I. 3: Schematic representation of a swinging-bucket rotor, where the containers move with the centrifugation speed.

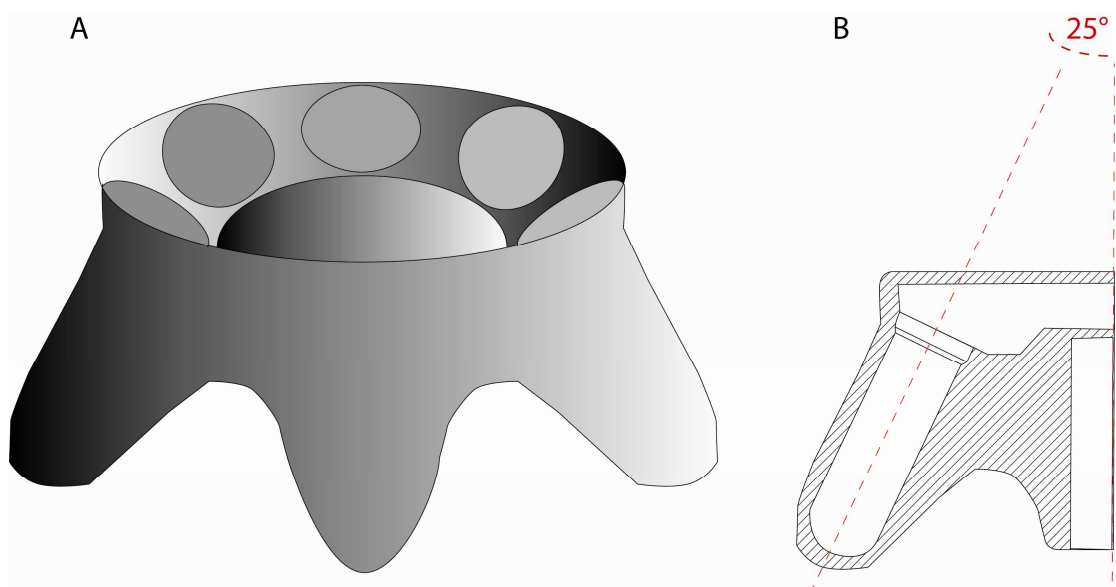


Figure I. 4: Schematic representation of a fixed angle rotor.

I.2.2 - Centrifuge used in this study

I.2.2.1 - Furnace centrifuge (Bayreuth, Germany)

One of the centrifuges used for the experiments presented here is the type “Centaur-2” (MSE Scientific Instruments™) where rotating furnaces have been added (Figure I.5). In fact, this centrifuge is equipped with a swinging-bucket rotor where the furnaces take the place of the containers. The rotation radius to the center of sample is approximately 124 mm.

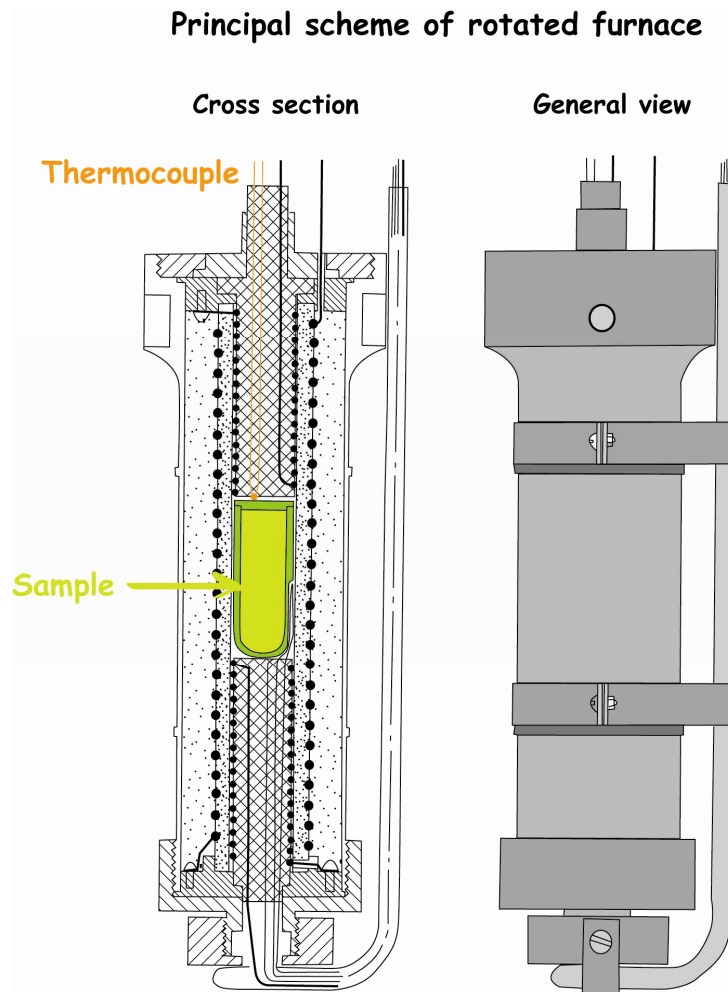


Figure I. 5: Representative scheme of the rotated furnace placed in the Bayreuth centrifuge.

I.2.2.2 - Centrifuging piston cylinder (Zürich, Switzerland)

The centrifuging piston cylinder results in a minimized 42 kg single-stage non end-loaded piston cylinder with bore diameter of 14 mm. The piston cylinder assemblies consist mostly of external NaCl and Pyrex sleeves and a straight graphite

furnace. The minimized piston cylinder is mounted onto a rotating table to get a radial assembly axis (Figure I.6). The maximum temperature for this centrifuge is approximately of 1250°C with a standard straight furnace. Higher temperatures can be reached with a stepped furnace. This piston cylinder centrifuge, particularly, has the ability to put the sample under pressure (max. 5 mm capsule outer diameter, max. 8 mm length). The pressure ranges between 3 and 18 kbar (0.3 – 1.8 GPa). The sample is sitting at a radius of 32 cm, so a maximum acceleration of 3000 g is reached at 2850 revolutions per minute (rpm).

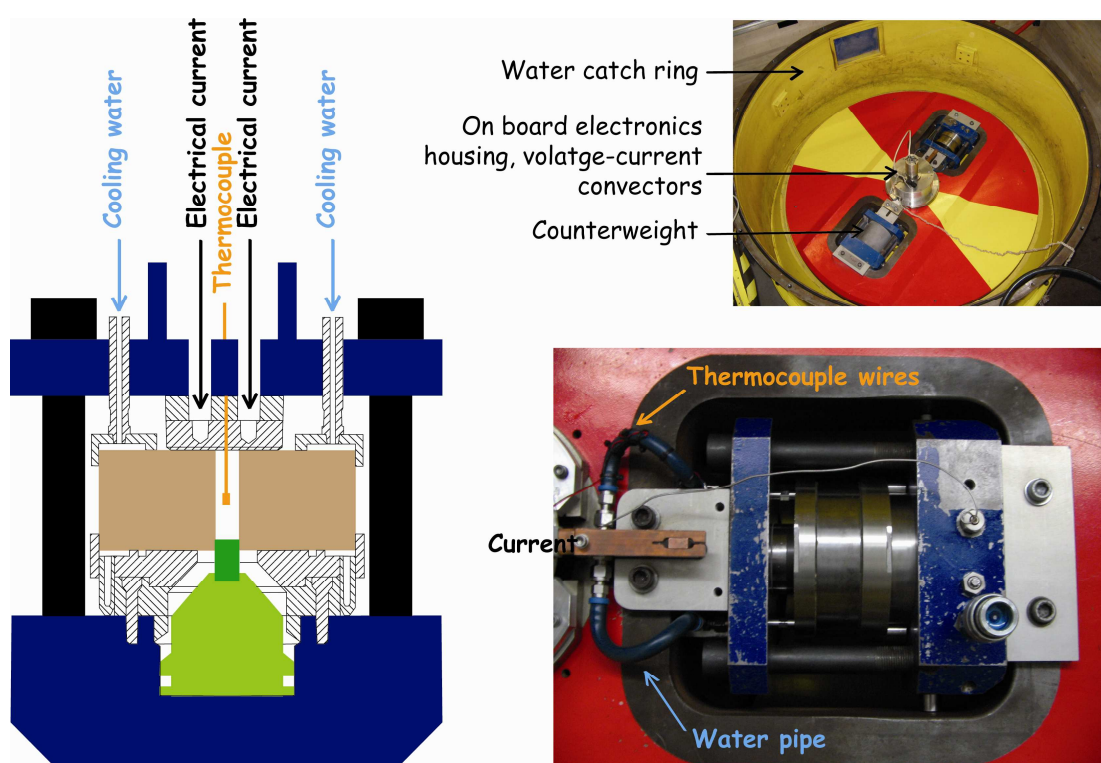


Figure I. 6: Representation of the centrifuging piston cylinder of Zurich. A. vertical cut of the piston cylinder introduced in the centrifuge. B. Top view of the centrifuge. C. Details of the emplacement of the piston cylinder.

1.2.2.3 - Centrifuge (Frankfurt, Germany)

The centrifuge used at Frankfurt University is an industrial centrifuge (Roto Silenta 630 RS, Andreas Hettich GmbH & Co) with a width of 813 mm and a depth of 1050 mm, equipped with a swinging-bucket rotor (Figure I.7). The distance from the centre of the turning axis to the bottom of the recipient is of 279 mm. The maximum speed is 4500 revolution per minute (rpm) and a maximum force (RCF) of 6498 g. The

models can have a maximum size of 90 mm in width and 150 mm in length, which corresponds to the dimensions of the inner container.

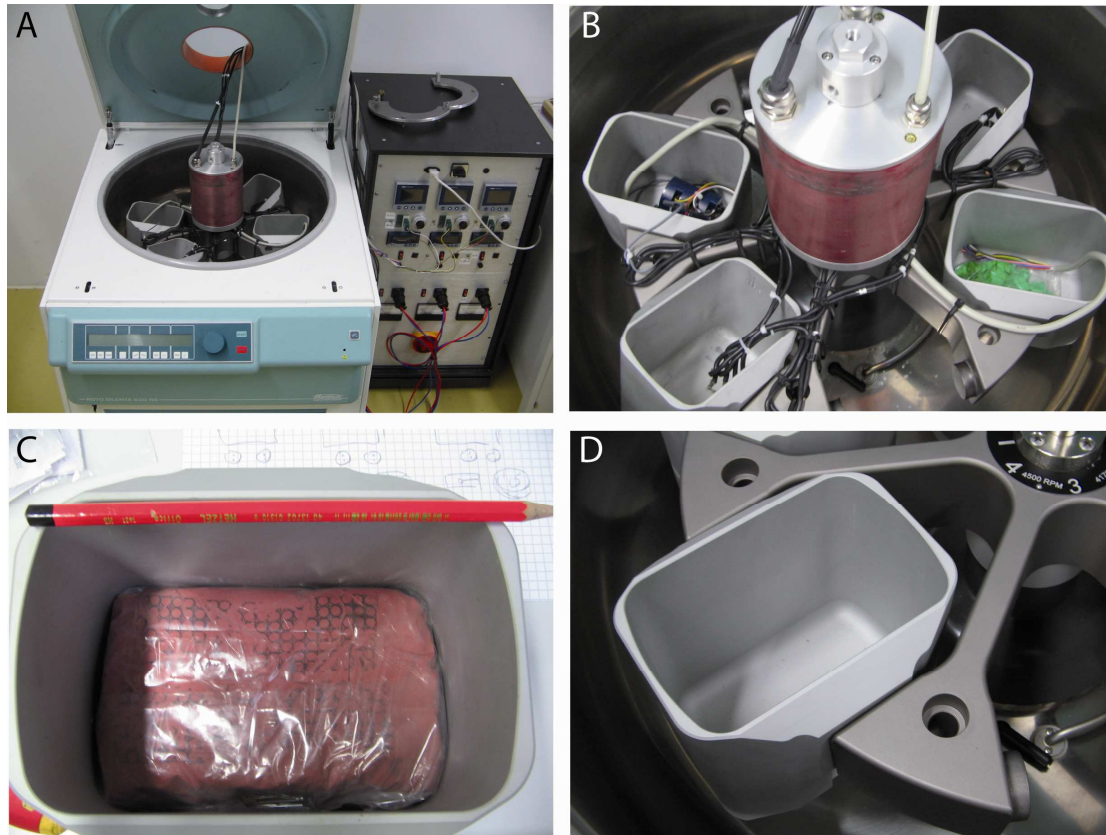


Figure I. 7: Different views of the centrifuge of Frankfurt. A. A general view of the centrifuge. B. General view of the swinging-bucket rotor. C. Details of one container with a model. D. Details of the swinging rotor with a container.

Chapter II

Pluton emplacement: the nested diapirs.

Table of contents

II.1 - INTRODUCTION	43
II.2 - EXPERIMENTAL PROCEDURE	44
<i>II.2.1 - Set-up of experiment 1 - without initial perturbations</i>	45
<i>II.2.2 - Set-up of experiment 2</i>	45
<i>II.2.3 - Set-up of experiment 3</i>	46
<i>II.2.4 - Set-up of experiment 4</i>	47
<i>II.2.5 - Set-up of experiment 5</i>	47
II.3 - EXPERIMENTAL RUN AND RESULTS OF THE EXPERIMENTS	48
<i>II.3.1 - Experiment 1 - without initial perturbations</i>	48
<i>II.3.2 - Experiment 2</i>	49
<i>II.3.3 - Experiment 3</i>	49
<i>II.3.4 - Experiment 4</i>	52
<i>II.3.5 - Experiment 5</i>	55
II.4 - SUMMARY	55

II.1 - Introduction

In this chapter, we investigate the diapiric ascent of buoyant material from two source layers at different depths, rising from protrusions at different positions within a model made from different silicone putties, in order to explain the origin of concentrically zoned, inflated plutons. Through these models, we wanted to test, if a rising diapir ascends straight upward or, if it might be deviated by a similar buoyant layer which is located within the overburden strata to follow the diapir stems developing from this layer (Figure II.1).

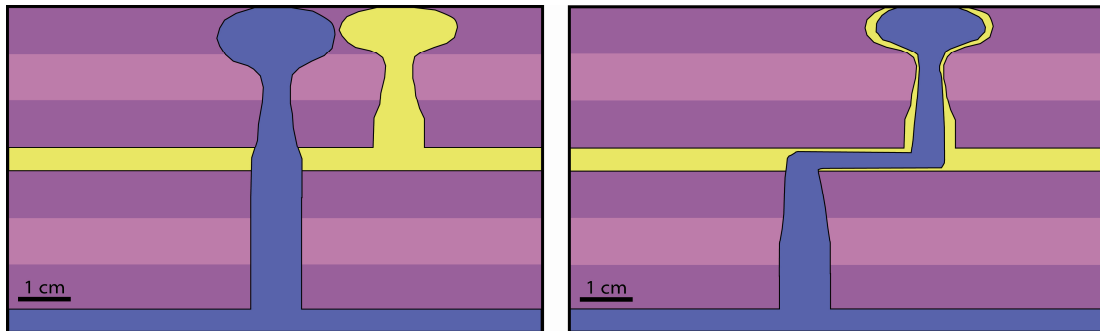


Figure II. 1: Profile sketches of the idealized and assumed pathways of diapirs from both the PDMS (polydimethylsiloxane) layer.

In the case of nested diapirs, the centrifuge has already been used earlier for modeling and is an important tool in understanding pluton ascent and emplacement (e.g. Dietl and Koyi, 2002, Cruden et al., 1995). The results of Dietl and Koyi (2002) show that nested diapirs can form by a combination of diapirism and subsequent “ductile dyking” of buoyant material through the stem of pre-existing diapirs. However, in this centrifuge model, the magma injections are successive and not contemporaneous (Figure II.2): after a first injection (in blue), the experiment was stopped in order to add a second layer for a second injection (in red) during the next centrifuging stage.

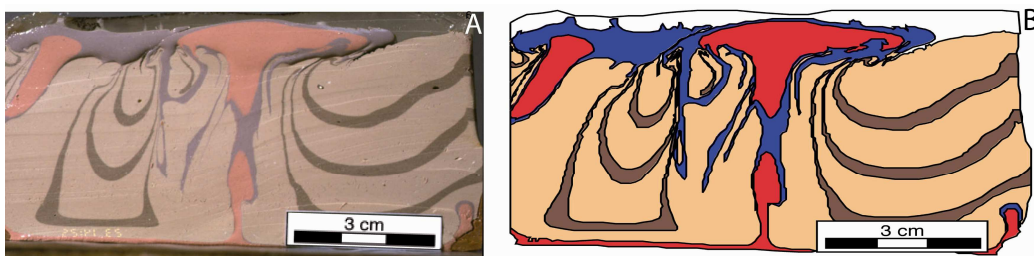


Figure II. 2: Experiment of nested diapirs of Dietl & Koyi (2002). A. Photograph of a cross section through the model centrifuged after emplacement of two buoyant layers. B. Drawing of the situation shown in Figure II.2.A.

II.2 - Experimental procedure

Centrifuge experiments were performed in order to study the rise of diapirs from two independent buoyant layers and the resulting internal structures within the overburden. The models were run with the centrifuge (ROTO SILENTA 630 RS, Andreas Hettich GmbH & Co, Germany) at the geophysics and structural geology laboratory of the Goethe University, Frankfurt (Main). The models have a rectangular geometry of 9 cm in width, 15 cm in length and 7 cm in height.

For this purpose, five models were constructed with the following general setup from bottom to top (Figure II.3):

- a buoyant layer of Newtonian polydimethylsiloxane (PDMS, stained in blue);
- an overburden, which consists of differently coloured denser layers with slightly different viscosities (for details see the specific paragraph of the individual experiments);
- a second buoyant layer (PDMS, stained in yellow);
- an overburden, which consists again of differently coloured, denser layers.

The overburden was stratified in order to visualise its internal deformation. A passive strain grid was printed on top of the models to record surface deformation. In order to prevent material leakage, the models were confined at the sides and at the bottom with plastic sheets. PDMS is a viscoelastic fluid with Newtonian properties (Doie and Edwards, 1978; Weijermars, 1986). The overburden was made from mixtures of so-called HK29, HK36 and HK40 (HK = “Hüpfender Kit” what means jumping putty) \pm plasticine and behaves as a viscoelastic Newtonian fluid with no plasticine added and as viscoelastic non-Newtonian fluid with plasticine added. For experiments 2 to 4, protrusions on top of both the PDMS layers were placed at different locations in each model to force the PDMS to rise from these instabilities. With different protrusion configurations, we aimed to control the ascent pathways of the diapirs and wanted to test if the individual diapirs interact with each other; e.g., if the diapirs from the lower source layer would use the upper source layer - and the stems of the diapirs rising from it – as pathways for their own ascent (Figure II.1). After centrifuging, the models were sectioned and photographed.

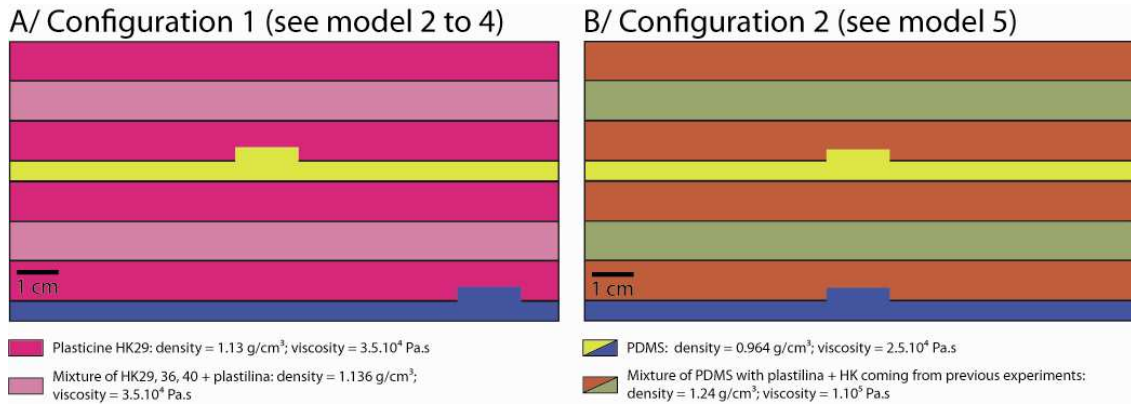


Figure II.3: Initial set-up of all four experiments for: A. Experiments 2, 3 and 4 (densities and viscosities of the overburden materials differ between experiments, see Table II.1) showing the stratified plastilina overburden and well-confined buoyant polydimethylsiloxane (PDMS) layers (yellow and blue). B. Experiment 5: note that the PDMS perturbations were positioned directly above one another.

II.2.1 - Set-up of experiment 1 - without initial perturbations

This model consists of (from bottom to top): a 5 mm thick lower layer (blue) of PDMS with a density $\rho = 0.964 \text{ g.cm}^{-3}$ and a viscosity $\mu = 2.5 \cdot 10^4 \text{ Pa s}$ (all viscosity data were measured at 20°C with a Rheolab QC viscometer at the structural geology laboratory of the Goethe University, Frankfurt/Main), a 10 mm thick layer of HK29 (with $\rho = 1.13 \text{ g.cm}^{-3}$ and $\mu = 3.4 \cdot 10^4 \text{ Pa s}$), followed by a 10 mm thick layer of a mixture of plastilina + PDMS + HK29, 36 and 40 – with $\rho = 1.136 \text{ g.cm}^{-3}$ and an approximate viscosity of $\mu = 3.4 \cdot 10^4 \text{ Pa s}$ at a strain rate of ca. 0.011 s^{-1} as it typical for this type of centrifuge experiments, followed by a 10 mm thick layer of HK29. This 30 mm thick stack of three layers served as overburden for the blue buoyant PDMS layer. On top of this 30 mm thick pile, we placed another buoyant PDMS layer of 5 mm thickness and another 30 mm thick alternating sequence of HK36 and the non-Newtonian material. The buoyant PDMS layer is meant to represent a partially molten rock ($\rho = 2.5 \text{ g.cm}^{-3}$ and $\mu \approx 8.5 \cdot 10^{18} \text{ Pa s}$), whereas the ductile overburden is used to simulate quite soft middle crust ($\rho = 3 \text{ g.cm}^{-3}$ and $\mu \approx 10^{20} \text{ Pa s}$). Model properties and scaling factors are summarized in Table II.1.

II.2.2 - Set-up of experiment 2

This model has basically the same setup as experiment 1 but with perturbations (see Figure II.3) on top of both the buoyant layers: the 5 mm thick layers (blue and yellow) of PDMS have a density $\rho = 0.964 \text{ g/cm}^3$ and a viscosity $\mu = 2.5 \cdot 10^4 \text{ Pa s}$. The

overburden consisted of a 10 mm thick layer of the Newtonian light pink HK36 ($\rho = 1.13 \text{ g.cm}^{-3}$ and $\mu = 3.4 \cdot 10^4 \text{ Pa s}$), followed by a 10 mm thick dark pink layer of a visco-elastic non-Newtonian material (a mixture of plastilina + PDMS +HK29, 36 and 40 – with $\rho = 1.136 \text{ g.cm}^{-3}$ and an approximate viscosity of $\mu = 3.4 \cdot 10^4 \text{ Pa s}$ at a strain rate of ca. 0.011 s^{-1} as is typical for this type of centrifuge experiment) and followed by a 10 mm thick layer of HK29. In order to govern the localisation of two diapirs, two perturbations were installed, one on top of each buoyant layer: for the bottom PDMS layer (in blue), the perturbation was in the centre of the model, whereas for the upper PDMS layer (in yellow), the perturbation was shifted to the side of the model (Figure II.3A).

Table II. 1: Properties of materials used for the individual experiments, i.e as overburden in all experiments plastilina + PDMS + several silicon putties; the buoyant layers in all four experiments consisted of PDMS. For experiment 3, the orange overburden units have a density of 1.27 g.cm^{-3} and a viscosity of $4 \cdot 10^5 \text{ Pa s}$. The red overburden units have a density of 1.136 g.cm^{-3} and a viscosity of $3.4 \cdot 10^4 \text{ Pa s}$.

Quantity	Experiments 1 & 2	Experiment 3	Experiments 4 & 5	Nature	Scaling
Thickness of overburden	30 mm			3000 m	10^{-5}
Thickness of buoyant layer	5 mm			500 m	10^{-5}
Density of overburden	1.136 g.cm^{-3}	$1.136 - 1.27 \text{ g.cm}^{-3}$	1.24 g.cm^{-3}	3 g.cm^{-3}	$0.37 - 0.41$
Density of buoyant layer	$0,964 \text{ g.cm}^{-3}$			2.5 g.cm^{-3}	$0,39$
Viscosity of overburden	$3.4 \cdot 10^4 \text{ Pa s}$	$3.4 \cdot 10^4 - 4 \cdot 10^5 \text{ Pa s}$	$1 \cdot 10^5 \text{ Pa s}$	10^{20} Pa s	$3.4 \cdot 10^{-16} - 10^{-15}$
Viscosity of buoyant layer	$2.5 \cdot 10^4 \text{ Pa s}$			$8.5 \cdot 10^{18} \text{ Pa s}$	$2.94 \cdot 10^{-15}$
Acceleration	6867 m/s^2			9.81 m/s^2	700

II.2.3 - Set-up of experiment 3

This model was built in the same way and as experiment 2: for the bottom PDMS layer (in blue) the perturbation is in a central position and for the upper PDMS layer (in yellow) the perturbation was shifted to the side of the model (Figure II.3A). The main difference with experiment 2 is that the three layers of the overburden are different in composition: the bottom and top layers were a viscoelastic, non-Newtonian

mixture of PDMS with plasticine and HK29 + HK36 + HK40 ($\rho = 1.136 \text{ g.cm}^{-3}$ and $\mu \approx 3.4 \cdot 10^4 \text{ Pa s}$), while the medium layer consisted only of Newtonian HK 36 (slightly denser and stiffer than the other overburden material of experiment 3: $\rho = 1.27 \text{ g.cm}^{-3}$ and $\mu \approx 4 \cdot 10^5 \text{ Pa s}$).

In contrast to experiment 2, this model was cooled down to 1°C in a refrigerator for 24 h before centrifuging in order to increase the overburden viscosity compared to the previous experiment. This experiment (in combination with experiment 2) aimed to study the effect of density and viscosity contrast between the overburden and the buoyant layer on the growth rate and rise of the smaller late-forming diapirs.

II.2.4 - Set-up of experiment 4

This model was built in the same way as experiment 2. The perturbation on top of the bottom PDMS layer (in blue) has a central position and for the upper PDMS layer, the perturbation was offset towards the side of the model (Figure II.3A). The main difference was that the density and viscosity of the entire overburden was changed to: $\rho = 1.24 \text{ g.cm}^{-3}$ and $\mu \approx 1 \cdot 10^5 \text{ Pa s}$ (see Table II.1).

In this model, the rheology and density of the two separate overburden layers is the same: they were only stained with different colours to make deformation structures within the overburden visible. With these changes, we wanted to investigate in more detail (and in combination with experiments 2 and 3) the role of viscosity and density contrast between the overburden and the buoyant PDMS layer

II.2.5 - Set-up of experiment 5

The overburden and buoyant materials applied in this experiment are the same as in experiment 4. The only difference lies in the fact that both perturbations on top of both the buoyant PDMS layers were located in the centre of model, one directly above the other, as shown in Figure II.3B. This change of perturbation position aimed to provide more information about the role of the position of the perturbations on top of the individual PDMS layers. In summary, the purpose and overall goal of all four differing setups was to gain as much information as possible about the development of nested and obviously diapiric structures, such as composite plutons and salt domes.

II.3 - Experimental run and results of the experiments

II.3.1 - Experiment 1 - without initial perturbations

The first experiment was carried out without protrusions on top of the buoyant PDMS layers, in order to compare and evaluate the role that perturbations play in diapir formation. Despite the lack of perturbations, first diapirs appeared at the surface of the model after 13 min of centrifuging at 700 g. Figure II.4A, B and C represent the map view and one cross section (1 – 1') of this experiment, respectively. The cross section shows that, in absence of imposed perturbations, the margins work as nucleation spots for diapir growth.

In order to know the natural spacing between two diapirs for the applied materials, we have calculated the dominant wavelength (λ) of the growing diapirs with the formula below:

$$\lambda = 2\pi * h_o * \left[\frac{\mu_o}{6\mu_b} \right]^{\frac{1}{3}} \quad \text{(Eq. II. 1)}$$

where μ_b and μ_o are the viscosity of buoyant layer and overburden layer, respectively, h_o the thickness of overburden layer.

The wavelength is an important factor in diapir growth because it controls the spacing of dome and anticlinal ridge. In this first experiment, the calculated dominant wavelength is ca. 11 cm. The difference between this theoretical value and the spacing observed in the model (ca 5 – 6 cm) is quite surprising but it can be explained by the diapir formation on the rims due to the margin effect. The two small diapirs, rising in the middle of the experiment (Figure II.4B and C), start their ascent relatively late during the model history. This can be concluded from the fact that they did not grow as far as those diapirs ascending along the margins of the model.

On the cross-section, it seems that the diapirs coming from the blue and yellow layers could interact with each other, but that is not the case. They will not be able to nest because the upper PDMS layer is thinner during the ascent of the diapir, coming from the yellow PDMS layer, and is deformed due to the rise of the blue diapir. This cross section shows, too, that the yellow PDMS layer is incorporated into the rim synclines of the rising blue PDMS diapirs. This experiment shows that it is possible for two diapirs to rise from two locations directly above each other (Figure II.4B and C) – as observed in experiment 5 (see below).

II.3.2 - Experiment 2

The model was placed in the centrifuge for 15 min at 700g until several diapirs appeared at the surface as observed from the deformed strain grid (Figure II.5A). It was then sectioned along the line 2-2' (Figure II.5A) in order to study its internal structure.

In cross-section (Figure II.5B and C), four mushroom-shaped diapirs formed in upper PDMS (yellow) layer; two are localised along the margins of the model, whereas the other two have grown from perturbations and coalesced directly below the surface on the left side of model (Figure II.5B and C). From the lower PDMS layer one large, three medium and three minor mushroom-shaped diapirs developed. The large diapir in the centre of the model developed from the perturbation site, whereas the other five diapirs are interpreted to have developed from minor random perturbations on its surface. From equation (II.1), the theoretical dominant wavelength for this experiment could be ca. 11 cm. The diapirs growing from lower PDMS layer have not used the stems of diapirs from the overlying PMDS layer as pathways, but have taken their own route upward.

During their rise from their respective source layers, the diapirs have deformed their overburden units and the overburden of the lower PMDS diapirs have, in turn, deformed the upper PDMS layer, too, causing the formation of rim synclines around each diapir (Figure II.5C). The synclinal shape of the upper PDMS layer is due, in part, to this deformation by the rise of the underlying (blue) PDMS diapirs.

II.3.3 - Experiment 3

The model was placed in the centrifuge and run for 6 min at 700 g. After this time, blue PDMS diapir pierced through the upper overburden. Other diapirs in the subsurface were indicated by distorted shape of the strain grid on the surface (Figure II.6A). A section was cut along the 3-3' line in Figure II.6A, which reveals two major mushroom-shaped diapirs from the upper (yellow) PMDS layer, one major diapir from

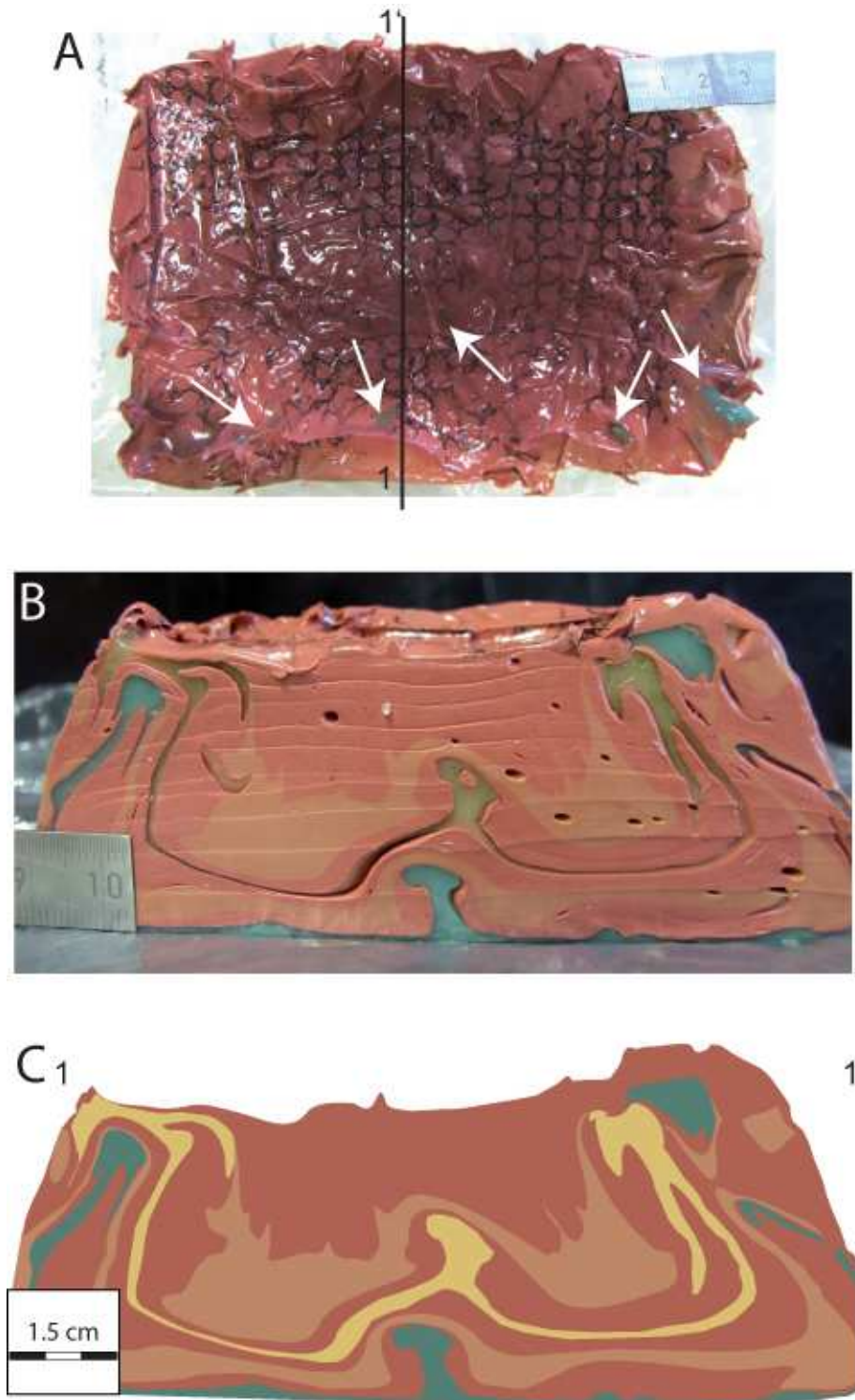


Figure II. 4: A. Plan view photograph of experiment 1- without initial perturbation on the top of the buoyant layer - after 13 min centrifuging at 700 g. A strain grid on top of the model is not deformed but the yellow PDMS diapirs have pierced the surface at several places (indicated by arrows). B. Photograph of a cross section through the model along line 1-1' in Figure II.4.A. The photograph shows two diapirs growing from their respective source layers which have the same localisation: they are one below the other. On the right side, we can see that two diapirs are growing from the respective source layers and are close to one to other without being nested. Both crosshatched areas correspond to the initial position of perturbations. C/ Drawing of Figure II.4.B.

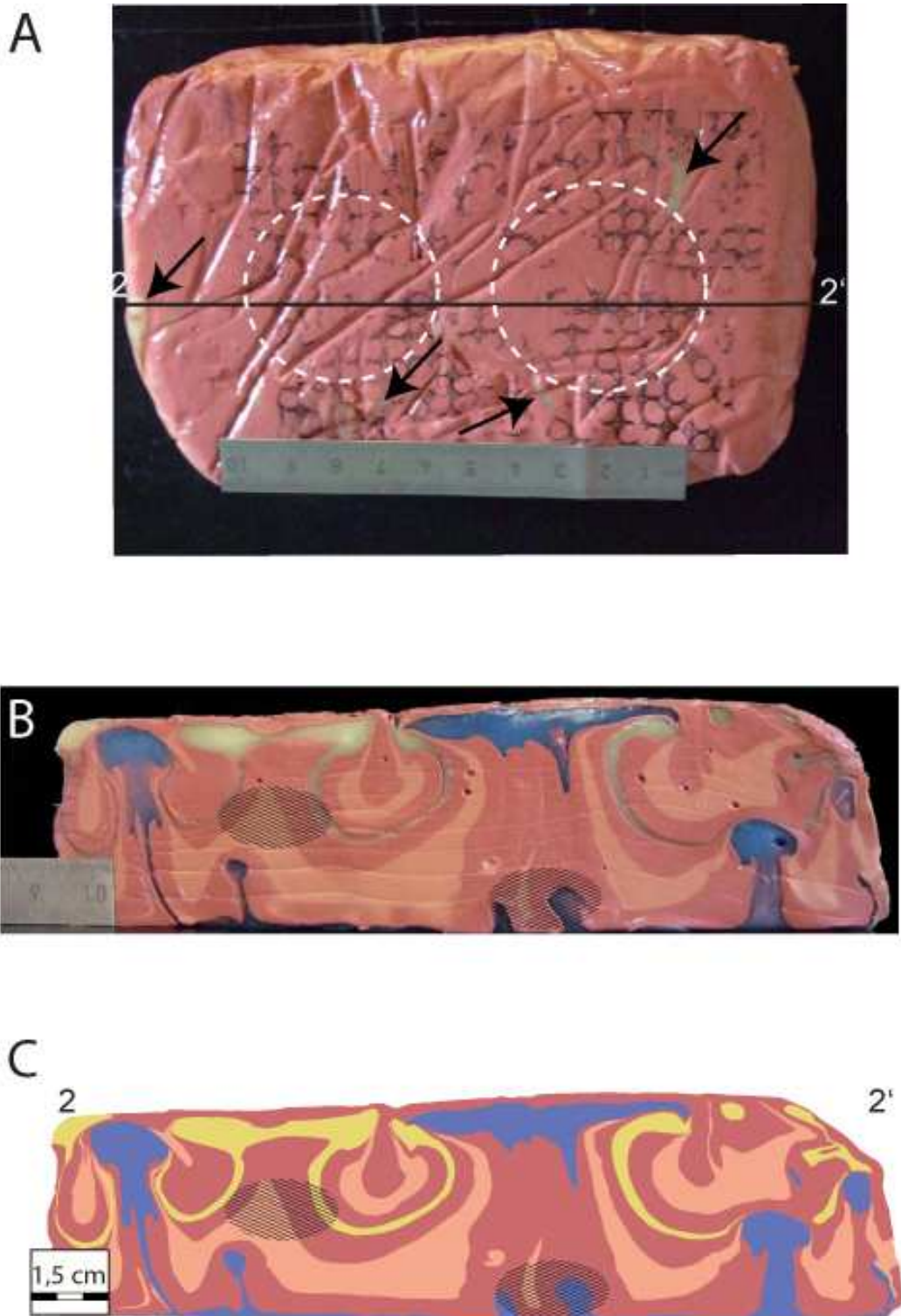


Figure II. 5: A. Plan view photograph of experiment 2 after 15 min centrifuging at 700 g. A strain grid on top of the model is only mildly deformed due to the emplacement of yellow PDMS diapirs, which have pierced the surface at several places (indicated by arrows). The white dashed circles indicate the location of the two major diapirs. B. Photograph of a cross section through the model along line 2-2' in Figure II.5A. The blue PDMS layer forms two major mushroom-shaped diapirs. A third diapir (far right) has started to rise, but ceased due to a limited amount of the buoyant material. Three other smaller blue diapirs are visible but result from Rayleigh-Taylor instabilities. Two diapirs also formed from the yellow PDMS layer. The passively stratified overburden was strongly deformed during the ascent of both layers and forms rim synclines around and in between the largest diapirs. The crosshatched areas correspond to the initial position of perturbations. C. Drawing of Figure II.5.B.

the underlying (blue) PDMS layer, and two small yellow and three small blue diapirs (Figure II.6B and C). One of the large yellow and the large blue diapir grew from perturbations imposed, and have coalesced directly below the surface of model (centre of Figure II.6B). The second large yellow diapir has risen along margin of model. The five small diapirs are interpreted to have developed from minor perturbations on the surface of the PDMS layers. The dominant wavelength calculated for this experiment from equation (II.1) is ca. 26 cm. As for experiment 2, the diapirs from lower PDMS layer have not taken the same pathway as the diapirs from the upper PDMS layer to reach top of model. During ascent, the diapirs deformed their overburden units, forming rim synclines in the upper part of model. The observed structures do not resemble composite plutons.

II.3.4 - Experiment 4

This model was placed in the centrifuge and run for 6 min at 700g until the first diapirs appeared at the surface of the model (two yellow and one blue diapir: Figure II.7A). A profile cut along section 4-4' in Figure II.7A shows that three major mushroom-shaped diapirs (two yellow, one blue) developed in the model, as well as two medium blue diapirs (Figure II.7B and C). One of the yellow diapirs has risen from the perturbation imposed on the model, and the second one – close to the model margin – results from Rayleigh-Taylor instability around a minor perturbation which developed during the experiment. The major blue diapir also developed from the perturbation imposed on the blue PDMS layer. Both medium-size diapirs have grown along the margin of the model. These diapirs are probably developed from minor perturbations on the surface of the blue PDMS layer. During the ascent, the diapirs have pierced through the overburden layers and deformed them into rim synclines (Figure II.7C). The result is the same as for both the previous experiments: each diapir took its own pathway upwards: none of the blue diapirs used the stem of a yellow diapir to move upward. From the equation (II.1), the theoretical calculated dominant wavelength is ca. 16 cm.

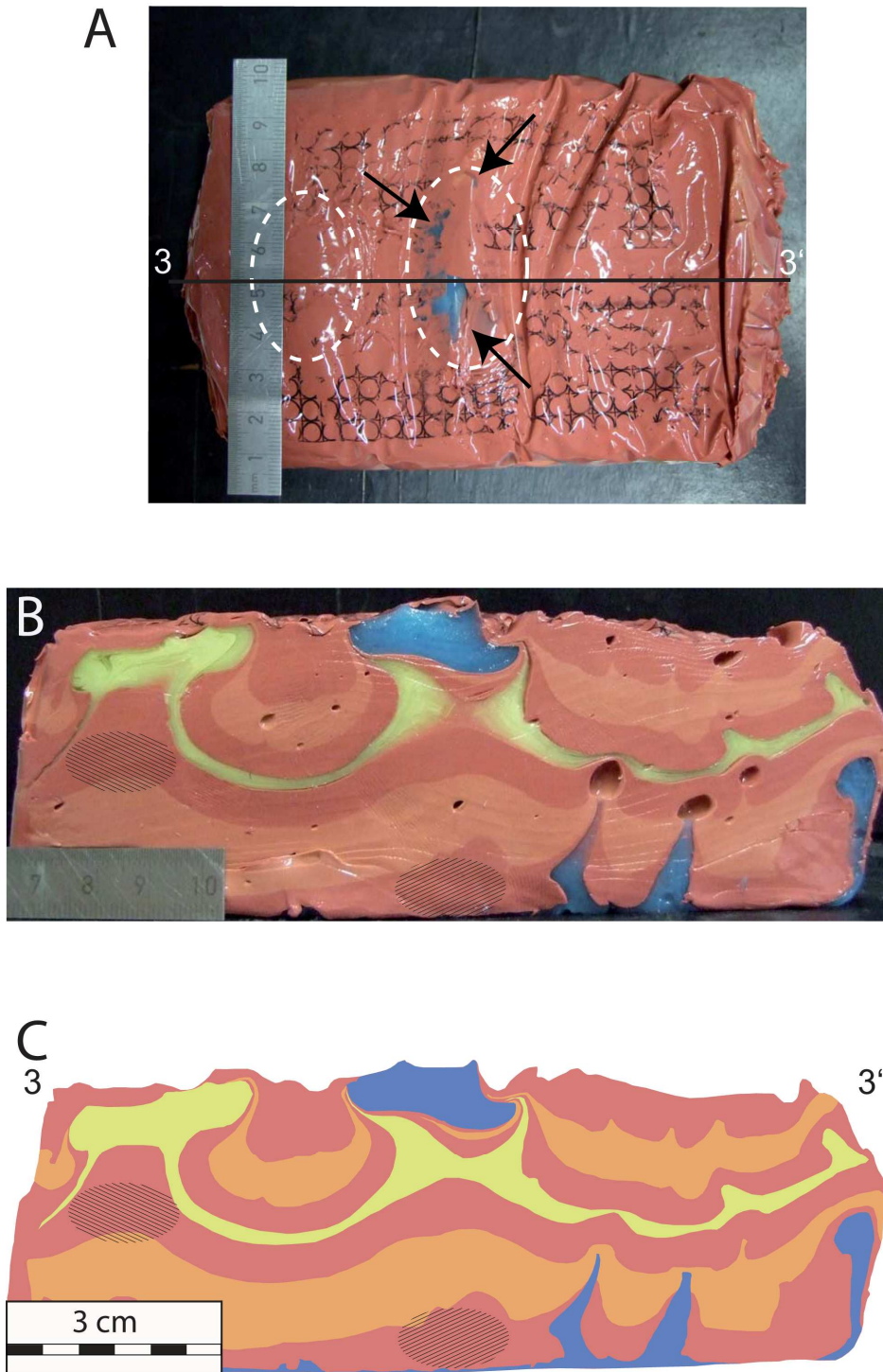


Figure II. 6: A. Map view photograph of experiment 3 after 6 min centrifuging at 700 g. A strain grid on top of the model was only weakly deformed due to the emplacement of the diapirs, but the blue PDMS pierces at several places through the overburden to reach the model surface (indicated by arrows). The major diapirs are localised within the white dashed circles. B. Photograph of a cross section through the model along line 3-3' in Figure II.6.A. The blue PDMS layer forms one major mushroom-shaped diapir, which reaches the surface and three smaller diapirs stems, which stopped growing after only 1.5 cm of rise due to shortage in supply of buoyant material. Moreover, two diapirs formed from the upper yellow PDMS layer. Observation of the picture shows that the blue diapir pierces through the yellow diapirs. The passively stratified overburden was strongly deformed during the rise of both PDMS layers and forms rim synclines around and in between the two large blue and yellow diapirs. The crosshatched areas correspond to the initial position of perturbations. C. Drawing of Figure II.6.B.



Figure II. 7: A. Map view photograph of the experiment 4 after 6 min centrifuging at 700 g. A strain grid on top of the model was weakly deformed due to the emplacement of the diapirs but the yellow and blue PDMS diapirs pierce at several places through the overburden to reach the model surface (indicated by arrows). The locations of the large diapirs are marked by the white dashed circles. B. Photograph of a cross section through the model along line 4-4' in Figure II.7A. The blue PDMS layer forms one large mushroom-shaped diapir which reached the top of the model and two smaller ones on the margins of the model which grew halfway through their overburden. Two diapirs grew from the upper yellow PDMS layer. The passively stratified overburden was strongly deformed during the rise of both layers and forms rim synclines around and in between the biggest three blue and yellow diapirs. The crosshatched areas correspond to the initial position of perturbations. C. Drawing of Figure II.7B.

II.3.5 - Experiment 5

This model was placed in the centrifuge and run for 4 min and 30 sec at 700 g. The experiment was stopped when deformation of the strain grid on the surface of the model became obvious (Figure II.8A). Despite similarities with experiment 4 regarding densities and viscosities, this experiment achieved maturity after a shorter run. In cross section 5-5' (Figure II.8B and C), two major mushroom-shaped diapirs - one blue and one yellow - have nested into each other. Four much smaller diapirs - two blue and two yellow - developed along the edges of the model, probably from little Rayleigh- Taylor instabilities in their respective PDMS layers due to rim effects. Both of the major, nested mushroom-shaped diapirs developed from the perturbations imposed on surface of each PDMS layer, which were arranged directly on top of each other. The overburden layers are deformed into two symmetrical rim synclines around the central nested diapirs. The major blue diapir that rose from the lower buoyant layer and pierced the already-formed upper (yellow) PDMS diapir also caused the flanking part of the yellow layer to sink down and become part of the rim syncline. While forming the diapir-in-diapir structure, the blue PDMS diapir pushed away the yellow diapir into two symmetrical halves (Figure II.8B and C).

II.4 - Summary

In this Chapter II, the interaction of simultaneously rising diapirs starting from different depths has been studied by analogue models in a centrifuge. Experiment 1 shows that without perturbations on top of the individual PDMS layers the positions of the growing diapirs are controlled by the dominant wavelength of the respective model system alone. Since the dominant wavelength of experiment 1 is ca. 11 cm, diapirs formed at the margins of the ca. 6 to 7 cm and in the center of the model. In experiment without initial perturbation, the dominant wavelength must control the spacing of domes and anticlinal ridges, but in our experiment, the main diapirs are formed due to the margin effect.

In 1981, Ramberg has shown that the dominant wavelength is proportional to the buoyant layer thickness: the thicker the layer, the wider the spacing of the domes. He has shown too, that if the overburden thickness is of the same order as the wavelength, then decreasing thickness should lead to shortening of the characteristic wavelength.

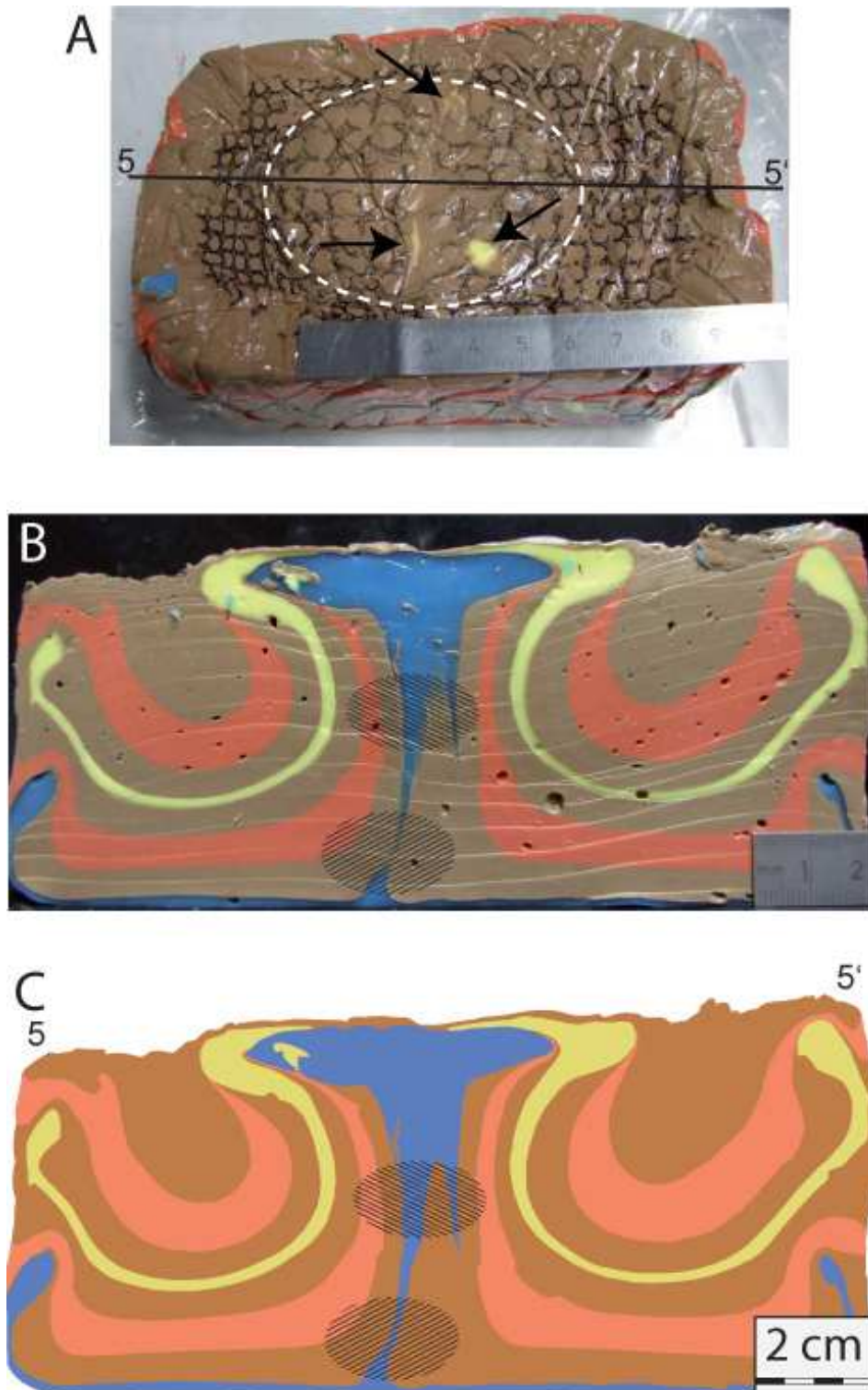


Figure II.8: A. Map view photograph of the experiment 5 after 4 min 30 sec centrifuging at 700 *g*. A strain grid on the top of the model is completely deformed in the centre of the model due to diapir emplacement of the diapirs. The yellow PDMS layer pierces through the surface of the model (indicated by arrows). The white dashed circle defines the location of the diapirs. B. Photograph of a cross section through the model along line 5-5' in Figure II.8.A. The yellow and blue PDMS layers each form one large tabular diapir with the blue one intruding its yellow precursor. Two small diapirs grew from both PDMS layers along the margins of the model. The passively stratified overburden was strongly deformed during the rise of both layers and forms rim synclines around the diapir-in-diapir structure. Moreover, screens of overburden material are incorporated within the nested PDMS diapirs. Both crosshatched areas correspond to the initial position of perturbations. C. Drawing of Figure II.8B.

Later, Schmeling (1987) demonstrated how the dominant wavelength and the geometry of the gravity overturns are influenced by the shape of the initial perturbation. Finally, in 2001, Ismail-Zadeh showed that when the viscosity of non Newtonian overburden is rather high, the dominant wavelength tends to diminish when the thickness of the overburden exceeds the buoyant layer thickness. He showed that the dominant wavelength is short when the overburden is thin, and with a large effective viscosity ratio its length increases with overburden thickness. In experiments 2-5, with perturbations on top of both buoyant layers, those protrusions control the nucleation positions of most diapirs in the individual experiments.

In contrast to experiment 1, the distance between diapirs in experiments 2-4 is smaller than predicted by the dominant wavelength equation (II.1) because it is strongly controlled by the initial perturbations on the top of the buoyant layers. The rising diapirs of these experiments, in particular those from models 2-5, are mushroom-shaped. Moreover, the diapirs that rose up from the lower PDMS layer cut the upper PDMS layer when the initial protrusion positions were not vertically aligned (Figure II.5, Figure II.6 and Figure II.7), whereas they formed a nested diapir-in-diapir structure when they were aligned (Figure II.8).

During, or after, the rise of the initial diapirs, some smaller diapirs developed from minor perturbations on the surfaces of the PMDS layers, whereby their final, limited height is probably a function of the limited supply of buoyant material. During the rise of different mushroom-shaped diapirs, the overburden units are deformed into rim synclines around the diapirs. Experiments 2 to 4 differ mainly in density and viscosity of the overburden. These differences in material properties have some consequences on the experiments in terms of diapir growth rate, dominant wavelengths (for experiments 2, 3 and 4, the dominant wavelengths are ca. 11, 26 and 16 cm, respectively) and rise of smaller later-forming diapirs. Moreover, it is widely recognized that the increase of the density contrast leads to an increase of the ascent rate (Kukowski and Neugebauer, 1990) and influences the diapir's shape (Römer and Neugebauer, 1991). Generally, we see that the higher the viscosity contrast, the fewer the diapirs (Woidt, 1978; Ramberg, 1981). In our study, the fourth experiment illustrates very well this last principle. In fact, the viscosity contrast between overburden and buoyant material is more pronounced in the medium layer of the overburden than for the other two layers underneath and above. In cross section (Figure II.7B and C), we have observed that the diapirs grow from the buoyant layers through the first overburden

layer (where the viscosity contrast is relatively low) but are stopped at the medium layer (where the viscosity contrast is higher). Moreover, the higher the viscosity contrast, the fewer the diapirs that develop. Consequently, the growth times for the diapirs to reach the model top differ between the experiments. For example, in the second experiment, the diapir pierces the model top in 15 min and the viscosity contrast is 1.36. On the other hand, in the fourth experiment, the diapir reaches the model top in 6 min and the viscosity contrast is 4.

Experiment 2 is the slowest of all three experiments with an offset between the upper and the lower perturbation. It is because experiment 2 depicts the lowest density contrast of all three experiments. On the other hand it also has quite a low viscosity contrast, while should allow the buoyant material to grow quite fast. Another surprising observation from these 3 experiments with offset perturbations was the behaviour of experiment 3: here, the increase in overburden viscosity should have decreased the ascent rate more significantly than the increase in density difference accelerated the process. However, this was not the case. A possible explanation for this observation is that in experiment 3, the overburden consisted of 3 layers of different viscosity and density: the bottom and top layer have the same viscosity and density contrast as experiment 1 (1.36 and 1.18, respectively) but the medium layer has stronger viscosity and density contrast (16 and 1.32, respectively). Consequently, the diapir ascends easily through the first layer but not through the middle layer. For that reason, the diapir ascent through the medium layer of overburden takes far more time than through the bottom and top overburden layers.

Chapter III

The settling and compaction of olivine.

Table of contents

III.1 - INTRODUCTION	61
III.2 - EXPERIMENTAL AND ANALYTICAL TECHNIQUES	61
<i>III.2.1 - Experimental strategy</i>	61
<i>III.2.2 - Experimental techniques</i>	61
<i>III.2.3 - Analytical techniques</i>	63
III.3 - RESULTS	65
<i>III.3.1 - Crystal distribution after static annealing</i>	65
<i>III.3.2 - Porosity profiles through the olivine layer</i>	65
<i>III.3.2.1 - Stokes settling of the olivine suspension</i>	66
<i>III.3.2.2 - Compaction of the cumulate</i>	66
<i>III.3.3 - Grain growth</i>	72

III.1 - Introduction

In this study we experimentally form cumulate layers of olivine from suspension in basaltic melt first by mechanical and then by chemical compaction. This allows us to evaluate mechanisms and formation times of ortho- and adcumulates.

While the concepts of settling and compaction are intriguingly simple, they pose hideous experimental problems: at 1 *g*, buoyancy forces on crystals in silicate melts do not dominate crystal distributions in experimental systems. Instead, unavoidable temperature gradients cause chemical diffusion due to saturation gradients, crystals dissolve in the hot zone of a capsule and re-precipitate in the cold zone, resulting in a mostly temperature-dominated rearrangement of crystals at ambient gravity (Leshner and Walker, 1988, see Figure 1). Further complexity arises from Soret diffusion, also induced by temperature gradients (Chipman, 1926; Leshner, and Walker 1988; Cygan and Carrigan, 1992). To overcome the effects of temperature gradients on crystal distribution, gravitational forces have been amplified by employing the centrifuging piston cylinder at 400-1500 *g*.

The goal of this chapter is not to decide which cumulate formation mechanism is prevalent in nature, but rather to investigate the mechanics and time-scale of gravitationally driven crystal settling and compaction, to understand the feasibility of this process for (layered) intrusions.

III.2 - Experimental and analytical techniques

III.2.1 - Experimental strategy

First, static annealing experiments were performed on a mixture of 30 % olivine and 70 % melt to measure crystal size and distribution at static conditions. After establishing a satisfying experimental protocol for obtaining a homogeneous initial crystal distribution, each further experiment was at first statically annealed according to this protocol. The capsules of these annealing experiments were then reloaded into the centrifuging piston cylinder, heated to the same temperature, and then centrifuged for the desired amount of time and gravity acceleration.

III.2.2 - Experimental techniques

The starting material was a 30:70 vol% olivine:MORB mixture of natural San Carlos olivine and synthetic simplified MORB glass with a Mg# of 0.79 (Table III.1). Olivine powder was obtained through crushing and subsequent milling for a few hours. The final grain size was measured through laser diffractometry on dispersed solutions ('Mastersizer 2000' instrument, Malvern Instruments Ltd.). The grain size distribution curve of the starting olivine for the OB and ZOB series (Table III.2) yields an average size of $\sim 1.8 \mu\text{m}$. For a second series (FF, Table III.2), initial grain sizes were varied and were 26, 36, and $51.5 \mu\text{m}$. The MORB glass was obtained from melting synthetic oxide powders at $1300 \text{ }^\circ\text{C}$ and an oxygen fugacity of $\log(f_{\text{O}_2}) = -6.704$ yielding an $\text{Fe}^{3+}/\text{Fe}^{2+}$ ratio corresponding to QFM at $1300 \text{ }^\circ\text{C}$, 1 GPa. The glass was then crushed, milled, and thoroughly mixed with olivine.

Static annealing experiments were performed in an end-loaded piston cylinder with a 14 mm bore, employing double Pt-graphite capsules with an inner diameter and height of 2.0 and 1.0 mm. Piston cylinder assemblies consisted of external NaCl and Pyrex sleeves, a straight graphite furnace (6.0 mm I.D., 36 mm length), and inner crushable MgO cylinders containing the capsule and mullite thermocouple ceramics. B-type Pt-Rh thermocouples were separated from the Pt-capsule by a 0.6 mm corundum disk and the temperature controlled at an accuracy of $\pm 5^\circ\text{C}$. Pressure was calibrated against fayalite + quartz = orthoferrosilite (Bohlen et al., 1980) and the quartz-coesite transition (Bose and Ganguly, 1995). Temperature was ramped down manually with a rate of ca. $50^\circ\text{C}/\text{s}$. Experiments were carried out at 1270 or 1280°C and 1.0 GPa (Table III.2). For annealing, these conditions were kept for 20-22 h for an initial grain size of $1.8 \mu\text{m}$, 72 h for larger grain sizes, and in one case 275 h (Table III.2). The latter experiment was intended for growing large grains, but resulted in one $\sim 500 \mu\text{m}$ grain stuck to the capsule roof and a rather homogeneous remainder of nicely settled crystals of $12.3 \pm 5.3 \mu\text{m}$ (after centrifugation).

The centrifuging piston cylinder consists of a minimized 42 kg single-stage piston cylinder with the same bore diameter and assembly as for the static runs. This piston cylinder is mounted into a rotating table such that the assembly axis is radial, the thermocouple towards the center, the bottom of the metal capsule facing the thermocouple, acceleration thus being directed towards the metal capsule lid. The inner graphite capsule has its lid towards the thermocouple (also during annealing), such that acceleration is directed towards the bottom of the graphite capsule. The sample is at a radius of 32 cm, the maximum acceleration used in this study of 1500 g being reached

at 2030 revolutions per minute (rpm). Centrifuge experiments were carried out at 1270-1280°C, 0.8-1.1 GPa, and accelerations of 200-1500 g for a maximum duration of 50 hours. Heating through the slip ring stack of the centrifuge is only advisable when the table is rotating and thus centrifuge experiments include two steps: first the piston cylinder is pressurized to 0.4 GPa, the table run at 200 rpm (15 g), and the assemblage heated to soften the pyrex glass and collapse the assembly's porosity at 600°C. Temperature is then ramped down, the table stopped, and pressure increased such that after heating and thermal equilibration of the assembly, the desired final 1.0 GPa is achieved. The somewhat variable final run pressure (Table III.2) results from the fact that this procedure was established during this series of experiments and that pressure adjustments during centrifugation are not possible, thus necessarily allowing for the characteristic pressure losses of salt + pyrex assemblies with time. Nevertheless, the amount of crystals in the olivine + MORB system is fairly insensitive to the small pressure fluctuation, thus this slight variation does not influence our experimental results (see also Connolly et al., 2009).

III.2.3 - Analytical techniques

Polished sections of the run products were imaged with backscattered electron beam (BSE) and chemically characterized with wavelength dispersive spectrometry (WDS) employing a Jeol JXA-8200 electron microprobe. WDS analyses of olivine were operated with a 15 kV, 20 nA focused beam. For melt analyses, 15 kV, 5 nA, and a beam size of 10 μm were employed.

Melt abundances along the capsule were obtained through digital analysis of BSE images with the software "Image Tool" (UTHSCSA Image Tool, The University of Texas Health Science Center in San Antonio). For this purpose, BSE images were converted to binary images. The crystal bearing part of the capsule was then sliced in 4 or 7 segments perpendicular to the capsule axis and analyzed for crystal size and distribution. Image analysis was repeated three times for several areas on each sample to evaluate average errors on melt abundances within a slice. Measurements of melt abundances in the crystal layer were limited to the axial region (50-60 % of the capsule diameter) to avoid boundary effects when settling crystals or rising liquid interfere with the capsule walls (Botto et al., 2005; Tatum et al., 2005).

Table III.1: Melt and crystal starting compositions

Oxides	MORB	San Carlo	Melt – OB6	Olivine-OB6
SiO ₂	51.8	41.0	50.2	40.1
Na ₂ O	1.92	0	1.95	0.02
TiO ₂	2.52	0	2.30	0.07
K ₂ O	0.53	0	0.50	0
FeO	5.19	8.96	6.20	7.18
Al ₂ O ₃	14.9	0	13.7	0.08
MgO	11.4	49.8	13.9	52.1
CaO	11.3	0	11.2	0.30
MnO	0.04	0.23	0.07	0.06
Total	99.6	100.0	100.0	100.0
Mg#	0.797	0.908	0.800	0.922

Table III.2: Run conditions and results.

Experiment	T (°C)	P (GPa)	annealing time (h)	acceleration (a) (x 9.81 m/s)	centrifuging time (t) (h)	a * t (m/s)	height crystal layer (h) ¹ (µm)	total porosity crystal layer (vol%)	porosity bottom layer (vol%)	Initial grain size (µm)	Final mean grain size (µm)
OB-14	1270	1.0	24	1	-	-	-	65.9 (2.1)	67.1 (2.1)	1.8	13.1 (2.5)
OB-6	1270	1.0	72	1	-	-	-	64.5 (2.0)	64.0 (2.1)	1.8	19.1 (2.4)
ZOB 9	1280	1.0	21	200	1.00	0.72 x 10 ⁶	620	53.5 (4.1)	51.6 (1.7)	1.8	13.1 (5.3)
ZOB 6	1280	0.8	20	200	3.00	2.16 x 10 ⁶	625	55.3 (2.4)	51.9 (2.1)	1.8	13.3 (2.5)
ZOB 1	1280	1.1	22	400	6.00	8.64 x 10 ⁶	450	49.9 (2.4)	46.1 (1.8)	1.8	14.4 (2.5)
ZOB 11	1280	1.0	21	1500	1.67	9.00 x 10 ⁶	640	38.2 (3.0)	35.4 (2.3)	1.8	11.0 (6.6)
ZOB 5	1280	0.9	21	700	10.00	25.2 x 10 ⁶	450	42.5 (2.0)	37.4 (1.9)	1.8	14.7 (2.1)
ZOB 10	1280	1.0	275	1500	4.67	25.2 x 10 ⁶	420	38.9 (4.3)	37.3 (2.4)	1.8	12.3 (5.3) ²
ZOB 4	1280	0.9	21	400	50.00	72.0 x 10 ⁶	560	36.7 (2.1)	31.2 (2.0)	1.8	18.6 (2.3)
FF01	1280	1.0	72	700	10.00	25.2 x 10 ⁶	740	42.1 (2.0)	42.5 (4.4)	26	33
FF05	1280	1.0	72	700	10.00	25.2 x 10 ⁶	730	43.4 (1.0)	37.4 (5.4)	36	47
FF04	1280	1.0	72	700	10.00	25.2 x 10 ⁶	730	43.5 (1.4)	41.9 (5.6)	51.5	64

¹Height of crystal layer above the centre of the bottom segment within the crystal pile²This experiment contains one large 500 µm grain, which is not considered for the mean grain size

III.3 - Results

III.3.1 - Crystal distribution after static annealing

The static annealing experiments did result in a homogeneous spatial distribution of crystals if limited to 24 h at 1270-1280°C (Figure III.1A). After 24 h, the final average grain size is $13.1 \pm 2.5 \mu\text{m}$ when the starting grain size was $\sim 1.8 \mu\text{m}$. The melt content is then $65.9 \pm 2.1 \text{ vol}\%$ which compares to 70 vol% melt in the starting material. The small difference in melt percentage is readily explained with a temperature dependent solubility of olivine, our starting basalt melt being slightly oversaturated in olivine at 1270°C. The crystal size and spatial distribution as shown in Figure III.1a, represents the texture of our sample when starting centrifuging.

Longer static annealing times of 72 h led to an increased average grain size of $19.1 \pm 2.4 \mu\text{m}$ and results unavoidably in an uneven distribution of olivine within the capsule (Figure III.1b). Olivine grains formed a dispersed and homogeneous layer in the lower 2/3 of the capsule, but a zone with significantly less crystals in the upper part and a zone with crystals above average grain size at the capsule top. The Stokes settling velocity for olivines of 13 to 19 μm in diameter in a basaltic liquid at 1280°C is from 8.2 to 17.5 $\mu\text{m}\cdot\text{h}^{-1}$, which could be attributed to pure melt zone formation of about 150 μm in height for grains growing with time from initial to their final size after 72 hours. However, at the beginning, the dense suspension of olivines settles only at about 1/10 of the Stokes velocity (Schwindinger, 1999), and later, the crystal-poor zone forms within the suspension and not at the top. We thus conclude that the crystal-poor zone forms through a chemical rather than mechanical process. Most likely, this zone corresponds to the hot zone in the capsule where crystals are dissolved due to saturation gradients and then re-precipitated during grain growth in the adjacent colder regions (Leshner and Walker, 1988). Clearly, long static experiments lead to a spatial crystal distribution that is not governed by simple gravitational crystal settling.

III.3.2 - Porosity profiles through the olivine layer

Statically annealed, homogeneous and texturally equilibrated samples (as in Figure III.1A) were centrifuged with varying acceleration and centrifugation time from 200 to 1500 g and from 1 to 50 hours, respectively (Table III.2). Except of the settling experiment ZOB9, all other centrifuge experiments caused the total of the crystals to

accumulate in a single olivine layer, leaving a homogeneous crystal free basalt layer in the gravitational top of the capsule (Figure III.2). This top melt layer is of no further interest to this study. Porosity profiles through the cumulate layer are given in Figure III.3. These profiles show a linear porosity (ϕ) vs. height (h) relation, except for the uppermost part which has a significantly lower porosity (Figure III.3). Absolute porosities determined from image analysis have analytical errors of typically $\pm 1-2.5\%$ (1σ). The porosity difference $\Delta\phi$ between the uppermost and second segments amounts to 3-8 vol%, and thus the slope $d\phi/dh$ from the top to the second layer is poorly defined. Thus this feature will not be exploited further. Instead, this study focuses mostly on the Stokes settling of sinking olivine grains and secondly on the chemical compaction of a basal olivine layer in the cumulate pile.

III.3.2.1 - Stokes settling of the olivine suspension

The settling velocity of the dense suspension of olivine crystals can be determined from the travel distance of the uppermost crystals of the olivine suspension. As long as the porosity of the top olivine layer remains constant and equal to the bulk porosity, one can assume that these olivine grains are effectively in suspension and do not pile up along grain contacts. To obtain a crystal layer in which the top part has olivines with a similar crystal density to that after static annealing, centrifugation had to be decreased to 200 g, 1 h. In this experiment (ZOB9, Table III.2, Figure III.2a), the melt layer above the olivine layer has a thickness of $300\pm 30\ \mu\text{m}$. Hence, the settling velocity of the dense olivine suspension, recalculated for an acceleration of 1 g, is approximately $4.17\cdot 10^{-10}\ \text{m s}^{-1}$. For comparison, the Stokes' velocity at 1 g for this experiment is equal to $2.31\cdot 10^{-9}\ \text{m s}^{-1}$.

III.3.2.2 - Compaction of the cumulate

For each experiment, the total force applied to the olivine in the lowermost segment of the cumulate is proportional to $\Delta\rho^{(\text{olivine-basalt})}\cdot h\cdot a\cdot t$, where $\Delta\rho^{(\text{olivine-basalt})}$ is the density contrast between crystal and melt, h the thickness of the olivine layer above the lowermost segment, a the experimental acceleration, and t the time over which the centrifuge acceleration is applied. $\Delta\rho^{(\text{olivine-basalt})}\cdot h\cdot a\cdot t$ is equivalent to pressure multiplied by time. Three observations on the crystal content and the crystal content

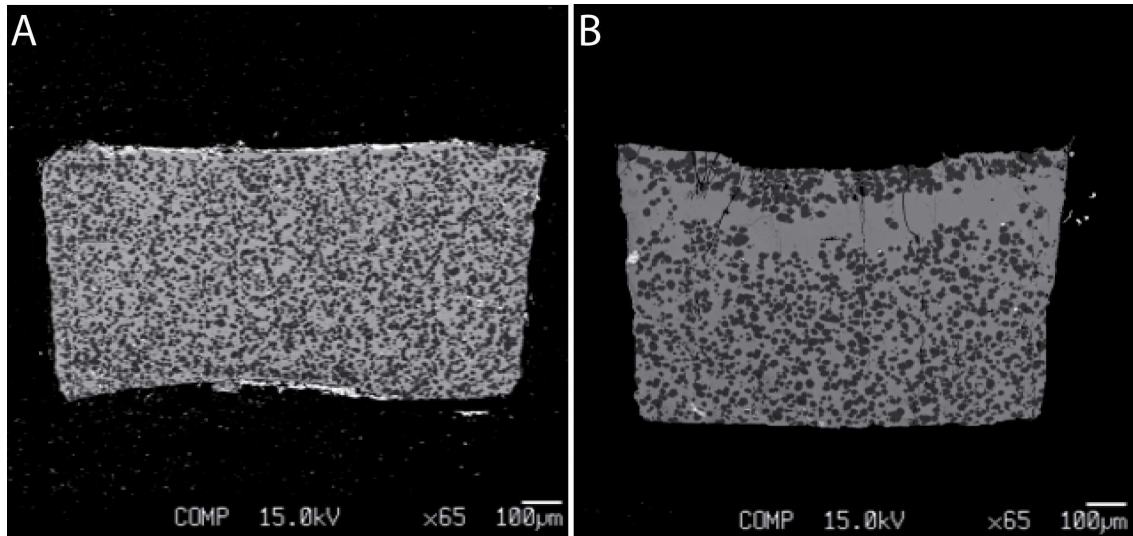


Figure III. 1: BSE-images of static runs without centrifuging. a: experiment OB-14 (1g, 24h), b: experiment OB-6 (1g, 72h). The dark grey phase is olivine, the light grey phase basaltic melt. The black surrounding is the graphite capsule. The starting material is homogeneous mixture of 70 vol% MORB-glass and 30 vol% olivine with grain size of 1.8 μm . Both experiments contain 65 vol% melt, the texture of the 24h experiment corresponds to the starting point of the centrifuge experiments. Note the uneven, most likely temperature gradient dependent distribution of crystals in the longer run.

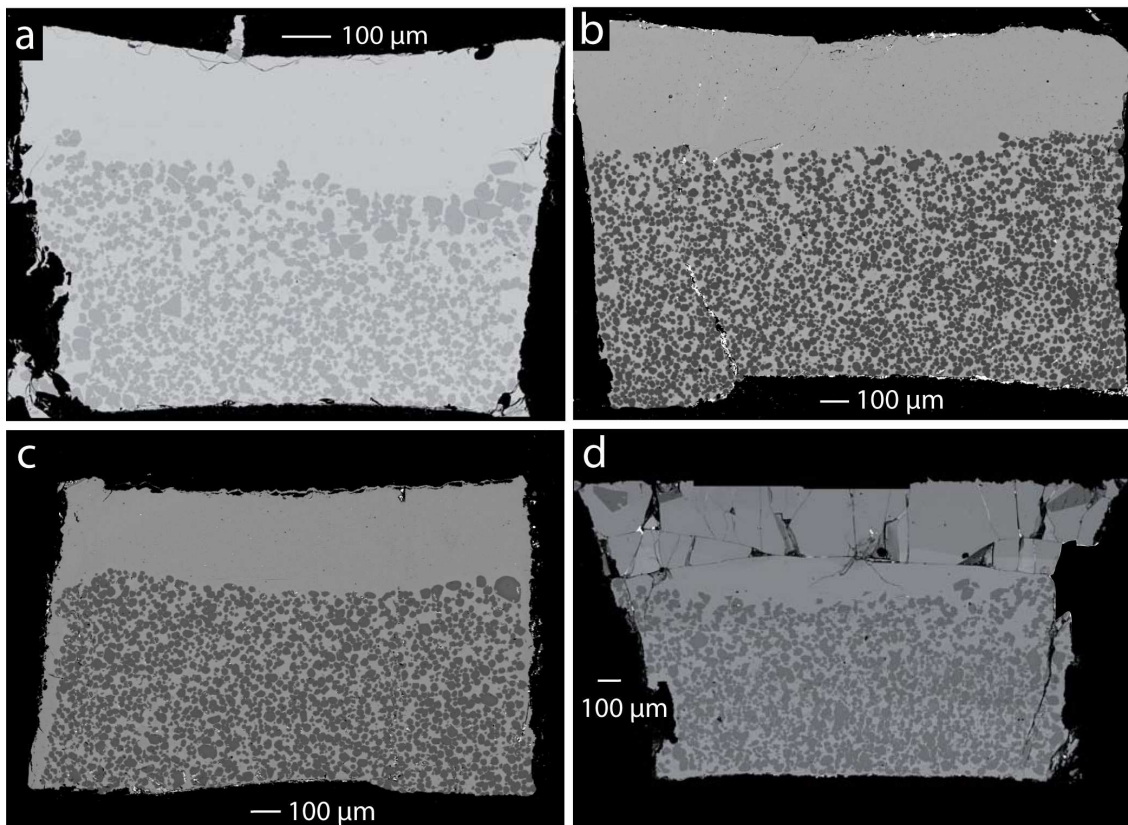


Figure III.2: BSE-images of three centrifuged samples. a. ZOB6 (200g, 3h) with a grain size of 13 μm and a basal layer porosity of 52%. The uppermost crystals are not fully settled yet. b. ZOB6 (200g, 6h) with a grain size of 13 μm and a basal layer porosity of 51%. c. ZOB4 ((400g, 50h), the most compacted experiment with a grain size of 18 μm and a basal layer porosity of 30% and d.FF05 (700g, 10h) with a grain size of 46 μm and a basal layer porosity of 37%. As for the Figure III.1, olivine is in dark grey, basaltic melt in light grey and graphite capsule is in black.

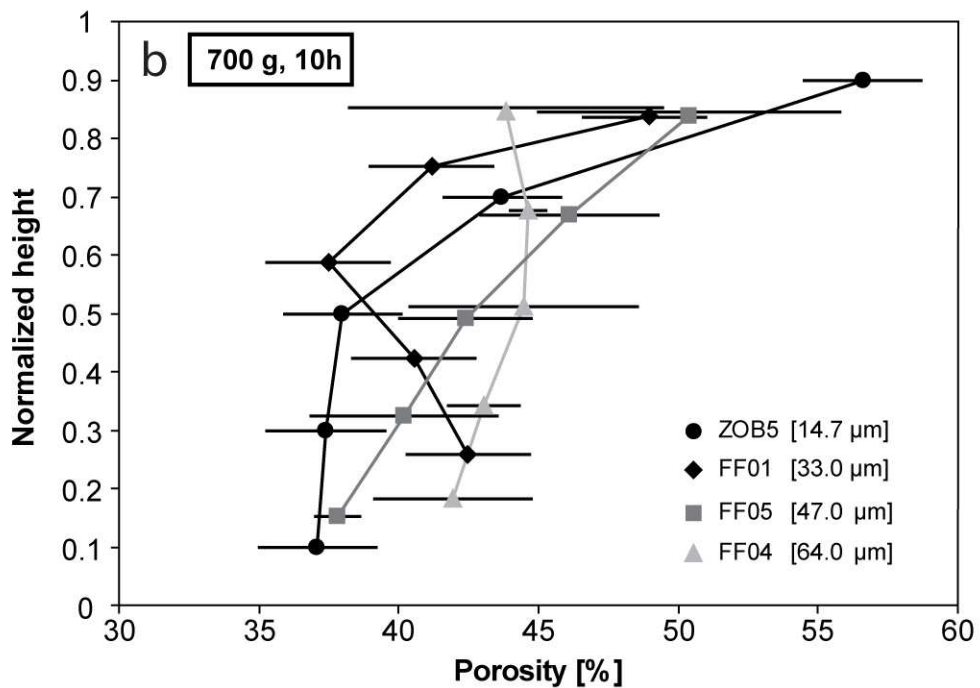
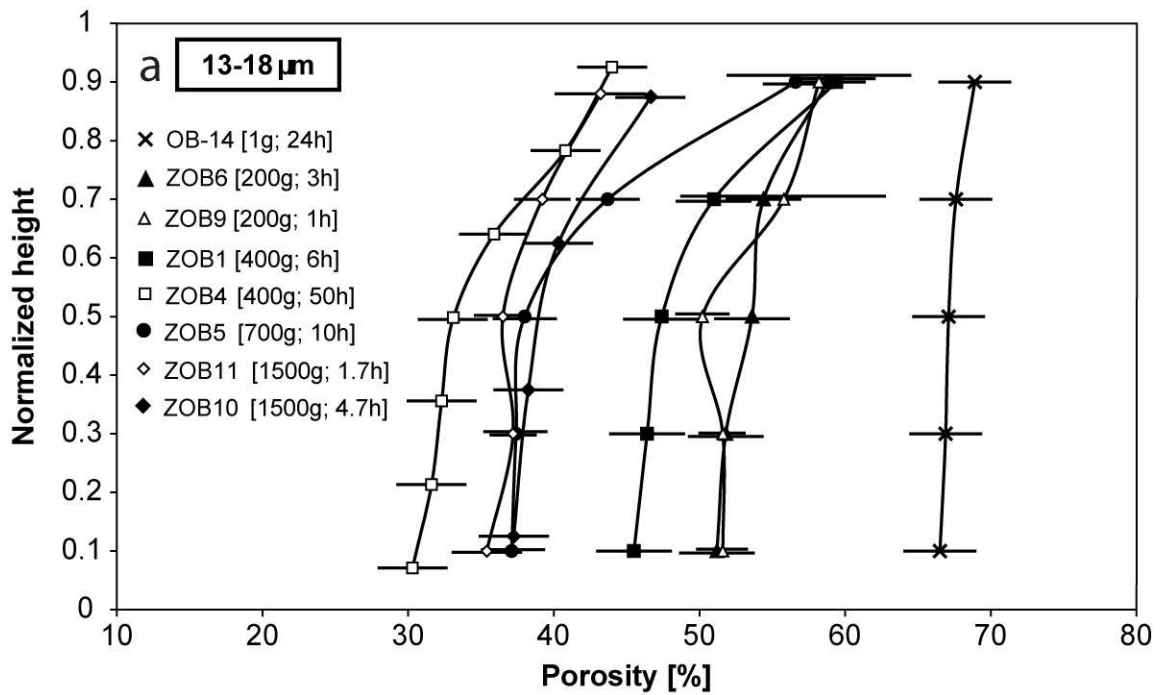


Figure III.3: Porosity profiles with melt abundance or porosity plotted against the normalized total height of the crystal layers of the experiments. a. The experiments with grain sizes 13-18 μm . Triangles represent experiments carried out at 200g; squares, those at 400g; circles, those at 700 g and diamonds, those at 1500 g. The run plotted with crosses is the static experiment of 24h and represents the starting crystal distribution before centrifuging. B. Experiments centrifuged at 700 g for 10h with a different starting grain sizes.

distribution across the cumulate layer can be made: (i) With increasing $\Delta\rho^{(\text{olivine-basalt})} \cdot h \cdot a \cdot t$, the average porosity and the porosity in any segment of the cumulate layer decreases (Table III.2). In fact, the average crystal content is 34 vol% at static conditions, increases to 45 vol% after 3 h at 200 g (Figure III.2B) and to 63 vol% after 50 h at 400 g (Figure III.2C, Table III.2). In the same way, the crystal content in the basal segment increases with centrifugation to 49 vol% (200 g for 3 h) and further to max. 70 vol% (400 g for 50 h, Figure 2c). (ii) Within each experiment, the crystal content of the crystal layer increases downwards, with $d\phi/dz$ being small and almost constant in the lower 2/3 of the cumulate layer of each experiment (Figure III.3A). (iii) With increasing acceleration, an increasing number of crystal contacts can be found in a polished section, and in particular the distance over which two crystals touch increases with $\Delta\rho^{(\text{olivine-basalt})} \cdot h \cdot a \cdot t$ (Figure III.4). This last observation indicates that pressure dissolution of olivine is the dominant mechanism of compaction, leading to larger crystal contact areas per unit volume. In our study, the role of grain rotation during initial compaction, just after grains make contact to each other, cannot be separated from that of chemical compaction, it may contribute a few percent to the decrease in porosity.

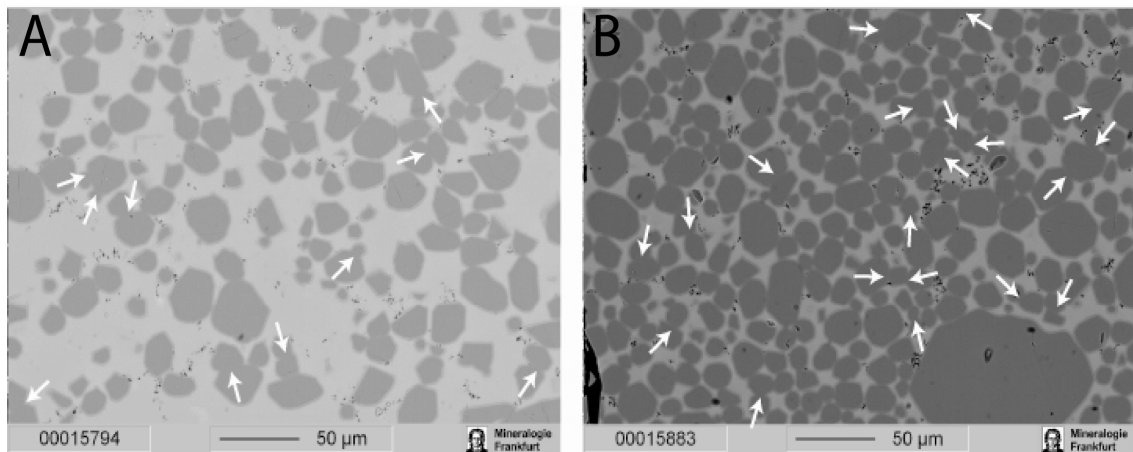


Figure III. 4: BSE images illustrating the abundance of crystal contacts. The BSE images are situated between the middle and the bottom of their respective experiments. a. Picture of the experiment ZOB9 centrifugation time of 1h at 200 g. b. Picture of the experiment ZOB11 with a centrifuging time of 1h40 at 1500 g. The white arrows show the contacts where the chemical compaction is noticeable, demonstrating a clear increase of crystal contacts with effective stress integrated over time.

The increase of crystal content with “applied pressure x time” (Figure III.5) can be calculated with the logarithmic equation:

$$\phi_m / \phi_0 = -0.2751 \log (\Delta\rho \cdot h \cdot a \cdot t) + 2.82 \quad (\text{Eq. III.1})$$

where ϕ_m is the melt fraction in the bottom layer, ϕ_0 the melt fraction after crystal settling (of 0.516 ± 0.017) and which fit quality is $r^2 = 0.88$. Similar porosity gradient $d\phi_m/dz$, as obtained from fitting all crystal layer except the uppermost one in each sample by linear regression, correlates best with $\log(\Delta\rho \cdot h \cdot a \cdot t)$ (Figure III.6) The experimental protocol leads to a narrow range of average grain sizes within 11.0 – 18.6 μm (Table III.2) with an average of 14.1 μm . Thus, we have not included grain size as a variable and equation (III.1) is valid for this average grain size. In order to elucidate the role of grain size, three additional experiments with larger starting grain sizes of 26, 36, and 51.5 μm have been carried out at constant centrifuging time (10 h, gravity acceleration (700 g) and height of the crystal layer (730-740 μm , Table III.2). These experiments resulted in mean grain sizes of 33, 47 (Figure III.2D), and 64 μm , however with very broad grain size distribution. Figure III.3B shows the influence of olivine grain size on the porosity profiles in the crystal layer. Scaling the time of accumulate formation for grain size by multiplying equation (III.1) solved for t with $(d/d_0)^n$, d_0 being 14.1 μm , we calculate the resulting porosity for the grain size scaling exponents $n=1, 2$ and 3 . As can be seen from Figure III.7, the porosities of the basal crystal layer employing larger grain size are only slightly less than for 14.1 μm , and would be only consistent with a grain size scaling exponent $n=1$. Such an inverse linear dependency is expected for densification by power law creep (Wilkinson and Ashby, 1975) or by reaction-controlled pressure solution creep (Shimizu, 1995), the latter being the likely compaction mechanism in this study. Nevertheless, the broad grain size distribution and the untypical porosity profiles for the 33 and 64 μm experiments result in large errors and a large data scatter. We thus consider this result simply as support for a grain size scaling exponent near 1, but further experimentation would be needed to truly constraint this parameter. The observation of a much stronger porosity gradient in the uppermost third of the crystal layer than in the lower two thirds is most likely a combined result of boundary effects and effect of the melt escaping from compacting cumulate layer (Jaupart and Tait, 1995). The total height of the experimental cumulate layers varies between 420 and 640 μm , sectioned into 4-6 layers, each around 100 μm in thickness. Each layer has thus an average thickness of 8 – 9 grains, and the uppermost layer is strongly influenced by e.g. the roughness of the cumulate layer surface. Nevertheless, such a strong gradient at the top boundary was observed in theoretical models of viscous compaction with an upper impermeable boundary (Yang, 2001).

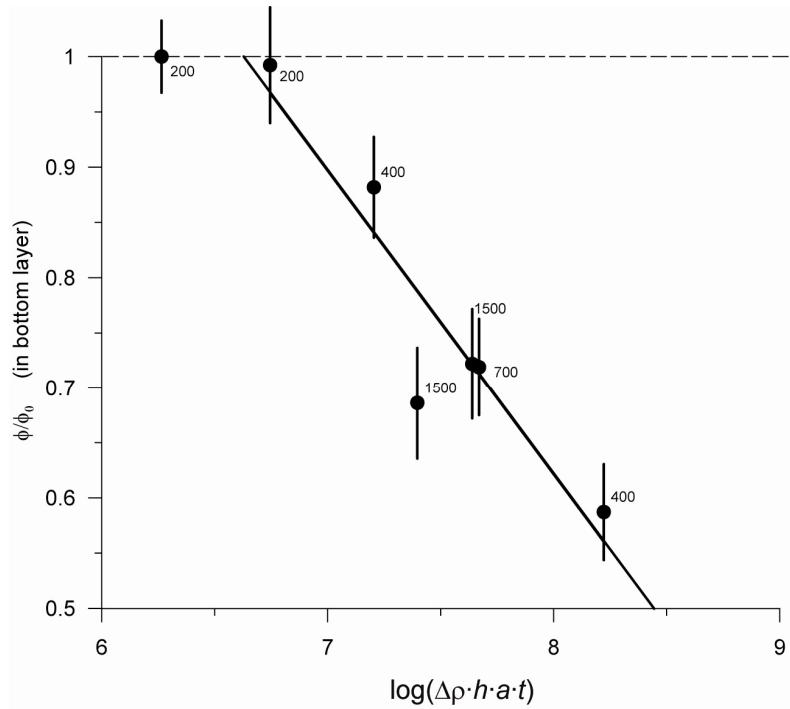


Figure III. 5: Porosity of the bottom layer plotted as a function of applied pressure by time. The solid line corresponds to the straight line best fitting of the experimental data: $\phi_m / \phi_0 = -0.275 \log(\Delta \rho \cdot h \cdot a \cdot t) + 2.82$, with a correlation coefficient of $R^2=0.875$. The dashed line represents to the porosity obtained through crystal settling and corresponds to the starting porosity for chemical compaction in the experiments.

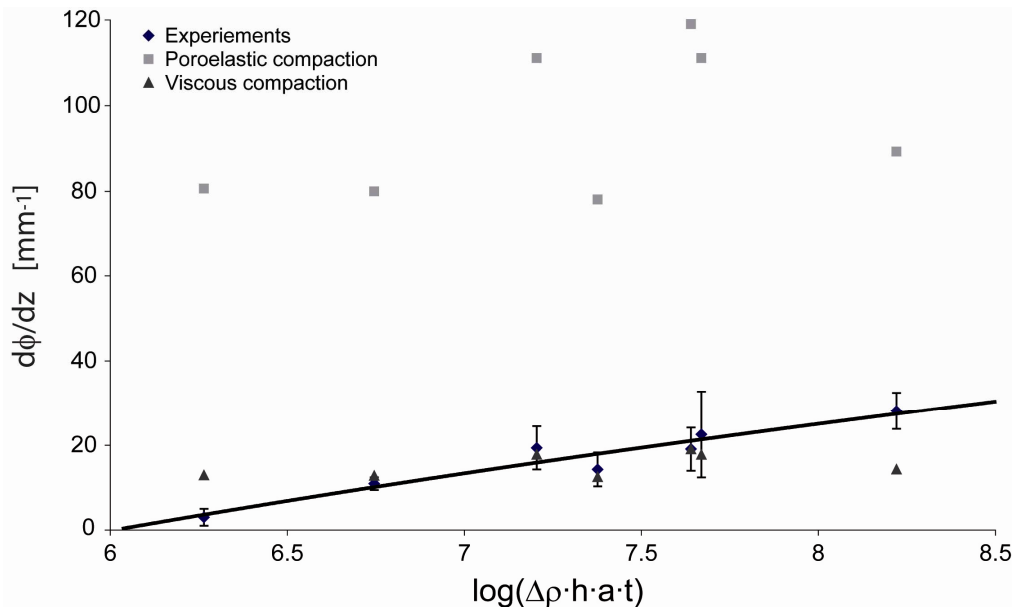


Figure III. 6: Vertical porosity gradient for the experiments with a grain sizes of 13 – 18 μm plotted as effective stress integrated over time. A. In each experiment, all except the uppermost crystal layer (see Figure III.3) were fit by a straight line, the slope yielding the porosity gradient. The solid line corresponds to the best fit straight line with experimental data: $d_{\phi_m} / dz = 0.122 \log(\Delta \rho \cdot h \cdot a \cdot t) - 0.742$ with a correlation coefficient of $R^2=0.915$. Viscous compaction (triangles) and porous compaction (squares) profiles calculated from Yang (2001) are also plotted. The centrifuge experiments correspond to viscous compaction mechanism.

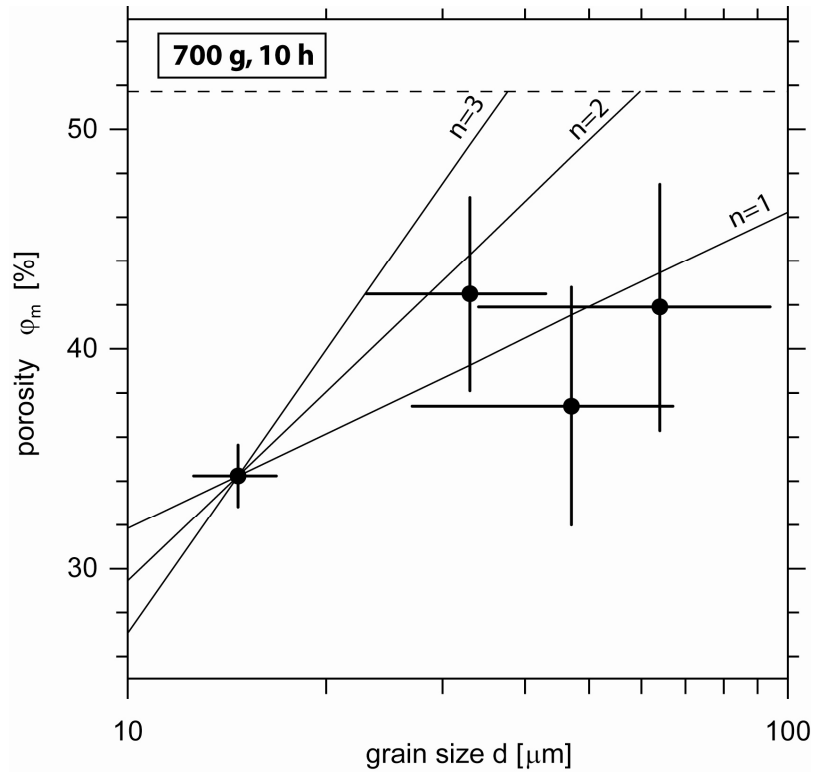


Figure III.7: Porosity in the basal layer as function of grain size for experiments centrifuged at 700 g for 10 h. Experiment ZOB5 with an average grain size of 15 μm yielded a porosity of 37% in the basal layer at a crystal layer height of 450 μm . To render the four experiments comparable, the porosity of ZOB5 was recalculated for a 700 μm crystal layer employing equation (1) to 34.2%. A 700 μm crystal layer is present in the experiments with larger grain size. The lines are the back-calculated porosities for scaling with the grain size exponents $n = 1, 2,$ and 3 . The experiments with larger grain size would only be coherent with a linear grain size dependence of compaction. The dashed line corresponds to the ϕ_0 of 51.8 %.

III.3.3 - Grain growth

With a starting grain size of 1.8 μm , an average grain size of $13.1 \pm 2.5 \mu\text{m}$ is reached after 24 h of static annealing. During centrifugation, further grain growth occurs, and grain size vs. total run time is plotted in Figure III.8. The largest final grain sizes for the experiments starting from 1.8 μm amount to $19.1 \pm 2.4 \mu\text{m}$ after 72 h of static growth, and to $18.6 \pm 2.3 \mu\text{m}$ for grain growth after 21 h static annealing and 50 h centrifugation. The olivine crystals show equant shapes with rounded edges. All but two experiments can be calculated by

$$\log(d) = 0.281 * \log(t) + 0.249 \quad (\text{Eq. III.2})$$

with a fit quality $R^2=0.999$ (Figure III.8) . From this fit, we excluded two experiments: run ZOB10, which was annealed for 10 days to attain a grain size of $\sim 80\mu\text{m}$, yielded one anomalously large grain of 500 μm , which remained stuck to the roof of the capsule

during centrifugation, and a relatively homogeneous population with an average grain size of 12.3 μm , which clearly plots below the best fit line. Run ZOB11 yielded a fairly heterogeneous grain population ($11.0 \pm 6.6 \mu\text{m}$) and would fit equation (III.2) within error.

The slope of 0.281(22) for our grain growth equation (III.2) would yield a growth exponent of 3.6, corresponding closely to the growth exponent $n=3$ predicted for Ostwald ripening controlled either by diffusion in a liquid between large and small grains or by the rate of growth or dissolution at solid-liquid interfaces (Wagner, 1961). Similar results have been found by Cabane et al. (2005) for experiments with olivine crystals in silicate melts at 1250°C, 1 atm, from which they have established a kinetic law $\sim t^{1/3}$.

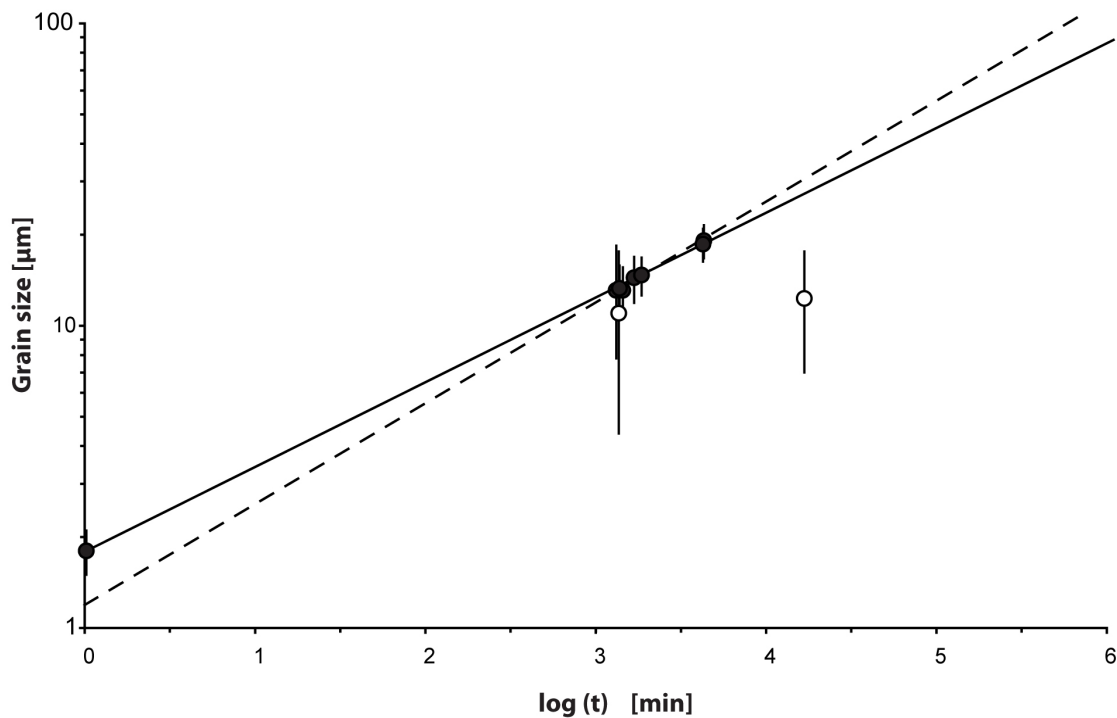


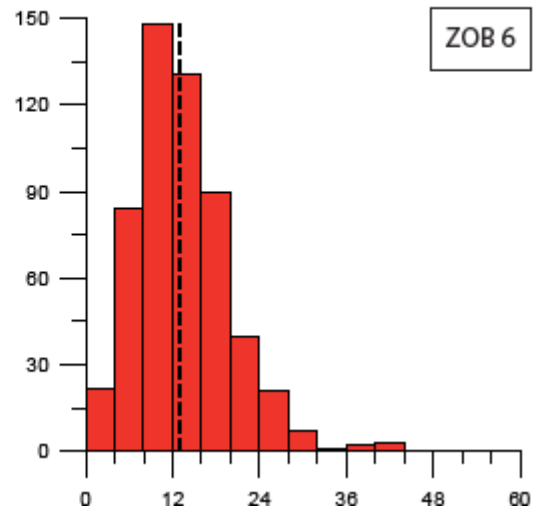
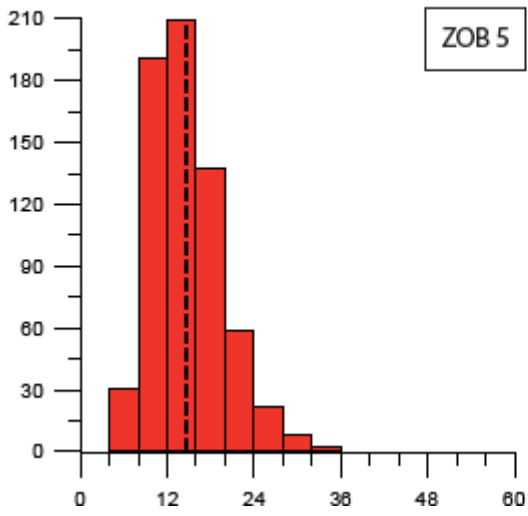
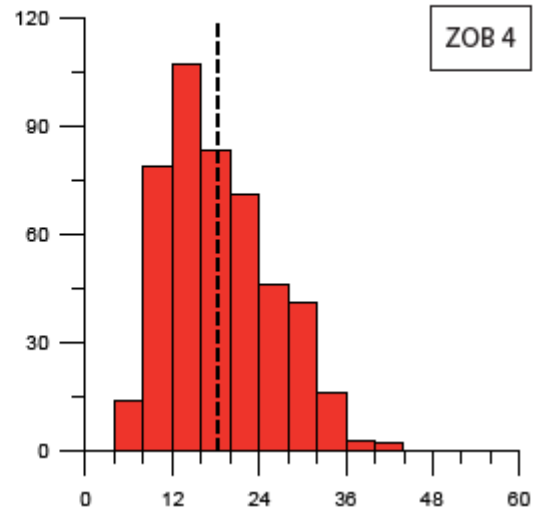
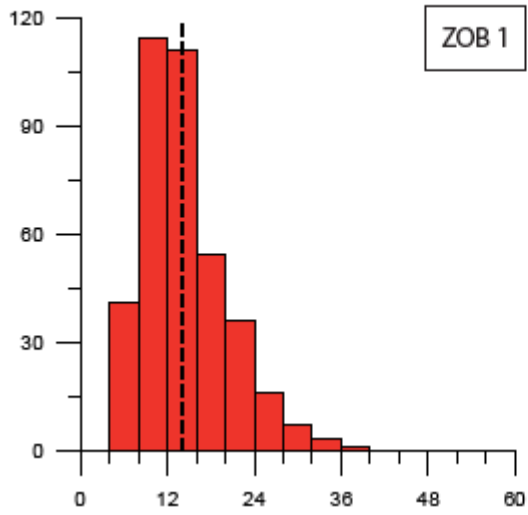
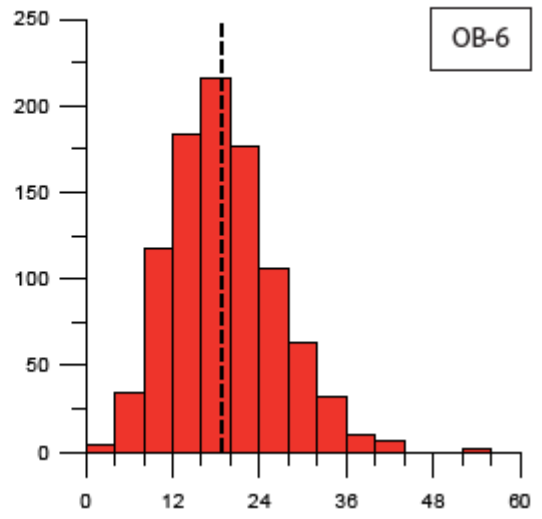
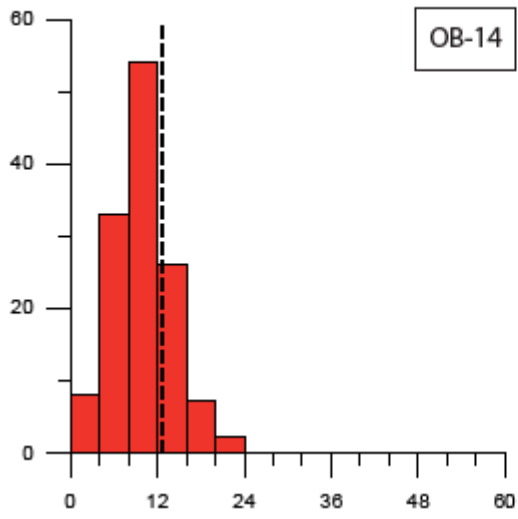
Figure III. 8: Mean grain size of olivine plotted as a function of total run time of experiments starting from 1.8 μm grain size. The solid line correspond to the line best fitting the experimental data: $\log(d) = 0.280 \cdot \log(t) + 0.25$ with a correlation coefficient of $R^2=0.999$. The dashed line corresponds to a grain growth exponent of 3 ($d(\log(d)/\log(t))=1/3$ as found by Cabane et al. (2005)). The open symbols correspond to experiments excluded from the fit (for explanation see text).

Crystal size distributions (CSD) for each experiment are plotted in Figure III.9. The distributions are asymmetric with low abundances towards large grain sizes. For normal grain growth and diffusion-controlled Ostwald ripening, the predicted CSD is narrow, the largest grain size typically smaller than 2x the mean grain size, and the peak

in the grain size distribution is located at or slightly above the mean grain size (Lifshitz and Slyozov 1961; Hillert 1965). Our CSD fit these characteristics quite well. Nevertheless, the largest grain sizes in some experiments are higher than 2x mean grain size, but only for a small percentage of grains (~8.4%).

Normalized crystal size distributions curves for all experiments are plotted in Figure III.10, where grain size is normalized to the mean and the height to the maximum of the grain size distribution. The two experiments with started from 1.8 μm and reached the highest final grain size (OB6 and ZOB4) have exactly the same distribution: narrow with a sharp cut-off the larger sizes. This kind of distribution is typical for diffusion-controlled Ostwald ripening. In contrast, the experiment with the lower final grain size (ZOB11) has a distribution with a long trail to large size. This distribution is predicted in the case of second order surface reaction controlled growth. Unfortunately, run durations, centrifugation and final grain sizes could influence this distribution type, in particular as the experiments OB6 and ZOB4 vs. ZOB11 are end-members of our run series in terms of run conditions. Nevertheless, the "FF" run series (Table III.2), starting from larger grain sizes, also yields narrow CSD fitting best with diffusion-controlled Ostwald ripening.

In summary, our CSD, when compared to theoretical models (Hanitzsch and Kalhweit, 1969; Lifshitz and Slyozov, 1961; Hillert, 1965), indicate that the dominant mechanism of grain growth was diffusion-controlled Ostwald ripening. This result is confirmed by our fitted growth exponent of $n=0.28$ which is similar to $n=1/3$ as determined by Cabane et al. (2005) for diffusion-controlled Ostwald ripening.



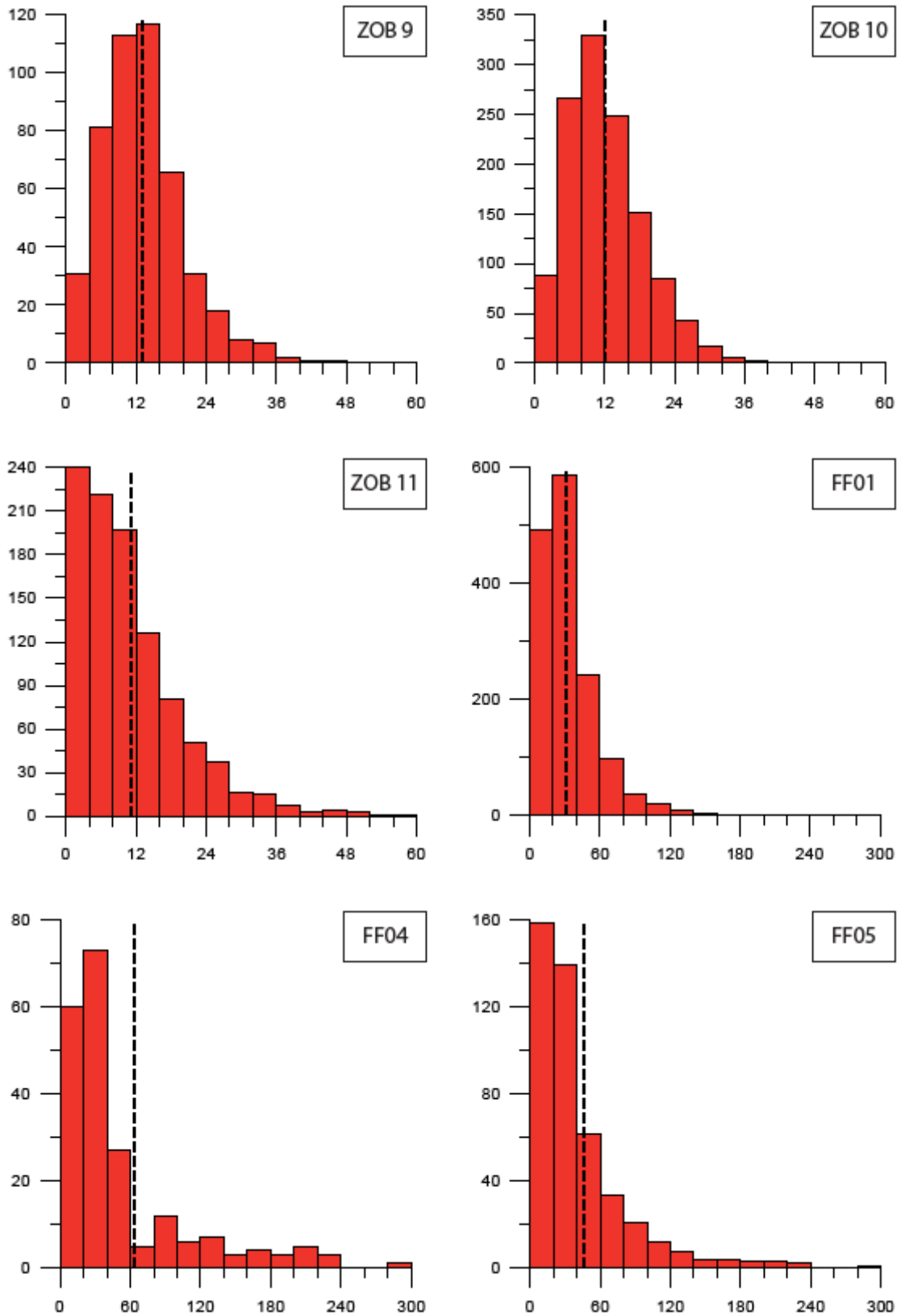


Figure III. 9: Histograms of the grain size distributions in μm . The tendency of the distribution is slightly asymmetric with a small concentration towards high values. The dashed line in each histogram represents the mean grain value.

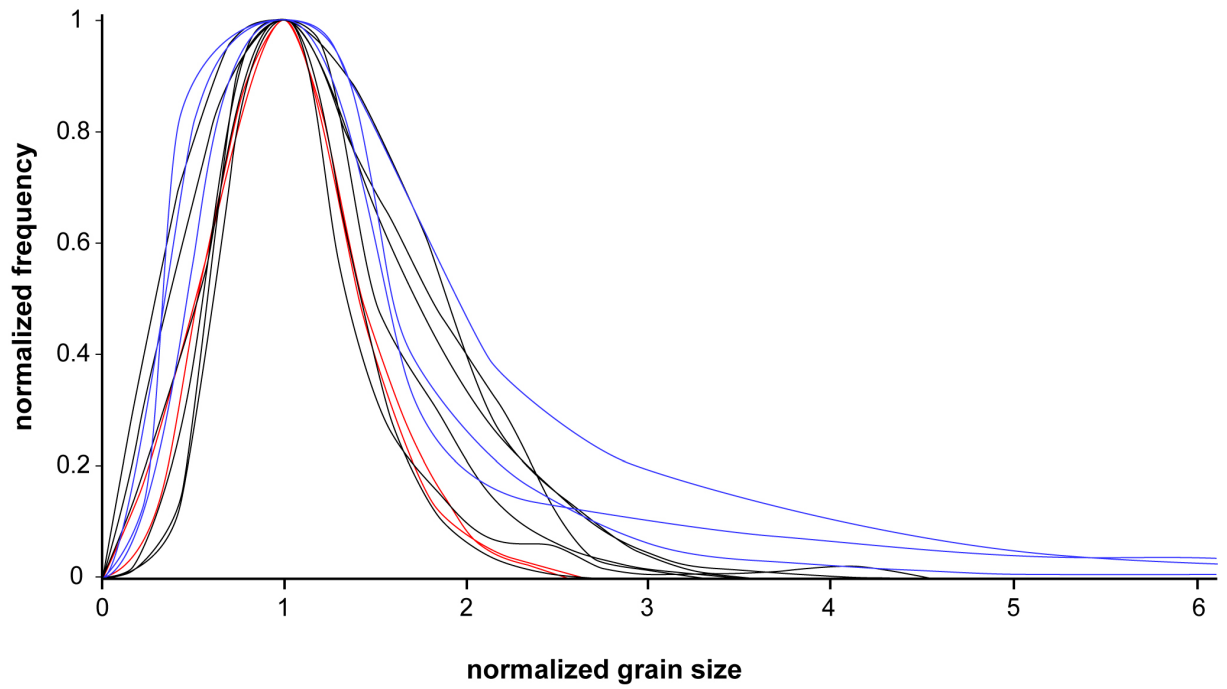


Figure III. 10: Normalized crystal size distribution where the grain size is normalized by the mean grain size and the frequency is normalized to the maximum of each individual sample distribution. In red: the static experiments, in black: centrifuged experiments and in blue: experiment starting from grain size larger than 1.8μm.

Chapter IV

Crystal - melt settling in a magma chamber

Table of content

IV.1 - INTRODUCTION.....	81
IV.2 – CENTRIFUGE EXPERIMENTS.....	81
<i>IV.2.1 – Centrifuge furnace</i>	<i>81</i>
<i>IV.2.2 - Sample preparation</i>	<i>82</i>
<i>IV.2.3 - Analytical methods.....</i>	<i>82</i>
<i>IV.2.4 - Results.....</i>	<i>83</i>
<i>IV.2.4.1 - Cumulate formation</i>	<i>83</i>
<i>IV.2.4.2 - Vertical chemical variation in the melt.</i>	<i>86</i>
<i>IV.2.4.3 - Horizontal chemical variation in the melt.....</i>	<i>89</i>
IV.3 - NUMERICAL SIMULATION	89
<i>IV.3.1 - General description.....</i>	<i>89</i>
<i>IV.3.2 - Mathematical model.....</i>	<i>91</i>
<i>IV.3.3 - Input parameters.....</i>	<i>93</i>
<i>IV.3.3.1 - Density and viscosity of the liquid phase</i>	<i>93</i>
<i>IV.3.3.2 - Minerals</i>	<i>93</i>
<i>IV.3.3.3 - Hindrance exponent: C.....</i>	<i>94</i>

<i>IV.3.4. Results</i>	94
<i>IV.3.4.1 - Comparison of numerical modeling and centrifuge experiments</i>	94
<i>IV.3.4.2 – Evolution of the compaction on the long term</i>	98

IV.1 - Introduction

A series of crystal settling experiments in a system composed of natural two pyroxene-gabbro is conducted in order to understand the relation between cumulus texture and the evolution of chemical composition at grain boundaries during crystal-melt settling in a magma chamber. Numerical simulation was carried out, and then compared with the experimental data in order to model the settling process under centrifugation conditions. The centrifuge experiments and numerical simulation fit quite well. By doing this, we have determined the time required in order to reach the maximum compaction in the experiments.

IV.2 – Centrifuge experiments

IV.2.1 – Centrifuge furnace

In this study, a furnace centrifuge is used in order to simulate the effect of a body force, with much higher acceleration than that due to the normal gravity (g) on partial molten rocks. The general principles of such high-temperature centrifuge furnaces have been already described in the literature (e.g. Roeder and Dixon, 1977; Kadik et al., 1989; Meier and Frishat, 1993). Their use permits an acceleration of the sample of a number (x) of times of the gravity constant (g). This acceleration is very effective to simulate a process of crystal-melt separation at high rates. The driving force for gravitational floating-settling which is proportional to the density contrast between melt and crystals increases by few hundred times. The crystal floating-settling processes have been simulated at high temperatures in the range of mafic rock melting, up 1300°C in a centrifuge furnace by Campbell et al. (1978). The purpose of this work was to study floating process of plagioclase crystals during melting of anorthositic rocks. In the present study, two temperatures (1235°C and 1290°C) have been chosen in order to carry out the experiments in the temperature range of gabbro partial melting. The initial degrees of partial melting here are ca. 27-28 vol% and 55-60 vol% for the experiments carried out at 1235°C and 1290°C, respectively. At this temperature range only a part of plagioclase crystals has been molten. Thus, partially molten gabbro samples represented a mixture of light (plagioclase), heavy crystals (pyroxenes, magnetite, olivine) and coexisting melt.

IV.2.2 - Sample preparation

The starting material is a powder 50-120 μm of natural pyroxene-gabbro from Denezkin Kamen (350 km north of Sverdlovsk, Ural). The composition is presented in Table IV.1. The rock powder was pressed in alumina crucibles having a diameter of 4.5 mm and height of 10 mm. The experiments were performed in a centrifuge furnace ("Centaur-2"; MSE Scientific InstrumentsTM) with a rotation radius of 124 mm. First, five experiments were conducted at a temperature of 1235°C for 6 hours with an acceleration range of 1 g, 100 g, 200 g, 500 g and 1000 g at 1 bar on partially molten gabbro samples. Second, one experiment has been carried out at 1290°C during 2 hours at 1000 g and 1 bar. The grain sizes of the different minerals, in the both experiments types, were: 50 μm for titanomagnetite, 100 μm for type 1 plagioclases and 120 μm for type 2 plagioclase (Bagdassarov et al., 1996 a, b). After the centrifugation, the samples were cut perpendicular to the central axis of the cylinder, and then analyzed by electron microprobe.

Table IV.1. Normalized composition (wt %) of starting materials.

Oxides	Gabbro (wt %)	
	I	II
SiO ₂	44.50	45.69
Fe ₂ O ₃	14.00	10.51
K ₂ O	0.00	0.01
Na ₂ O	0.40	0.41
Al ₂ O ₃	16.40	13.66
MnO	0.15	0.16
CaO	16.60	18.74
MgO	8.60	10.19
TiO ₂	0.62	0.63

I - Initial bulk composition of gabbro rock.

II - Composition of partial melt (1235°C)

IV.2.3 - Analytical methods

The standard electron microprobe analyses with the defocused beam spot have been performed on quenched glass phases. The glass microprobing was performed with an acceleration voltage of 15 kV, beam current of 10 nA, and with a beam size of 10-17 μm . In order to obtain compositional trends in the glass layer, 28 - 32 vertical and 28 horizontal analyses are performed for each sample after centrifuging.

IV.2.4 - Results

The run conditions of all experiments are listed in Table IV.2. In the six experiments, the crystals have been segregated in crucibles according to their buoyancy: plagioclase crystals floated to the top and magnetite crystals sank to the bottom of the capsule. The results of experiments are shown in Figure IV.1. For all samples, glass is the most abundant phase. The chemical compositions of the glass (melt) are listed in Table IV.3.

IV.2.4.1 - Cumulate formation

The set of 5 centrifuge experiments at differing acceleration has been carried out at 1235°C. The experiment S1 at normal gravity 1 g does not show any melt-crystal separation because of the effect of surface tension of melt. During this experiment the gabbro sample has been heated without centrifugation for 6 hours. The other four experiments have been carried out also at 1235°C but at differing accelerations 100, 200, 500 and 1000 g, experiments S2, S3, S4 and S5, respectively. The samples after quenching demonstrated the intensive character of crystal-melt floating-settling with a various degree of separation. The centrifuged samples show a structure consisting of three layers (Figure IV.2A). From the top towards the bottom one distinct (i) a layer of non-melted plagioclase crystals, (ii) a layer of silicate melt, and (iii) a third layer consisted of cumulated crystals in which magnetite and some pyroxene and plagioclase crystals are compacted. In the experiment S6, carried out at 1290°C (Figure IV.1B), the structure consisted of four layers is observed (Figure IV.2B). One can distinguish from the top towards the bottom (i) a glass layer, (ii) a layer of non-melted plagioclases crystals (iii) followed by a second glass layer and, finally, (iv) a cumulate layer formed by accumulation of the magnetite and some pyroxene and plagioclase crystals.

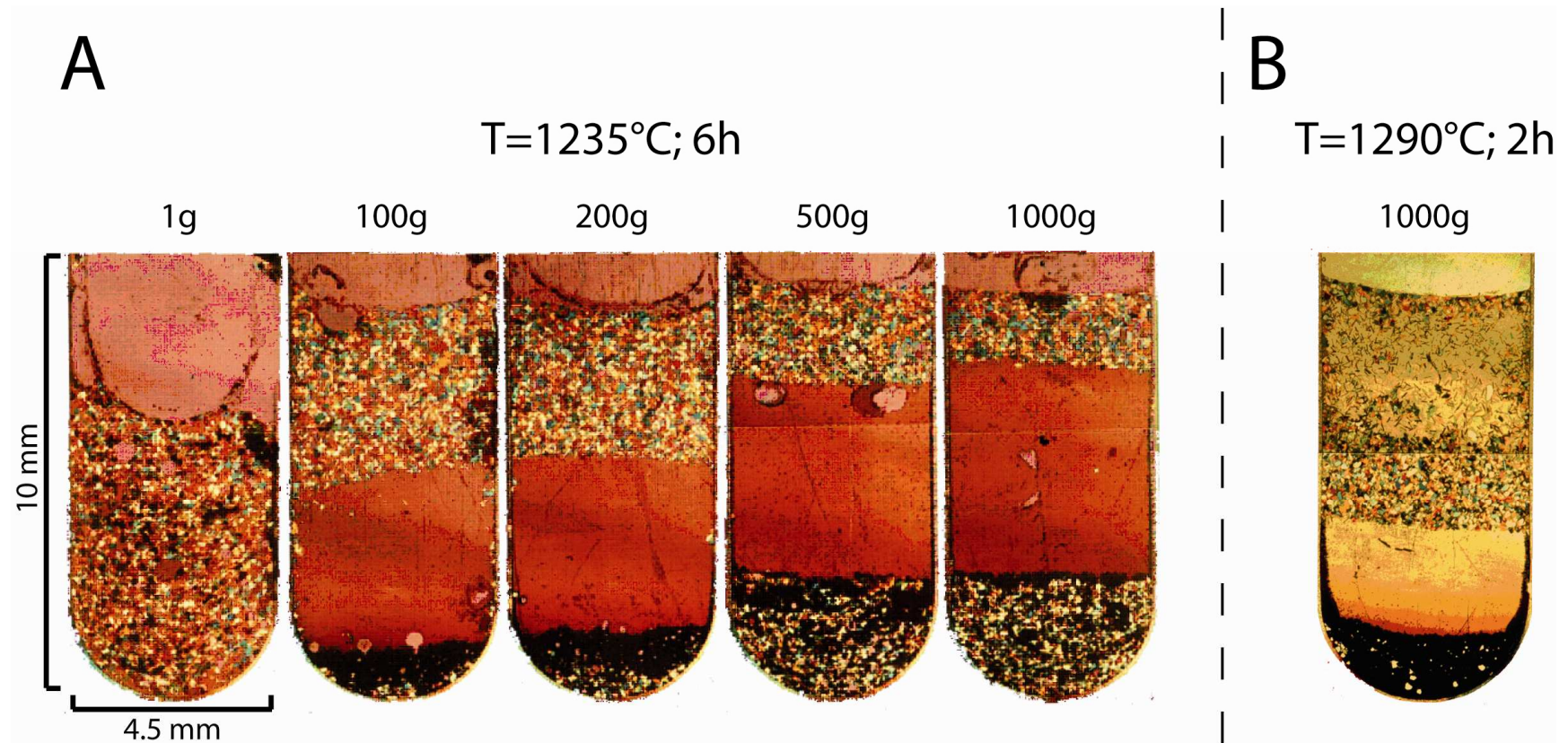


Figure IV. 1: Thin sections of six centrifuge experiments. According to their buoyancy plagioclases are found at the top, titanomagnetites and few pyroxenes are at the bottom of samples. A) The experiments are conducted at 1235°C during 6h for differing accelerations. B) The experiment conducted at 1290°C during 2 hours at 10 00 g.

Table IV.2. Run conditions.

Experiment	T (°C)	acceleration (x 9,81 m/s)	centrifuging time (h)	a * t (m/s)	height melt layer (mm)	melt volume %
S1	1235	1	6	2.16E+04	-	-
S2	1235	100	6	2.16E+06	3.74	47.00
S3	1235	200	6	4.32E+06	3.83	48.13
S4	1235	500	6	1.08E+07	4.3	54.04
S5	1235	1000	6	2.16E+07	4.67	58.68
S6	1290	1000	2	7.20E+06	5.9	74.14

Table IV.3. Representative composition of glass in experiments.

Experiments	T (°C)	SiO ₂ (wt %)	Al ₂ O ₃ (wt %)	FeO (wt %)	MnO (wt %)	MgO (wt %)	CaO (wt %)	TiO ₂ (wt %)	Na ₂ O (wt %)	K ₂ O (wt %)	Total
S1	1235	-	-	-	-	-	-	-	-	-	-
S2	1235	45.92	14.74	9.41	0.16	9.90	18.91	0.55	0.42	0.01	100.00
S3	1235	45.86	13.92	9.85	0.16	10.34	18.87	0.57	0.43	0.01	100.00
S4	1235	45.50	13.00	11.53	0.17	10.09	18.55	0.75	0.39	0.01	100.00
S5	1235	45.50	12.96	11.23	0.17	10.43	18.64	0.67	0.39	0.01	100.00
S6	1290	45.27	9.33	16.01	18.69	8.80	0.70	0.01	0.43	0.15	99.38

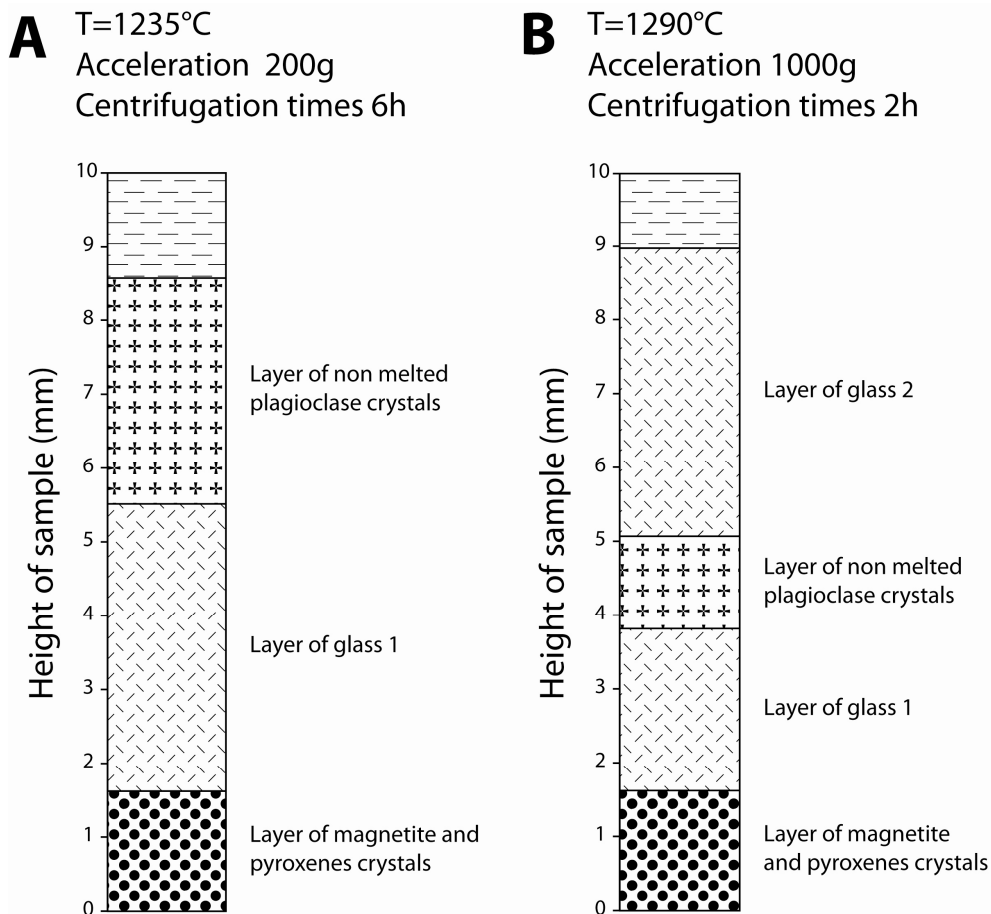


Figure IV. 2: Sections of samples. Several layers are found in the centrifuged samples. A) Experiment conducted at 1235°C at 200 g during 6 hours, B) Experiment conducted at 1290°C at 1000 g during 2 hours.

IV.2.4.2 - Vertical chemical variation in the melt.

The average composition of the glass in all experiments is show in Table IV.3. The microprobe analysis of glass (melt) composition has been performed to 28 – 32 points. The vertical composition trend has been observed for major and trace elements (Si, Fe, Al₂O₃, Mg, Ca and Ti) and is shown in Figure IV.3.

In the experiments carried out at 1235°C, two kinds of behaviour are distinguished in the graph: the curves of compositional variation in experiments at 100 and 200 g are different from those at 500 and 1000 g. In the experiments at 100 and 200g, SiO₂ and Al₂O₃ profiles demonstrate an abrupt increase of concentration from the top of the cumulate layer (0) and become to be constant at height of 1 mm and 2 mm, respectively. FeO and TiO₂ concentration profiles decrease rapidly within the first millimetre of capsule height. Then, FeO concentration profile continues to decrease

slower, whereas the concentration profile of TiO_2 stabilizes. MgO concentration profile reveals an increase followed an abrupt decrease and then becomes stable at the height of 1.5 mm. Finally, CaO profile shows a linear increase with a somewhat chaotic variation at shallow depth of capsule. The distribution of the oxides in the glassy layer of the experiments at 500 and 1000g is quite similar to the described above. SiO_2 and Al_2O_3 concentration profiles demonstrate an almost linear increase between the top of cumulate layer (0) and the base of the plagioclase layer on the top. The profiles of FeO and TiO_2 show a concentration variation decreasing regularly and slightly from bottom to the top. MgO concentration profile shows an increase between 0 and 2mm of capsule height which followed by constant concentration. Finally, CaO concentration profile demonstrates an abrupt decrease between 0 and 3 mm of capsule height, then, it becomes stable in the rest of the glass layer.

The experiment at 1290°C represents a formation of two glassy layers between which a non-melted plagioclase layer is located. On Figure IV.3, this intermediate crystal layer is marked with the red circles, the green circles represent the glass layer 1 which is located between cumulate and an intermediate plagioclase layer, and the glass layer 2 which is sandwiched between two plagioclase layers. The composition of two glass layers is different. The oxide concentration profiles of the first glassy layer have a distribution along the height of the capsule according the distribution of oxides in the glass layer observed in experiments at 1235°C . In the second glass layer, oxide concentrations have the same values as in the plagioclase layer on the top and demonstrate a negligible variation with the height of capsule. Just as in experiments at 100 and 200g at 1235°C , the concentration of SiO_2 , increases abruptly from the top of the cumulate layer (0) and becomes constant above the height 2 mm. The values oxide concentrations in the intermediate plagioclase layer and in the second glass layer are almost constant. Al_2O_3 concentration decreases abruptly in the first 0.5 mm then increases rapidly in the followed 1.5 mm of capsule height. In the intermediate plagioclase layer, the values of Al_2O_3 concentration are scarred then become almost constant in the second glass layer. FeO and TiO_2 concentrations decreases progressively up to the height of the intermediate plagioclase layer, then the curves become stable within the intermediate plagioclase layer and within the second glass layer The MgO concentration profile demonstrates an increase up to 1 mm of capsule height followed rapidly by a decrease in the first glass layer. MgO concentration within the intermediate

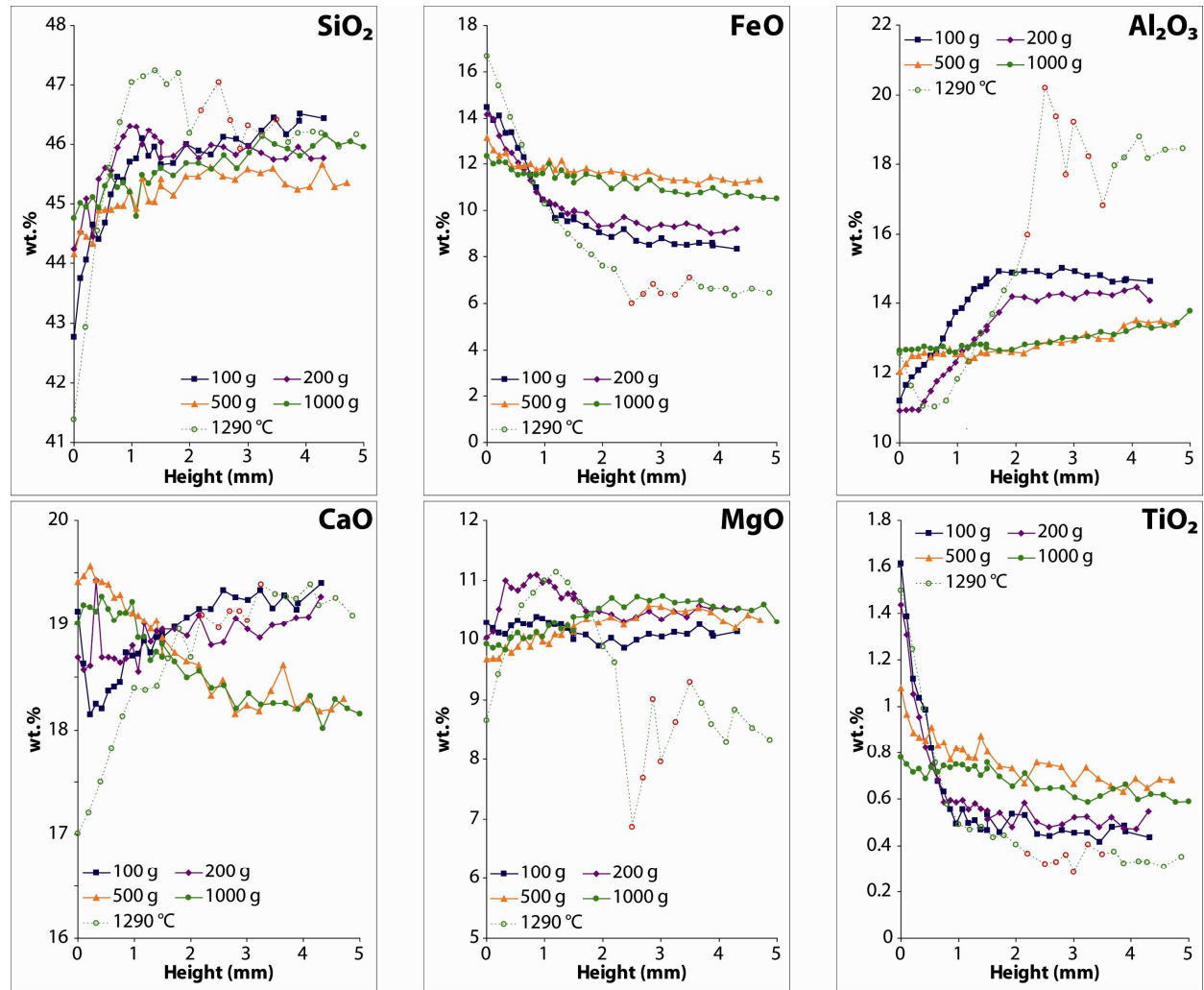


Figure IV. 3: Variation of oxide contents along the height of the glass layer for the experiments carried out at 1235°C and 1290°C. The data points representing the experiments conducted at 1235°C are filled symbols; those representing the experiment at 1290°C are open circles. The red empty circles indicate the layer of non melted plagioclase crystals. The curves could be grouped according to the similar behaviour: (1) experiments at 100 g, 200 g at 1235°C and glass layer 1 of the experiment at 1290°C; (2) experiments at 500 g and 1000 g carried out at 1235°C..

plagioclase layer and within the second glass layer is stable but rather scarred. Finally, CaO concentration profile shows a linear increase up to the height of the intermediate plagioclase layer; reaches more or less stable values within the intermediate plagioclase layer and within the second glass layer.

IV.2.4.3 - Horizontal chemical variation in the melt.

In order to have an overview of oxide distributions in quenched melt, 28 points of analyse are performed along the width of capsule at differing heights. The profiles of the major and trace elements are shown in the Figure IV.4 only for the experiments carried out at 1235°C.

For these experiments, the behaviour of profiles is the same despite few small scale variations, the chemical components in the glassy layer are almost stable. Close to the capsule walls (-3 mm and +3 mm on both sides) there are some marked variations of chemical composition. The horizontal distribution of oxides from the concentration profiles of FeO, Al₂O₃, MgO, CaO and TiO₂ along the width of capsule is relatively stable. Although, Al₂O₃ concentration profile demonstrates a noticeable increase toward the capsule walls for the experiments conducted at 500 and 1000 g. The SiO₂ horizontal distribution of concentration in the experiments is slightly different. The experiment at 100 g shows that SiO₂ concentration slightly increases from one wall to the other. The experiments at 200, 500 and 1000 g show a dome shaped distribution of SiO₂ concentration across the capsule width: the SiO₂ concentration increases toward the center of the capsule, then decreases gain toward the wall. The sole difference between these experiments is that the dome shape is more pronounced for the experiment at 1000 g rather than for the experiments at 100 g and 200 g.

IV.3 - Numerical simulation

IV.3.1 - General description

The numerical modeling presented here is based on a general modeling framework for polydisperse suspension including compression effects and is proposed together with a robust numerical method in Berres et al. (2003). The mathematical analysis carried out there also holds for polydisperse sedimentation with particle-size-specific hindered-settling factors (Basson et al., 2009) as long as all particles have the

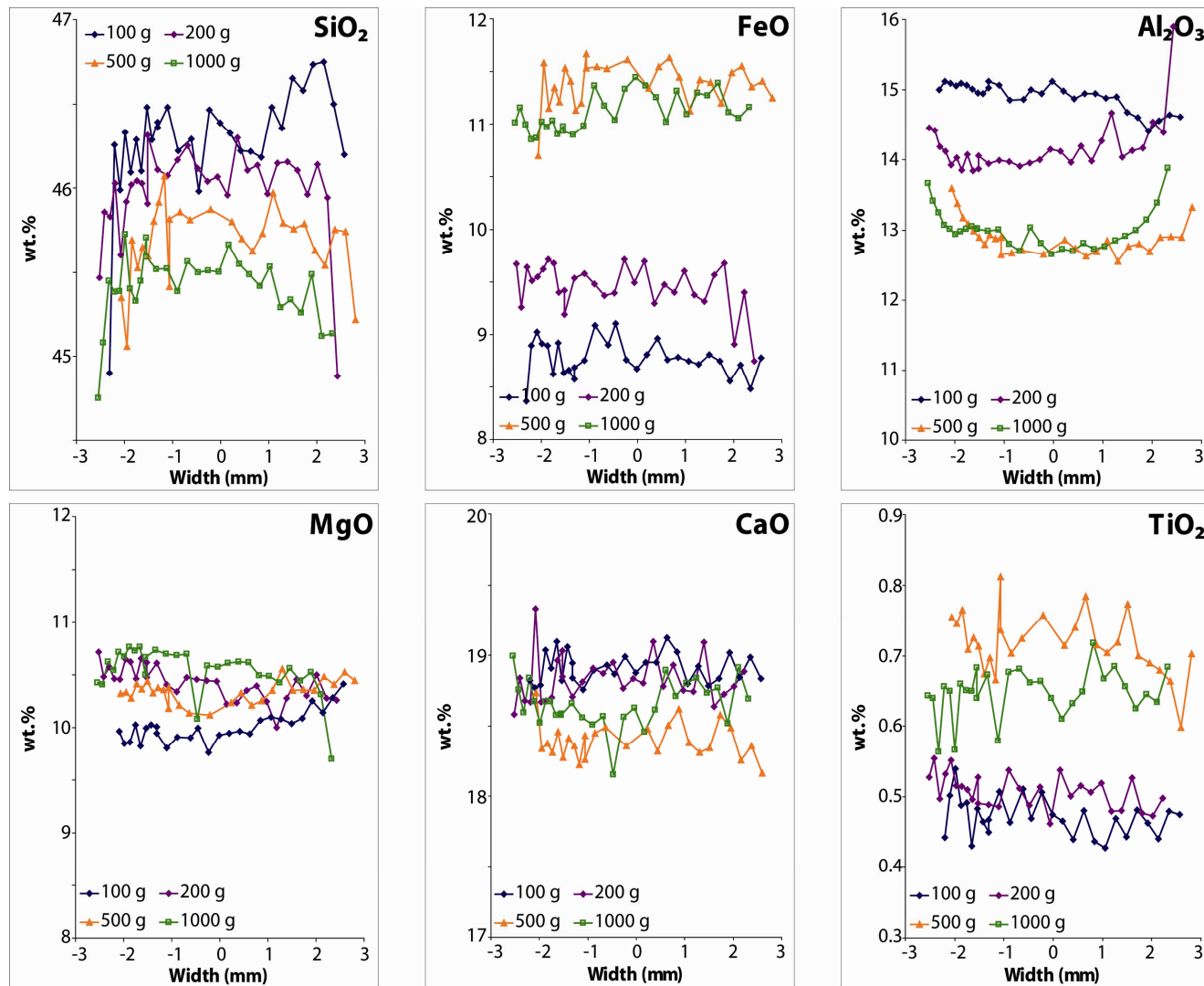


Figure IV. 4: Variations of oxide content across the width of the glass layer for experiments carried out at 1235°C. The curves could be grouped (1) experiments at 100g, 200g (2) experiments at 500g and 1000g carried out at 1235°C .

same density. For the case of particles having different sizes and densities, stability studies have been carried out (Bürger et al., 2002; Berres and Bürger, 2008) and an adaptive high-order finite volume method has been proposed (Bürger and Kozakevicius, 2007; Berres et al., 2009). This modeling framework on polydisperse suspensions can be applied in the context of geology (Bedard et al., 2007; Hladil et al., 2006), petrology and in particular to the study magma chambers (Simura and Ozawa, 2006; Kuritani et al., 2007). For the applicability of polydisperse model in the centrifugation of suspensions see Detloff et al. (2007) and Detloff and Lerche (2008).

IV.3.2 - Mathematical model

Kynch's theory of hindered sedimentation has been already applied to describe the redistribution of floating-settling crystals in magma chambers (Simura and Ozawa, 2006). Here, a brief summary of applied equations is elucidated. The mathematical model describes the evolution of the phase volume fractions:

$$\phi_j = \phi_j(r, t), \quad j = 1, \dots, N,$$

with respect to time t and position r , $0 \leq t \leq T$ and r varies from the inner to the outer radii of the centrifuge as R_1 and R_2 , respectively, i.e., $R_1 \leq r \leq R_2$. The settling of a polydisperse mineral mixture in a rotating furnace centrifuge is modelled by the following spatially one-dimensional partial differential equation (PDE) for the vector-valued local solids concentration (volume fraction) of the j -th mineral species $\phi_j = \phi_j(r, t)$ as a function of radial position r and time t :

$$\frac{\partial \phi_j}{\partial t} + \frac{\partial}{\partial r} \left(-\frac{\omega^2 r}{g} f_j(\phi_1, \dots, \phi_N) \right) = 0, \quad j = 1, \dots, N, \quad (\text{Eq. IV.1})$$

where ω is the angular velocity and g is the acceleration of gravity. It is assumed that the initial condition (at time $t = 0$) is given by $\phi(r, 0) = \phi_0(r) = \phi_0$, which corresponds to an initially homogenous mixture of constant concentration ϕ_0 . At the boundaries of the centrifuge, the system is closed, which gives rise to the zero-flux boundary condition:

$$\frac{\omega^2 r_b}{g} f_j(\phi_1, \dots, \phi_N)(r_b, t) = 0, \quad j = 1, \dots, N,$$

at $r_b = R_2$ and $r_b = R_1$. The components of the vector valued flux function:

$$f_j(\phi_1, \dots, \phi_N) = \phi_j v_j(\phi_1, \dots, \phi_N), \quad j = 1, \dots, N,$$

describe the suspension separation dynamics, where ϕ_j , $v_j(\phi_1, \dots, \phi_N)$ are the volume fractions and the absolute velocity of the j -th mineral phase, respectively. The absolute phase velocity is described in terms of relative phase velocities as:

$$v_j(\phi_1, \dots, \phi_N) = u_j(\phi_1, \dots, \phi_N) - \phi_1 u_1(\phi_1, \dots, \phi_N) - \dots - \phi_N u_N(\phi_1, \dots, \phi_N), \quad j = 1, \dots, N.$$

The basic model assumption, regarding the relative velocity, generalizes the Stokes law as:

$$u_j(\phi_1, \dots, \phi_N) = \frac{d_j^2 (\rho_j - \rho(\phi_1, \dots, \phi_N)) g}{18 \mu_f} V(\phi_1, \dots, \phi_N), \quad j = 1, \dots, N,$$

where d_j and ρ_j are the particle size and the densities of the i -th mineral phase, respectively, g is the acceleration of gravity and μ_f the fluid viscosity. The density difference $\rho_j - \rho(\phi_1, \dots, \phi_N)$ assumes a volume-averaged suspension density:

$$\rho(\phi_1, \dots, \phi_N) = \phi_1 \rho_1 + \dots + \phi_N \rho_N + (1 - \phi) \rho_f$$

as a reference density where ρ_f is the fluid density. The used parametric forms for the hindering function is, following Richardson and Zaki (1954):

$$V(\phi_1, \dots, \phi_N) = (1 - \phi)^C,$$

where $\phi = \phi_1 + \dots + \phi_N$ is the total solids concentration and the Richardson-Zaki hindrance exponent $C=4.7$ was estimated by fitting the numerical modeling results to the centrifuge experimental data (see below). To obtain a numerical method for solving solve the initial-boundary value problem for (IV.1) the space-time domain is discretized by a grid with spatial cells of width $\Delta r = (R_2 - R_1) / M$, where M is an integer, and a time step $\Delta t = T / N$ such that there are points $r_j = R_1 + j \Delta r$, $t_n = n \Delta t$, $m = 0, \dots, M$, $n = 1, \dots, N$, for which the approximation $\phi_{j,m}^n \approx \phi_j(r_m, t_n)$ is computed, starting from $\phi_{j,m}^0 = \phi_j^0$. The marching formula has the form:

$$\frac{\phi_{j,m}^{n+1} - \phi_{j,m}^n}{\Delta t} - \frac{\omega^2}{\Delta r} \left(r_{m+1/2} f_{m+1/2}^n - r_{m-1/2} f_{j,m-1/2}^n \right) = 0, \quad \text{(Eq. IV.2)}$$

where we employ for robustness a central numerical flux $f_{j,m+1/2}^n$. Whereas formula (IV.2) applies for $m=1, \dots, M-1$, for $m=0$ and $m=M$ we employ the following boundary schemes, which result from modifying (2) by discrete versions of the zero-flux boundary conditions:

$$\frac{\phi_0^{n+1} - \phi_0^n}{\Delta t} - \frac{\omega^2}{\Delta r} r_{1/2} f_{j,1/2}^n = 0, \quad \frac{\phi_M^{n+1} - \phi_M^n}{\Delta t} + \frac{\omega^2}{\Delta r} r_{M-1/2} f_{j,M-1/2}^n = 0.$$

IV.3.3 - Input parameters

The calibration of the model is performed in order to obtain a best fit with the centrifuge experiments in a sense of crystal concentration distribution as a function of acceleration. The main variables in the numerical modeling are the viscosity of liquid μ_f , the density contrast between melt and minerals ($\rho_f - \rho_i$), the grain sizes and the hindrance exponent (C).

IV.3.3.1 - Density and viscosity of the liquid phase

In Table IV.1, the chemical analysis in the liquid phase of four samples is given. Using the predictive method of Bottinga et al. (1982), the calculated density of melt is ca. $\rho_f = 2.80 \text{ g.cm}^{-3}$. For the viscosity, the methods of Shaw (1972) and Giordano et al. (2008) have been used to predict the viscosity of the melt which is ca. $\mu_f = 17 \text{ Pa s}$ at 1235°C .

IV.3.3.2 - Minerals

Two minerals in different proportions have been taken in consideration in order to characterise the gabbro: 29.8% plagioclase (type 1: 19.6% with $\rho_1 = 2.65 \text{ g.cm}^{-3}$ and type 2: 10.2% with $\rho_2 = 2.76 \text{ g.cm}^{-3}$) and 10.2% titanomagnetite ($\rho_3 = 5.00 \text{ g.cm}^{-3}$) in 60% silicate melt ($\rho_f = 2.80 \text{ g.cm}^{-3}$ and $\mu_f = 17 \text{ Pa.s}$). In the centrifuge experiments to measure the crystal size distribution of sample was not possible. The crystal populations have been assumed having two sizes for plagioclase and uniform grain size for titanomagnetite crystals. The grain size has been fixed at $100 \mu\text{m}$ for type 1 of plagioclase crystals and $120 \mu\text{m}$ for type 2, respectively. The size of titanomagnetite crystals has been taken $50 \mu\text{m}$.

IV.3.3.3 - Hindrance exponent: C

This exponent called Richardson–Zaki exponent C , is a parameter characterizing a deviation of settling process from a Stokes sedimentation velocity and is defined as follows:

$$V_{\phi} = V_s(1 - \phi)^C \quad (\text{Eq. IV.3})$$

where ϕ is the local concentration of suspension, V_s the settling velocity given by the equation of Stokes (1851):

$$V_s = \frac{g(\rho_c - \rho_f)D^2}{18\mu_f} \quad (\text{Eq. IV.4})$$

and V_{ϕ} is the hindered-settling velocity in suspension, D is the diameter of crystals $\rho_c - \rho_f$ is the density contrast. The hindrance exponent C has been evaluated from the comparison of experimental results of the centrifuge experiments with the distribution of crystals from numerical experiments using the same density contrasts and viscosity. The best fit of the hindrance exponent provides $C \approx 4.7$.

IV.3.4. Results

IV.3.4.1 - Comparison of numerical modeling and centrifuge experiments

Only the centrifuge experiments performed at 1235°C have been used for comparison with the numerical simulation. In fact, only one experiment has been performed at 1290°C, which is too few for validate the numerical modeling at this temperature. The numerical simulations mimic the centrifuge experiments and have been carried out for the same time duration (6 hours) and acceleration. The numerical result of the centrifuge experiment conducted at 500 g is presented in Figure IV.5. The numerical modeling reproduces quite well the structure of the centrifuge experiment. The graph shows clearly a high compaction of crystals at the bottom and at the top of capsule, and a layer of melt in between. In the experiment at 500 g , these three layers correspond to cumulate, top layer of plagioclases and glass layer, respectively.

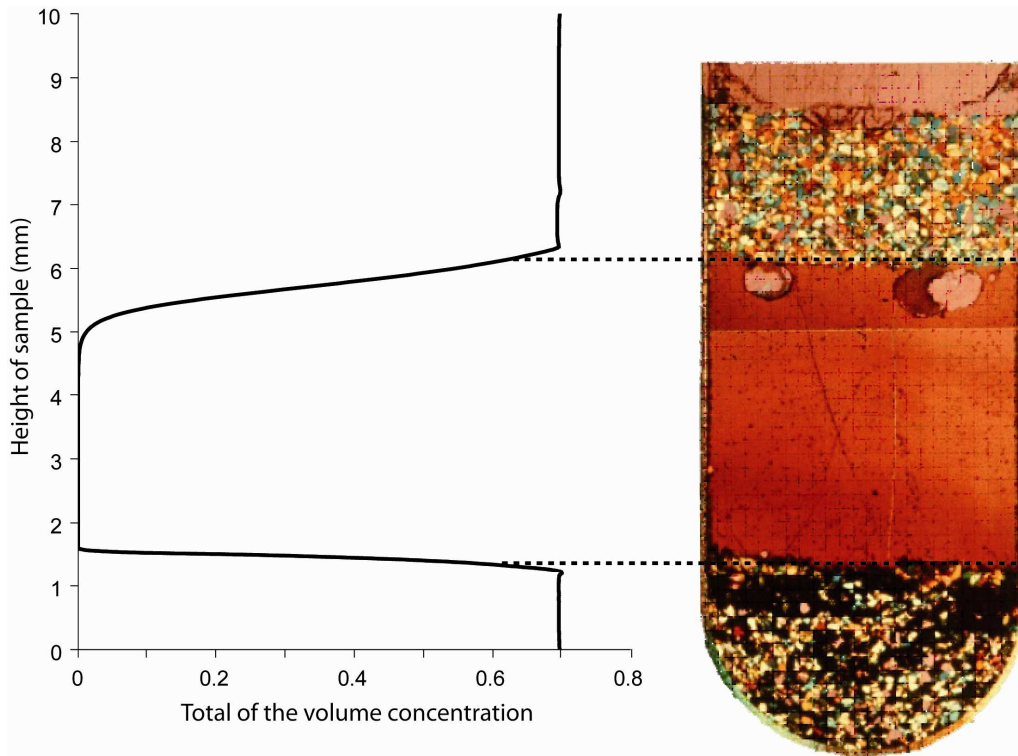


Figure IV.5: Variation of separated melt and crystals along the height of samples predicted by numerical modeling for the centrifuge experiment at 1235°C, 500 g during 6 hours.

Using the same input parameters for the numerical simulation as for the experiments conducted at 100, 200, 500 and 1000 g the vertical distribution of crystals and melt has been reproduced. The results are shown in Figure IV.6. Similar to the case presented in Figure IV.5, two compaction layers are formed: one at the bottom, which corresponds to the cumulate layer and another one at the top which corresponds to the floated plagioclase layer. The gap between these two layers corresponds to the layer of melt which is free of crystals. The height of the melt layer varies with of the applied acceleration. The total amount of melt in the sandwiched layer has been estimated from the centrifuge experiments and compared with numerical simulations. Figure IV.7 shows the observed vs. calculated melt volume. The diagram demonstrates the difference between predicted and observed melt volume in numerical for 3 cases of hindrance exponent $C=4.4$, 4.7 and 5.0. The good correlation of values between observed vs. the predicted melt volume is observed in the case of the hindrance exponent $C=4.7$. At high g the separated melt volume is practically independent from the hindrance exponent C because of the long time of centrifuging. Thus, only centrifuge experiments at 100 and 200 g can be used for choice the hindrance exponent.

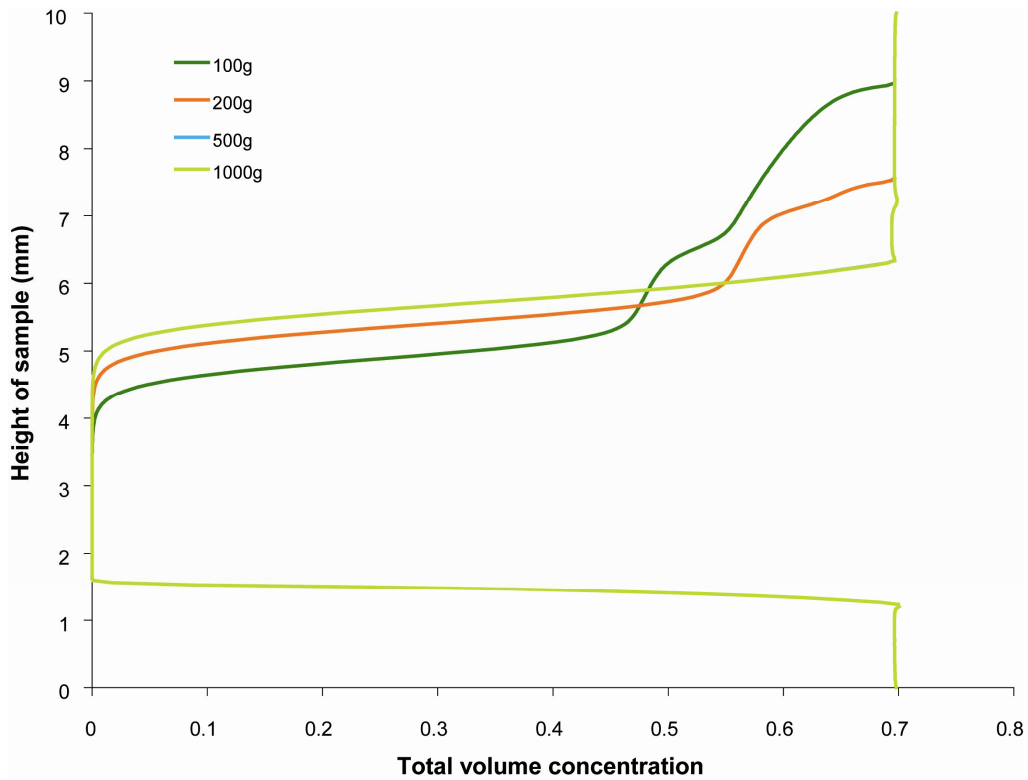


Figure IV.6: Variation of separated melt and crystals along the height of sample predicted by numerical modeling.

Figure IV.8 represents the layered structure of partially molten gabbro sample after the centrifuge experiment at 200 g and for 3 cases of hindrance exponent $C= 4.4$, 4.7 and 5.0. The best fit of the melt layer thickness corresponds to the values of $C=4.7$. The dashed lines represent the boundary between the melt layer and the layer of compacted plagioclase crystal. The position of this boundary has been, used as criteria for the choice of hindrance exponent $C=4.7$

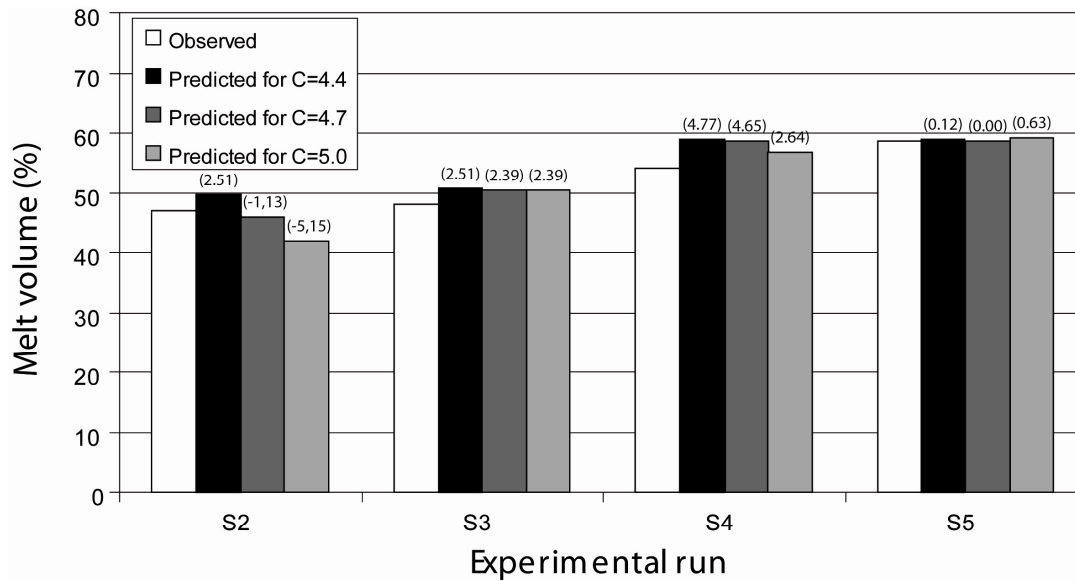


Figure 7: Histogram showing the separated melt volume observed in centrifuge experiments vs. predicted values from numerical simulations for 3 cases of hindrance exponent 4.4, 4.7 and 5.0. The values in brackets correspond to the difference between the observed separated melt volume and the predicted melt volume from numerical modeling (in vol.%).

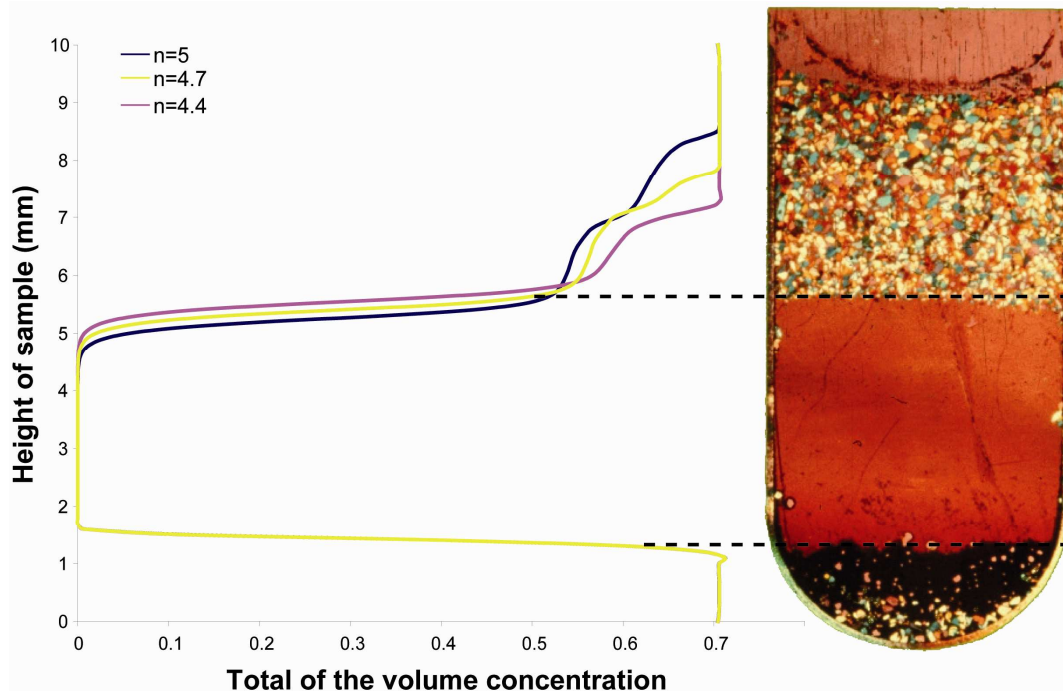


Figure IV.8: Influence of the hindrance exponent C on the simulation results of the centrifuge experiment at 200 g. The dashed lines correspond to location of the glass layer. Above this glass layer, the maximum compaction (0.8) is not reached. This boundary corresponds to the upper boundary of the precipitated crystal layer.

IV.3.4.2 – Evolution of the compaction on the long term

Once the hindrance exponent has been chosen to describe the layered structure of centrifuged samples, the evolution of the compaction in floated and settled crystal layers can be simulated and predicted on the long term by using the numerical model described above at normal gravity. The aim of this modeling is to find the time when a maximum compaction is reached. Figure IV.9 demonstrates that in the case of normal gravity, the maximum compaction in a capsule of 10 mm in height is reached after ca. 3 months. For example, the experiment S4 at 500 g during 6 hours corresponds to 4 months in natural conditions. For the experiment S6 at 1000 g, the time is equivalent to 8 months.

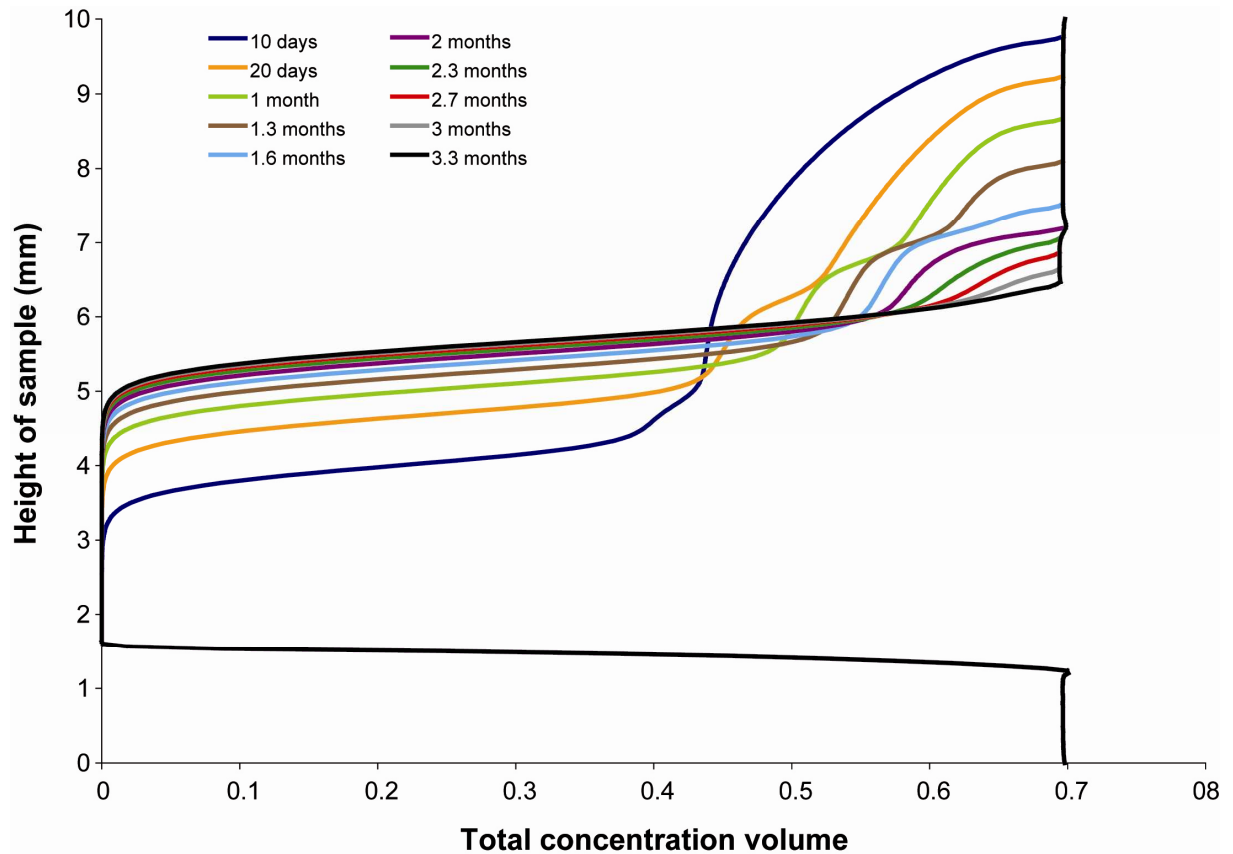


Figure IV. 9: Predictive curves of the separated melt volume along the height of samples at normal gravity.

Chapter V

Discussion

Table of contents

V.1 – MODELING CONSTRAINTS	101
V.2 – EMPLACEMENT OF NESTED DIAPIRS.....	101
V.3 – ORTHO- AND ADCUMULATE TIME FORMATION	104
<i>V.3.1 - Settling velocity in olivine cumulate</i>	<i>104</i>
<i>V.3.2 - Pressure dissolution and precipitation - chemical compaction.....</i>	<i>106</i>
<i>V.3.3 - Formation times of gravitational cumulates in layered intrusions.</i>	<i>109</i>
V.3.3.1 - Orthocumulates	109
V.3.3.2 - Adcumulates	110
V.4 - CRYSTAL SETTLING-FLOATING PROCESS IN A MAGMA CHAMBER.....	112
<i>V.4.1 - Structure of centrifuge samples</i>	<i>113</i>
<i>V.4.2 - Compositional trends of the major and trace elements concentrations in the glass layer 1</i>	<i>114</i>
<i>V.4.3 - Evolution of the compaction.....</i>	<i>115</i>
V.5 - COMPARISON WITH NATURAL EXAMPLES.....	116
<i>V.5.1 - The Great Kavir</i>	<i>116</i>
<i>V.5.2 - The Odenwald Crystalline Complex.....</i>	<i>116</i>
<i>V.5.3 - The Muskox intrusion.....</i>	<i>119</i>

V.1 – Modeling constraints

Analogue modeling is a well-established laboratory technique which can reproduce the overall geometry of geologic structures. These models are designed, imitated with the help of analogue materials, then deformed in a number of ways to simulate deformation and flow of structures found in nature in order to test some tectonic hypotheses.

The principal constraint of these models is the scaling of models. The scaling theory for analogue modeling of geologic processes has first been described by Hubbert (1937) and has later also been discussed by Horsfield (1977), Davy and Cobbold (1991) and Cobbold and Jackson (1992). The scaling theory considers that a physical analogue model is adequate only if the gravitational (F_g) and viscous (F_v) forces acting on the bodies in the model are scaled to the dimensions of the model in the same proportion as these forces acting on the bodies in natural objects. Moreover, these models must be geometrically and kinematically similar or have the same dimensionless numbers (Ramberg, 1981). In tectonic modeling, it is very important that the ratio of these two forces in model and in nature is approximately the same, which is called “a dynamic similarity”:

$$Fg_m / Fv_m = Fg_o / Fv_o \quad (\text{Eq. V. 1})$$

where the subscripts o and m are the original and the model, respectively. In 1986, Weijermars and Schmelling called the ratio F_g/F_v the Ramberg number.

Concretely, in the case of brittle rocks, their cohesion and friction coefficients are the most important parameters, as described by Coulomb’s fracture criterion (Coulomb, 1776). Since cohesion has the dimensions of Pascal (Pa), it should be scaled in a similar fashion as stress (Davy and Cobbold, 1991; Cobbold and Jackson, 1992). Furthermore, the friction coefficient is dimensionless, thus it should have similar values in both model and nature. Finally, for viscous material, viscosity should be scaled as the product of stress and time (Davy and Cobbold, 1991).

V.2 – Emplacement of nested diapirs

With the models described in chapter II, we wanted to test a hypothesis, if a rising diapir ascends straight upwards, or if it might be deviated by a similar buoyant layer located within the overburden strata to follow the diapir stem developing from this

layer (Figure II.1). In all experiments, neither has revealed – and we have observed three couples of yellow and blue diapirs sitting on top of each other – paired yellow and blue diapirs nested into each other. It could be the result of a combination of two effects: on the one hand, the thinning of the upper yellow PDMS layer during the rise of its diapirs, and on the other hand, the deformation then incorporation of the yellow upper PDMS layer into the rim synclines of the blue diapirs due to their ascent. The experiments 2-4 indicate that individual diapirs take their own straight pathways to the surface. That is true for all experiments and independent of the viscosity of the overburden material, whether or not it was Newtonian (experiment 2), or non-Newtonian (experiments 3, 4 and 5). One might expect that the size of the perturbations themselves could control the pathways of the ascending diapirs. However, the cross section of experiment 1, without any perturbations, shows similar structures as experiments 2-4. This implies that the protrusions and their respective size allow only to control the diapir nucleation position and the ascent velocity of the rising diapir. This is evident from the comparison of experiment 1 with the other experiment, where (1) the diapirs grew with only half the velocity as in experiments 3-5 and (2) the positions of the developing diapirs were controlled by the dominant wavelength of the model system, while in the protrusion-dominated systems those perturbations act as nuclei for further diapirs. However, the presence and/or size of perturbations on top of the buoyant layers does not control the vertical pathway of the diapirs. This is most likely because the upper PDMS layer thins out when diapirs grow from it and thus makes its influence negligible on the rise of the lower diapirs. This explanation is reinforced by the experiment 1, without protrusions, which likewise shows this feature, and even in an earlier stage, because the diapirs in this experiment are not as far developed as in experiments 2-4 (compare Figure II.4B and C with Figure II.5, Figure II.6 and Figure II.7B and C). This allows diapir growth from an early, less evolved stage (experiment 1) to a later, more evolved stage (experiments 2-4). From comparison of these four models it becomes obvious that thinning and deformation of the upper, yellow PDMS layer starts already early during the rise of the diapirs from both buoyant layers. That means, in consequence, that nesting of small diapirs growing from offset perturbations (or no perturbations at all) is prohibited simply by the deformation behaviour of the PDMS layers during the run of the experiment. Deformation of the model during diapir rise is characterized by the formation of rim synclines around the ascending diapirs developing from the lower PDMS layer. Those rim synclines incorporate both the overburden

materials and the upper PDMS layer. This is best visible in experiment 1, without imposed perturbations (Figure V.1).



Figure V.1: Part of the experiment 1 without initial perturbations, where a diapir coming from the lower PDMS layer pierces the upper PDMS layer because this last layer is so thin, and so the rising diapir cannot use this weak plane to reach the top of the model.

Thinning and deformation of the upper PDMS layer make it “in attractive” for the growing blue diapirs to follow the yellow PDMS layer, instead of rising straight upwards along their own pathways. As also shown in the experiment 1, the size of the individual protrusions does not play a role in deviating the vertical pathway of the growing diapirs. However, those protrusions (experiments 2-4) influence the growth rate as well as the position of the developing diapirs. By comparing experiments 2-4, particularly experiments 2 and 3, we can study in detail: (a) the effect of differing overburden viscosities on the number and wavelength between diapirs generated, and (b) the effect of differing overburden viscosities on the degree of deformation of the overburden units. These two experiments have overburden viscosities that differ by more than one order of magnitude (experiment 2: $3.4 \cdot 10^4$ Pa s, experiment 3: $4 \cdot 10^5$ Pa s, respectively). Different overburden viscosity leads in experiment 2 to eight fully developed diapirs forming from both source layers, whereas only three diapirs developed in experiment 3. Thus the more viscous the overburden, the fewer the diapirs are formed (Ramberg, 1981).

With regards to the degree of deformation, it is important to note that both overburden layer and upper PDMS layer were completely deformed into rim synclines around the growing diapirs during both of these experiments (2 and 3). However, the

degree of deformation of overburden units reflected their viscosity. In experiment 2, which had the weakest overburden material of all four experiments with perturbations, the overburden units on top of PDMS layers were strongly deformed. The high number of diapirs – which is a function of the low viscosity contrast between buoyant material and its overburden – can be regarded as responsible for the strong deformation of the overburden units in this experiment (Figure II.5). In experiment 3 (Figure II.6), but also in experiments 4 and 5 (Figure II.7 and Figure II.8) where the viscosity contrast is much higher and fewer diapirs develop, the deformation of the overburden units into rim synclines is less pronounced. We conclude, therefore, that the shapes of the rim synclines are a function of the overburden viscosity: the stronger the overburden relative to the PDMS, the less the overburden is deformed.

V.3 – Ortho- and adcumulate time formation

In the experiments of chapter III, two physical processes dominate during the formation of our experimental cumulates: firstly, crystals settle through a purely mechanical process in which the olivine grains behave as rigid bodies and form a framework by mechanical compaction (Yang, 2000). In nature, this process leads to the formation of orthocumulates (Wager et al., 1960). Secondly, once olivines are in contact, compaction occurs through pressure induced dissolution and reprecipitation while melt excesses filtrate upwards through the cumulate pile (chemical compaction, Yang, 2000). In nature, this process leads to the formation of adcumulates (Wager et al., 1960).

V.3.1 - Settling velocity in olivine cumulate

To achieve the settling of solid particles dispersed in a liquid, the particles move because gravity acts on the density contrast between the liquid and the solid particle. This purely mechanical process may continue until all grains are in contact to each other, forming a network. In the uncompacted olivine suspension (with 65.9 vol% melt present), grain contacts are not observed (Figure III.1), but this observation is limited because, even in a perfect olivine grain network, only few grain contacts would be observed in a two dimensional section. A single spherical grain in an infinite layer of

melt settles with a well defined velocity similar to Stokes' settling velocity (V_s – Stokes, 1851), obtained by equating the drag on the settling particle and the buoyancy:

$$V_s = \frac{1}{18} \frac{d^2 \Delta\rho (n \cdot g)}{\mu} \quad \text{(Eq. V.2)}$$

where d is grain size, $\Delta\rho$ the density difference between solid and liquid, $n \cdot g$ the vertical acceleration in the system, expressed as a multiple of the gravitational acceleration g , and μ the liquid viscosity. In our experiments, the average olivine grain size, as measured from BSE images of the sample charges OB14 is $13.1 \pm 2.5 \mu\text{m}$, the density of the olivine is 3.21 g.cm^{-3} , the density of the liquid is computed to 2.79 g.cm^{-3} (employing Lange and Carmichael, 1990), the viscosity of the melt at 1235°C to 17 Pa s (Bottinga and Weill, 1972). With these parameters, the Stokes settling velocity of olivine grains, scaled to 1 g , is $2.31 \cdot 10^{-9} \text{ m.s}^{-1}$. This velocity represents only an approximation because olivine grains are not exactly spherical but short prismatic and thus the drag slightly differently than for a sphere.

When settling crystals are abundant, the concentrated suspension is formed and the settling velocity becomes either slower than that predicted by Stokes' velocity. Moreover, when the concentration of settling crystals is close to the dense packing the settling velocity tends to 0 as a power law. In fact, the distance between grains during the formation of gravitational cumulates is small, i.e. typically less than a few grain diameters and the olivine grains do not settle individually, but in a cooperative way all together as a suspension. In suspension, the velocity of particles is calculated with the “hindered” settling velocity $V(\phi)$, which depends on the concentration of a suspension ϕ and follows the semi-empirical relationship (Tomkins et al., 2005):

$$V(\phi) = V_s \cdot (1 - \phi)^n \quad \text{(Eq. V.3)}$$

where n is the sedimentation exponent. For fine sand particles this empirical relationship works up to the dense packing concentration ϕ_m of 0.74 (tetrahedral or pyramidal packing). With the effectively observed settling velocity $V(\phi) = 4.17 \cdot 10^{-10} \text{ m.s}^{-1}$, and $\phi = 0.341$ (experiment OB14), the sedimentation exponent n in our experiments results to $n \sim 4.1$. The high values of $n \sim 4$ indicate that the average “hindered” sedimentation velocity drops down to zero strongly non-linear, at high concentrations settling slows down considerably but does not vanish. Thus, the mono-dispersed cumulates consisting of crystals deviating from spherical shape experience an

extended stage of slow settling at concentrations close to the dense packing ϕ_m . Schwindinger (1999) investigated the settling of clay prisms in a viscous liquid, because they have a similar shape to olivine grains. She observed that for a solid fraction in the suspension around 0.35 (i.e. 35 vol%), which is very close to that of our samples after static annealing (i.e. 34.1 vol%), the suspension settles as a single object with a speed of $0.1 \cdot V_s$. This would lead to a settling velocity for our suspension of $2.3 \cdot 10^{-10} \text{ m.s}^{-1}$ or $0.8 \text{ }\mu\text{m.h}^{-1}$ at 1 g. In our experiments, the settling velocity in experiment ZOB9 reaches $4.2 \cdot 10^{-10} \text{ m.s}^{-1}$, i.e. 1/6 Stokes velocity. This value supports Schwindinger's (1999) conclusions, and excludes aggregate settling velocities for natural cumulates much lower than 1/6 of Stokes' velocity.

V.3.2 - Pressure dissolution and precipitation - chemical compaction

After grain settling, further densification of the cumulate layer may be reached through grain rotation and chemical compaction. Grain rotation is thought to be of less importance, however cannot be quantified in the present study. Evidence for 'welding' of olivine grains is already found in the centrifuge experiments with the lowest "pressure x time" values (ZOB6), and the porosity of 31.2 vol% of the most compacted experiment (ZOB4) is significantly below that of a most dense cubic packing of spheres with 37 % porosity. For this latter experiment, there is ample evidence for large grain contact areas (Figure III.5), i.e. in a two-dimensional section numerous and long contacts between individual grains can be observed. A detailed analysis of the fine structure of olivine grain boundaries yields further evidence for a dissolution – reprecipitation process of olivine grains. The first feature is the presence of Ca, which is characteristic only for MORB-melt, at the interface of two adjacent Ol-grains even when no melt is present. Analyses have been carried out at the boundary between two adjacent olivine grains as well as towards the interior (Figure V.2A). Table V.1 presents analyses on welded olivine grain boundaries after centrifugation, which should be compared to the analysis of Table III.1. Olivine at the welded grain boundaries has lower SiO₂ and FeO concentrations and increased MgO contents. The presence of Ca in the grain boundary region (Figure V.2B) can be attributed to grain dissolution or recrystallisation. The Ca-concentration is high in the melt phase and at the starting point of the grain junction, but also at an increased level into the interior of the boundary layer between the two olivine grains where no melt is present.

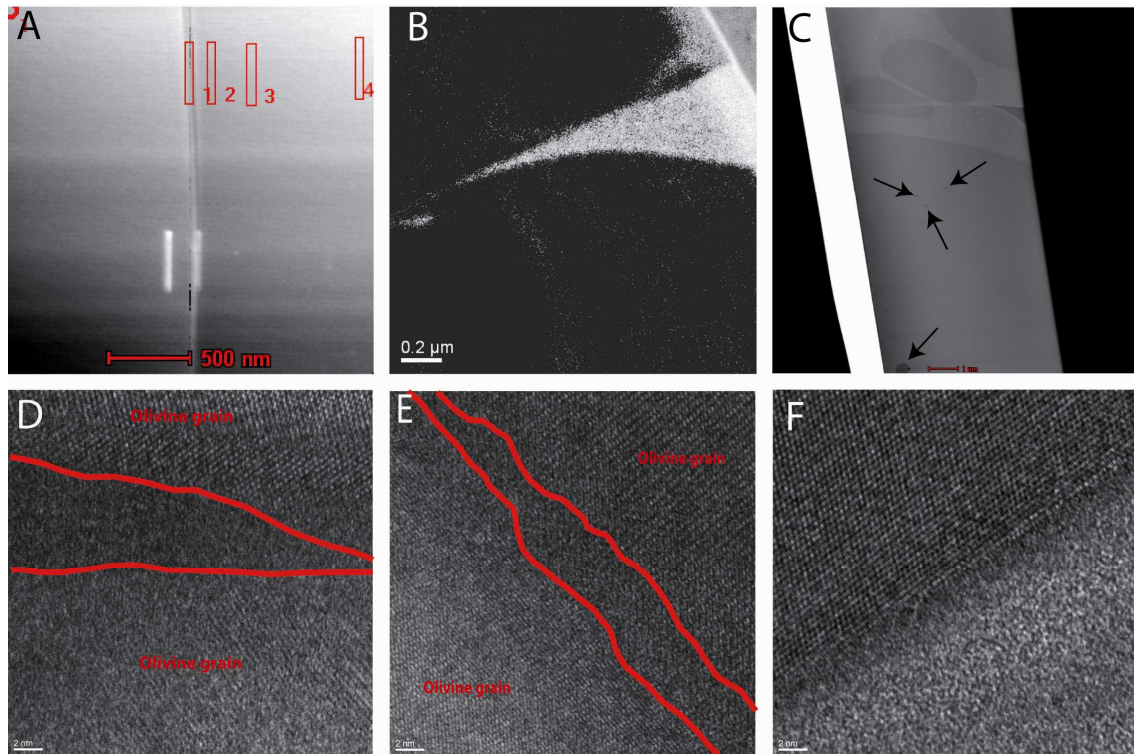


Figure V.2. Fine structures of olivine grain boundaries. a. Contact of two adjacent Olivine grains with analyses positions in ZOB10 sample (see Table V.1). b. Calcium map near triple junction between two grains and a melt pocket. White colour indicates the calcium distribution. c. Overview of one grain boundary in sample ZOB10. The black arrows indicate the inclusions. d and e. HREM Images showing boundary between two olivines in the sample ZOB10 and ZOB11, respectively. f. HREM Image showing a boundary between melt (amorphous phase) and one olivine grain (crystallized phase) in sample ZOB10.

Table V. 1: Chemical composition for the different positions situated between two olivine grains (for the point 1), then towards the centre of one olivine grain (for the points 2, 3 and 4) (see Figure V.2) in experiment ZOB10.

Oxides	1 (wt%)	2 (wt%)	3 (wt%)	4 (wt%)
SiO ₂	35.70	35.40	33.80	37.30
TiO ₂	0.06	0.00	0.00	0.00
FeO	4.60	3.40	4.00	3.70
Al ₂ O ₃	0.30	0.00	0.20	0.00
MgO	58.90	61.00	61.80	58.70
CaO	0.40	0.20	0.20	0.20
Total	99.96	100.00	100.00	99.90

Images obtained with the high resolution electron microscope (HREM) have allowed identifying the fine structure of the boundary between two adjacent olivine grains (Figure V.2D,E) which are compared to an olivine - melt contact (Figure V.2F). The upper left part of Figure V.2f is an olivine crystal (i.e. the crystalline phase) and on the lower right side the melt phase (i.e. the amorphous phase). The thickness of the recrystallized boundary layer is not more than 2 nm. In Figure V.2D and E, the recrystallized boundary layer between two olivine grains is 4-6 nm. The boundaries between two olivine grains are distinct but not as fully crystallized as the interior of olivine grains. This indicates that some chemical species from the MORB melt (e.g. Ca) prevent the re-crystallization of olivine in a fully crystalline structure.

These observations can best be explained by a dissolution and reprecipitation of olivine. This process is driven by the centrifuge induced pressure on grain contacts. This non-hydrostatic pressure is proportional to the height of the olivine column above the measured section, the density contrast between olivine and liquid and the centrifugal acceleration. The non-hydrostatic stress leads to dissolution and a basaltic liquid oversaturated in olivine, which in turn causes reprecipitation on the grain surfaces in contact with the liquid. This process increases the grain contact area to distribute the effective stress over a larger surface (Connolly and Podladchikov, 2000). A complete review of the literature about pressure solution mechanisms and its modeling goes beyond the purposes of this study and can be found in Angevine and Turcotte (1983), Tada and Siever (1989), Shimizu (1995) and Fowler and Yang (1999). This non hydrostatic pressure (P_p) for our olivine grains in the basal segment can be quantified through

$$P_p = (1 - \phi_m) \cdot \Delta\rho^{(\text{olivine-basalt})} \cdot h \cdot a \quad (\text{Eq. V.4})$$

and amounts to 0.6-2.5 kPa in the experiments that resulted in porosities < 40% in the basal layer. This value is similar to the pressure of 1.4 kPa at the base of a cumulate of ½ m height and a porosity of 5 %, i.e. values typical for strongly compacted olivine cumulates in nature.

Chemical compaction will slow down when the decreasing permeability of the adcumulate leads to hindered escape flow of excess melt. Whether this applies to our experiments can be evaluated by comparing the hydrostatic pressure gradient ∇P with the lithostatic pressure gradient $(1 - \phi) \cdot \Delta\rho \cdot g$. With

$$\nabla P = q \cdot \mu / k \quad (\text{Eq. V.5})$$

where q is the melt flux expressed as $h \cdot \Delta\phi / t$ and k permeability calculated from $k = d^2 \cdot \phi_m^3 / (1 - \phi)^2 \cdot c$, where $c=10$ (Connolly et al., 2009). Hydrostatic pressure gradients result to $\nabla P = 0.4-220 \cdot 10^3 \text{ Pa}\cdot\text{m}^{-1}$ and lithostatic pressure gradients are $0.3-4 \cdot 10^6 \text{ Pa}\cdot\text{m}^{-1}$. The hydrostatic over the lithostatic pressure gradient in the experiments then results to $10^{-2} - 10^{-3}$ and thus $\ll 1$, and we conclude that our experiment are not permeability limited.

V.3.3 - Formation times of gravitational cumulates in layered intrusions

Typical natural cumulate layers of olivine are $\leq 1/2$ m in thickness, with typical average grain sizes from 2 to 10 mm (Goode, 1975; Wiebe, 1987). In the following section, we will discuss formation times employing these characteristic values and using the result of the centrifuging settling of crystals.

V.3.3.1 - Orthocumulates

Orthocumulates are thought to be formed through mechanical crystal settling of a concentrated suspension. Small settling distances result in fast growing thickness of orthocumulate layers, which depends on the initial crystal fraction in the unsettled suspension. The settling time can then be calculated as follows:

$$t_{\text{ortho}} = (h \cdot 0.46 / \phi_{\text{ci}} - h) / V(\phi_{\text{ci}}) \quad (\text{Eq. V.6})$$

where h is the thickness of the uncompacted orthocumulate layer, typically twice the thickness of a chemically compacted dense adcumulate layer. In the equation V.6, 0.46 corresponds to the crystal fraction after gravitational settling while ϕ_{ci} denotes the initial crystal fraction in the melt layer from which the orthocumulate is formed. The time necessary to produce 1 m of an uncompacted crystal layer of olivine is thus 242, 39, or 10 hours for an initial crystal content of 1% for grain sizes of 2, 5, and 10 mm, respectively. For an initial crystal fraction of 5%, these values become 52, 8.4, and 2.1 hours and for an initial crystal fraction of 10% settling times are 29, 4.6, and 1.1 hours. Thus, it can be concluded that the hindering of crystal settling due to the formation of a dense suspension does not slow down orthocumulate formation decisively. As it will be shown in the next section, chemical compaction is of few orders of magnitude slower.

V.3.3.2 - Adcumulates

Equation (III.1), derived from the centrifuge experiments, yields the time dependence of chemical compaction for constant grain size (14 μm) and can thus be employed to calculate adcumulate formation times. To scale for grain size, we introduce a linear growth of grain size dependence as an appropriate for a dissolution-precipitation limited process (Boudreau and McBirney, 1997; Shimizu, 1995). The compaction time, i.e. the time necessary to reduce porosity from $\phi_0 = 0.512$ to ϕ_m in the basal layer of cumulate of height h_{cum} can then be calculated as

$$t_{adcum} = \frac{20.8 \cdot d}{10^{\phi_m} \cdot h_{cum} \cdot g \cdot \Delta\rho^{crystal-melt} \cdot d_0} \quad (\text{Eq. V.7})$$

where d_0 is the experimental average grain size of 14.1 μm and ϕ_m the observed melt porosity (in %) at the cumulate's base. Please note that in this equation h_{cum} occurs in the denominator, as pressure dissolution driven chemical compaction in the basal layer is faster, when the crystal pile is thicker, because the effective stress caused by the overlying weight is getting larger. Formation times of adcumulate from orthocumulate layers with a starting porosity of 54% are then calculated for olivine (Figure V. 3). For a $\frac{1}{2}$ meter olivine adcumulate layer the chemical compaction will result in a residual porosity 30 vol% at grain sizes of 2, 5, and 10 mm after 109-546 days, i.e. 0.30-1.5 yrs. To reach 25 or 20% residual porosity, 0.7-3.4 and 1.5-7.7 yrs, respectively, are necessary for these grain sizes.

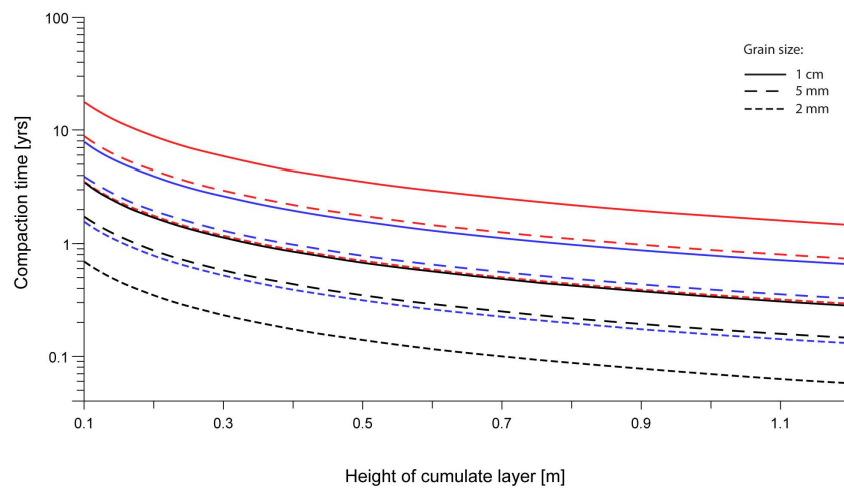


Figure V.3: Cumulate formation time is calculated from the equation (III.1) for different grain sizes (1 cm; 5mm and 2 mm) and with various final porosities. The three lines for each grain size correspond to same value of porosity: the highest is for a porosity of 35 vol%; these of the middle for 30 vol% and the lowest for a porosity of 25 vol%.

These periods of orthocumulate and adcumulate formations may first be compared with characteristic cooling times of magma sills, which are in the order of years to decades, depending on a sill thickness and a depth level of intrusion. The solidification of a dike or a sill is given by Turcotte and Schubert (1982):

$$t_s = \frac{b^2}{4\kappa\lambda^2} \quad \text{(Eq. V.8)}$$

where at $t = t_s$, all magma has solidified and where b is the width of the sill (m), κ is the thermal diffusivity and λ is the roof of:

$$\lambda(1 + \text{erf } \lambda)e^{\lambda^2} = \frac{c_p(T_m - T_0)}{L\pi^{1/2}} \quad \text{(Eq. V.9)}$$

where c_p is the specific heat capacity of country rocks, T_m is melting-point temperature of magma and L is latent heat of solidification. The thermal diffusivity, κ , is defined by:

$$\kappa = \frac{K}{\rho_r c_p} \quad \text{(Eq. V.10)}$$

where K is the thermal conductivity of the material, ρ_r is density of the host rock, and c_p is specific heat capacity.

In the case of mafic layered intrusions it is appropriate to select basaltic material also as a country rock and K , L , ρ_r and c_p are then the material properties of basaltic material and their values are typically $K=2.5 \text{ W m}^{-1} \text{ K}^{-1}$, $L = 420 \text{ kJ kg}^{-1}$, $T_m - T_0 = 1207^\circ\text{C}$, $\rho_r = 2750 \text{ kg m}^{-3}$, $K = 2.5 \text{ W m}^{-1} \text{ }^\circ\text{C}^{-1}$ and $c_p = 1 \text{ kJ kg}^{-1} \text{ }^\circ\text{C}^{-1}$. With these values, the thermal diffusivity κ results $= 9.1 \cdot 10^{-7} \text{ m}^2\text{s}^{-1}$. T_m can be assumed to be at or slightly less than the liquidus temperature of basaltic material at few kbar and is around 1250°C . The two parameters which then remain to be constrained are the half thickness b of the sill and background temperature T_0 . If we remain with a $\frac{1}{2}$ m adcumulate, the sill thickness is constrained by the initial crystal content ϕ_{ci} and is around 18-4m for 1-5% olivine crystals in the melt layer or sill magma. Typically, large layered mafic intrusions intrude at a few kbar depth which equivalent to a background country rock temperature of $300\text{-}550^\circ\text{C}$. Furthermore, the characteristic cumulates are not formed at the very beginning of the formation of a large layered mafic intrusion, hence, it is

plausible that a first series of sills or magma chambers has further heated the surrounding country rocks, possibly leading to background temperatures of 500-700°C or more. At 4-18 m half sill thickness, $T_0 = 400^\circ\text{C}$ leads to characteristic cooling times of 0.5-9.0 years, $T_0 = 550^\circ\text{C}$ to 0.6-12 yrs and $T_0 = 700^\circ\text{C}$ to 0.8-15 yrs. Comparing adcumulate formation times with the characteristic cooling times, the gravitationally driven olivine adcumulate formation appears generally feasible for residual porosities of $\geq 30\%$. For lower residual porosities, larger grain sizes would require thick sills with magmas with either initially low crystal loads or magmas precipitating only a few percent olivine when cooling from liquidus to solidus takes place.

The above calculations only consider single cumulate layers. Alternatively, chemical compaction within a given cumulate layer may continue during deposition and compaction of successive layers. Thus the crystal load and effective stress driving compaction becomes much higher than within a single layer. In this case, the porosity profile across single cumulate layers becomes more homogeneous, and from the porosity gradient within a layer one could derive the height of the cumulate pile leading to compaction of the cumulate layer.

Finally, the total formation time of adcumulates does not simply correspond to the added periods necessary for crystal settling and chemical compaction, as chemical compaction begins as soon as a few layers of crystals are settled. Nevertheless, gravitational crystal settling is about two orders of magnitude faster than chemical compaction and thus becomes negligible for the adcumulate forming process. Similarly, the lithostatic pressure at the bottom of the crystal column increases with increasing compaction, but also this is a second order effect.

V.4 - Crystal settling-floating process in a magma chamber.

The experiments described in chapter IV show a series of crystal settling experiments in a system composed of natural two pyroxene gabbro. The structure and chemical composition of the samples has been described in this previous chapter as well as numerical simulations of hindered sedimentation.

V.4.1 - Structure of centrifuge samples

In the experiments carried out at 1235°C, the samples show a structure in three layers, contrary to the experiment at 1290°C which shows a structure in four layers. This difference between the sample structures could be explained by the centrifugation who allows the separation of two phases due to their density contrast. In fact, this principle is applied not only for crystal-melt separation, but also melt-melt separation in the experiments, which means that the second melt layer having the same density as in the intermediate layer of plagioclases is a product of further melting of plagioclases at temperature 1290°C. In the experiment S6 carried out at 1290°C (Figure IV.1B), two glass layers correspond to two differing densities (Figure. V.4). The vertical variation of melt density through the sample allows to identify that (i) the density of glass 1 is the same that for the experiments done at 1235°C, and (ii) glass layer 2 has the same density as non-melted plagioclase crystals in the intermediate layer. Similar observations have been established with use of chemical compositions (Figure IV.3). Hence, the identification of glass layer compositions is as follows. The first glass layer corresponds to a partial silicate melt with the same composition that in the experiments carried out at 1235°C; the second is composed of melted plagioclases crystals which were non-melted at 1235°C. In a long run experiment these two compositions would be mixed producing a new chemical composition of melt coexisting with crystals. In the centrifuge experiments the duration is too short for the effective chemical diffusion and mixing of two melts. The stratification of two melts according to their density results in a non-mixing phenomenon of two similar silicate melts having doddering density. Another observation drawn from the experiment carried out at 1290°C is that none of plagioclases is trapped in the cumulate layer with magnetite and pyroxene crystals contrary to the experiments carried out at 1235°C. The capturing of light plagioclase crystals in the cumulus layer is a dynamic phenomenon typical for floating-settling of crystals in concentrated suspensions. Clusters of denser crystals sinking down may capture lighter crystals and burry them in the bottom layer. At higher temperature (1290°C) these crystals may be melted and the interstitial liquid escaped into the main melt body in the capsule.

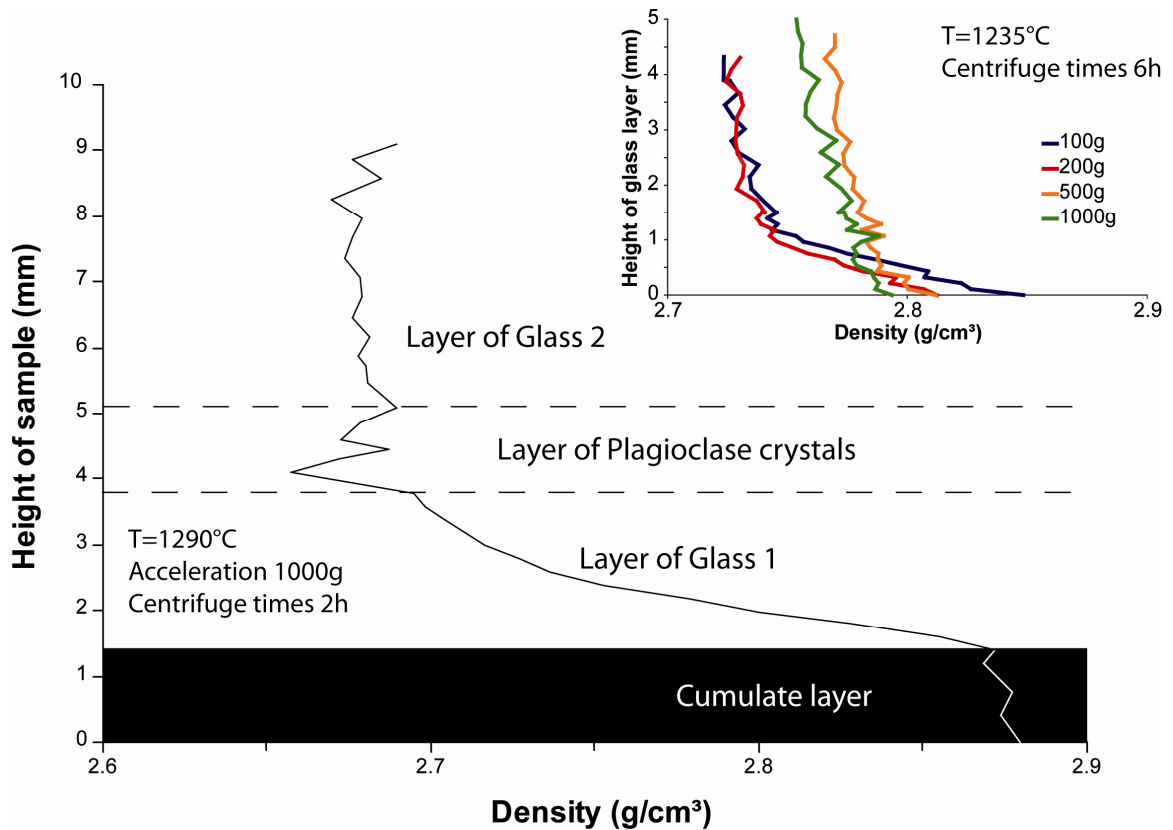


Figure V.4: Figure 10: Density variations along the sample height for experiment at 1290°C. For comparison, in the insert at the top right, the density variation in the glass layer for the experiments conducted at 1235°C with the centrifuge accelerations 100 g, 200 g, 500 g and 1000 g during 6 hours is shown.

V.4.2 - Compositional trends of the major and trace elements concentrations in the glass layer 1.

The vertical distribution of major and trace element concentration in glass layer 1 shows some important variations between the bottom (adjacent to the cumulate layer) and the top of the capsule in experiments at 100 g and 200 g conducted at 1235°C as well as in the experiment at 1000 g and 1290°C (Figure IV.3). In fact, between 0 and 1-2 mm height (depending on the type of oxide), some drastic decreases and increases of concentrations occur and can be explained by several phenomena. The most probable reasons are as follows (i) because of grain boundaries diffusion in cumulate crystals, the melt escaped from this layer is enriched or depleted in some oxides during the compaction. In fact, Dimanov et al. (2000) and Hiraga et al. (2002) have shown that grain boundaries, after separation of melt and crystals, are highly chemically contaminated with the melt phase composition. In order to achieve a significant contamination of grain boundaries by escaping interstitial melt, partially molten rocks require a certain compaction time or in other words the melt escape process should be

slow enough. During compaction the trapped melt is expelled from the bottom layer and move through a crystal pile upward to the top of a cumulate pile. The expelled melt has, as a result of its slow flow, a different composition than the melt which is remained trapped. At high temperature, the mixing of melts occurred if there is sufficient time for fluid flow and diffusion (Sparks and Marshall, 1986). For the experiments at 100 g and 200 g at 1235°C, the time for mixing is not sufficient. The escaping of melt from cumulus layer is slow and continuous. This results significant variations in the vertical concentration profiles of chemical components influencing the density contrast. For example, Al₂O₃ profiles show a concentration of 12 wt% at the part adjacent to the cumulate layer and 14.5 wt% at the top of glassy layer 1. The same is true for FeO, the profiles show a concentration of 14 wt% at the part adjacent to the cumulate layer and 9 wt% at the top of glassy layer 1. For the experiments at 500 g and 1000 g at 1235°C, these variations are not so important along the verticals profiles (i.e. the oxide contents are approximately constant in the melt phase). This may be explained that the compaction and escape of melt from the bottom layer was fast, and the composition of the melt did not change in the course of compaction. The concentration profiles of horizontal distribution demonstrate some noticeable variations of chemical composition only at boundaries with the wall of capsule, which corresponds, either to wall boundary effect or small dissolution of alumina capsule in a course of centrifuge runs.

V.4.3 - Evolution of the compaction

Previously, it was shown that the numerical simulation can reproduce quite adequately the centrifuge experiments, if the hindrance exponent $C=4.7$. It was also numerically established that, in the case of normal gravity, the maximum compaction in a capsule of 10 mm in height is reached after ca. 3 months, which is equivalent to a centrifuged experiment at 365 g during 6 h. However, judging from Figure IV.1, the maximum compaction seems to be reached for experiments carried out at 500g and 1000 g for 6 h. It means that at these high centrifuge experiments the compaction was slower than predicted by numerical experiments with $C=4.7$. One explanation at this difference is that during the centrifuge runs at 500 and 1000 g, light plagioclase crystals are trapped by clusters of the titanomagnetite crystals and deposited in the cumulate layer. This phenomenon can be noted in experiments at 500g and 1000g (Figure IV.1). The plagioclase and titanomagnetite crystals possess differing grain sizes. The

compaction rate in a layer composed of differing size of crystals is slower than for a uniform grain size layer. Hence, the maximum compaction in the experiments at 500 g and 1000 g is reached for a longer duration of centrifuging. This phenomenon may inherent to the constraints of the centrifuge experiments.

V.5 - Comparison with natural examples.

V.5.1 - The Great Kavir

The models described in the chapter II have important implications for the geometry of salt diapir basins such as the Great Kavir Basin (central Iran). In fact, spatially, the model diapirs which ascend from different depths and different positions (experiment 2-4) can be quite close to each other. A similar spatial distribution has been described by Jackson et al. (1990) for salt diapirs the Great Kavir Basin (Figure V.5). As in our experiments, those salt diapirs originate from at least two independent source layers. Rise of salt diapirs in the Great Kavir Basin is probably not controlled extensively by regional structures such as folds and faults, but may rather be controlled by natural perturbations at the surface of the individual salt layers, as well as by the rheology of the overburden sediments. These factors control the rise and the positioning of the PDMS diapirs in our models 2-4.

V.5.2 - The Odenwald Crystalline Complex

In experiment 5 of the chapter II, in which perturbations on top of both PDMS layers were situated directly above each other, the large blue diapir followed its yellow precursor. However, even then, unlike the experiment carried out by Dietl and Koyi (2002), the diapir rising from depth did not ascend exactly along the stem of the upper, yellow diapir, but grew along the broad deformation zone of its precursor. Nevertheless, the resulting diapir-in-diapir structure is very similar to the one in Dietl and Koyi (2002). It is characterized by a very broad, extensive and tabular, mushroom-shaped head. However, in contrast to the nested diapir modelled by Dietl and Koyi (2002), it lacks the slim, well-defined stem and incorporates voluminous overburden material situated between the stems of both nested diapirs (Figure II.8B and C). Moreover, comparison of this experiment 5 with experiment 4 reveals the effect that the positioning of the initial perturbations has on the number of developing diapirs. During

both experiments, four smaller diapirs developed, but the difference between the experiments is that the diapirs growing from the shifted perturbations stay separated in experiment 4, whereas they interact with each other in experiment 5 because the initial position of the perturbations were directly above one another.

One well known and intriguing example of this “nested” diapir is the western part of the the Odenwald Crystalline Complex, Germany, the so called Bergsträßer Odenwald (e.g. Stein, 2001). Here, numerous small and intermediate plutons have intruded simultaneously as nested intrusions (e.g. Dietl and Stein, 2001), separated in places by kilometer-scale screens of schists and amphibolites, which resemble the overburden screens within the composite PDMS diapir in experiment 4 (Figure V.6). Thus, the structures resulting from experiment 5, even if the model is not scaled properly to nature with respect to the viscosity contrast between buoyant material and overburden, reproduces nested, composite and concentrically expanded plutons. Consequently, we assume that these granitoid intrusions form, similar to what we observed in model 5, when individual intrusive batches use the same pathway zones as their precursors for their own ascent and emplacement. From the position of the overburden screens in experiment 5 one could conclude that in the Flasergranitoid Zone the stems of diapiric plutons and not their heads are exposed. As experiments 2-4 showed (as well as the experiment without any perturbation), an offset of perturbations or a lack of perturbations at all results in small, “non-nested” diapirs unlike composite plutons such as the Flasergranitoid Zone.

V.5.3 - The Muskox intrusion

The Muskox intrusion (Canada) is a well documented example of a layered intrusion (Irvine, 1975; 1977), which was mapped by Smith (1962) and Smith et al. (1963). The intrusion has been an object in the numerous subsequent publications (Barnes and Francis, 1995; Day et al., 2008). As well as Skaergaard (Greenland), Bushveld (South Africa), Stillwater (Montana), and Windimura (Australia), the Muskox intrusion is of a great ore deposit interest due to the high concentration of chrome in some specific layers (Barnes and Francis, 1995). The compaction as a dominant mechanism of the cumulate formation in Muskox intrusion has been suggested by

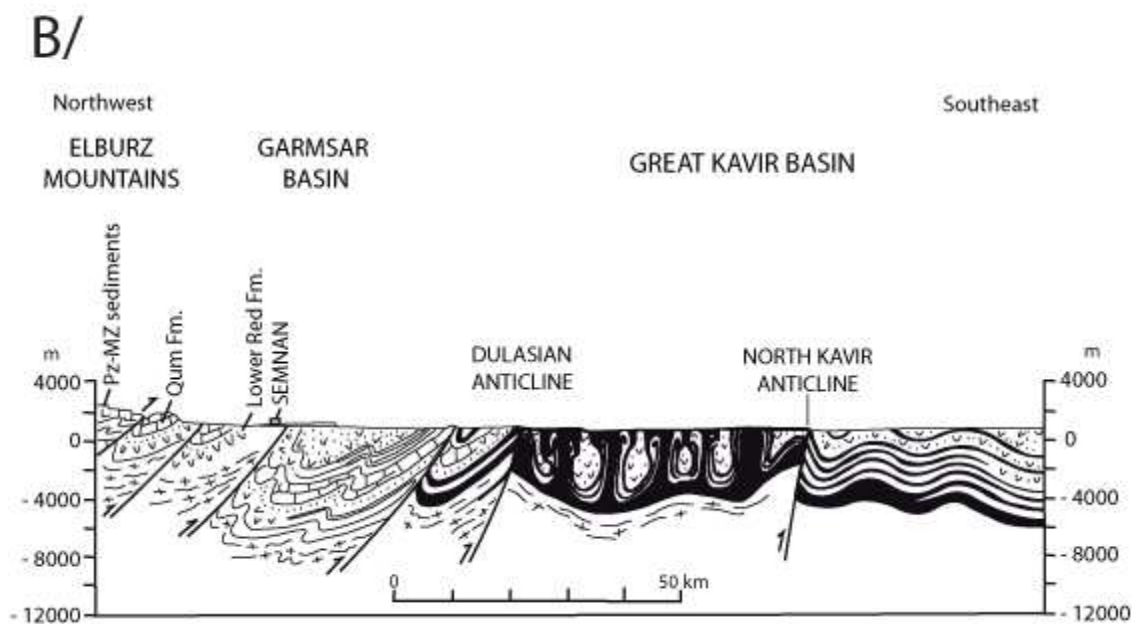
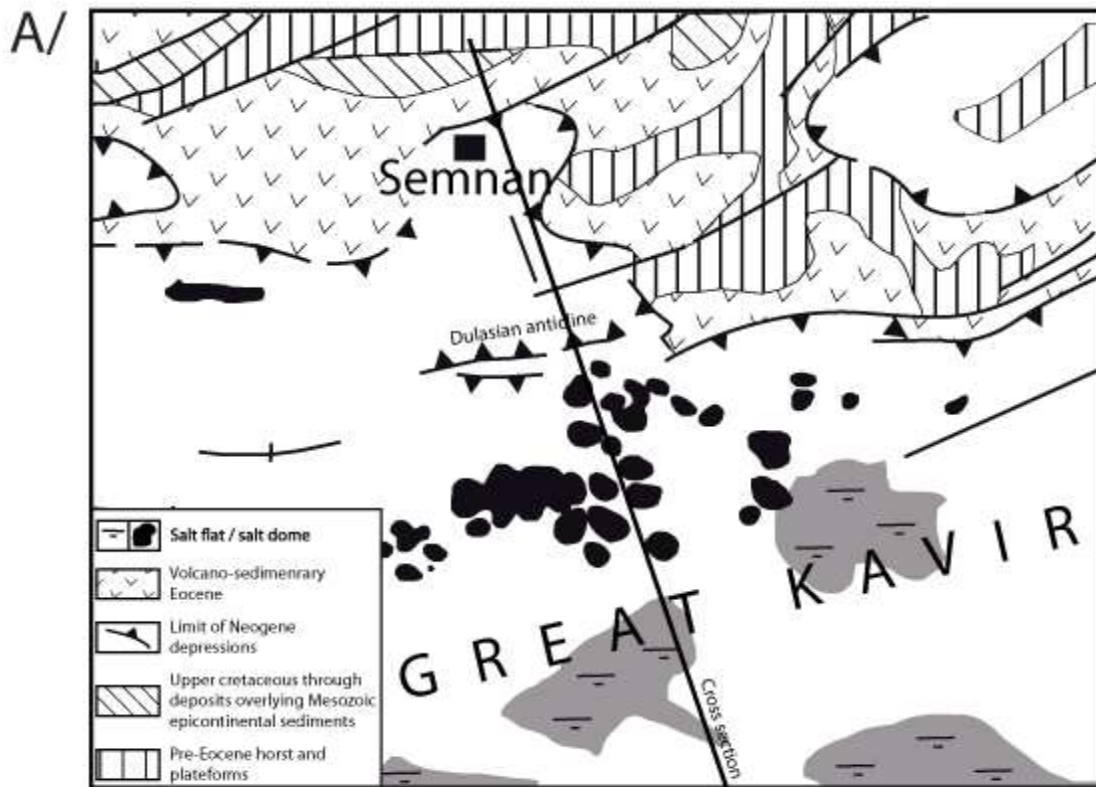


Figure V.5: A/ Tectonic sketch map of the Great Kavir basin and surrounding areas in the Central Iran (redrawn from Jackson, 1990). B/ Schematic cross section across the Great Kavir basin, emphasizing the distribution of salt units (in black).

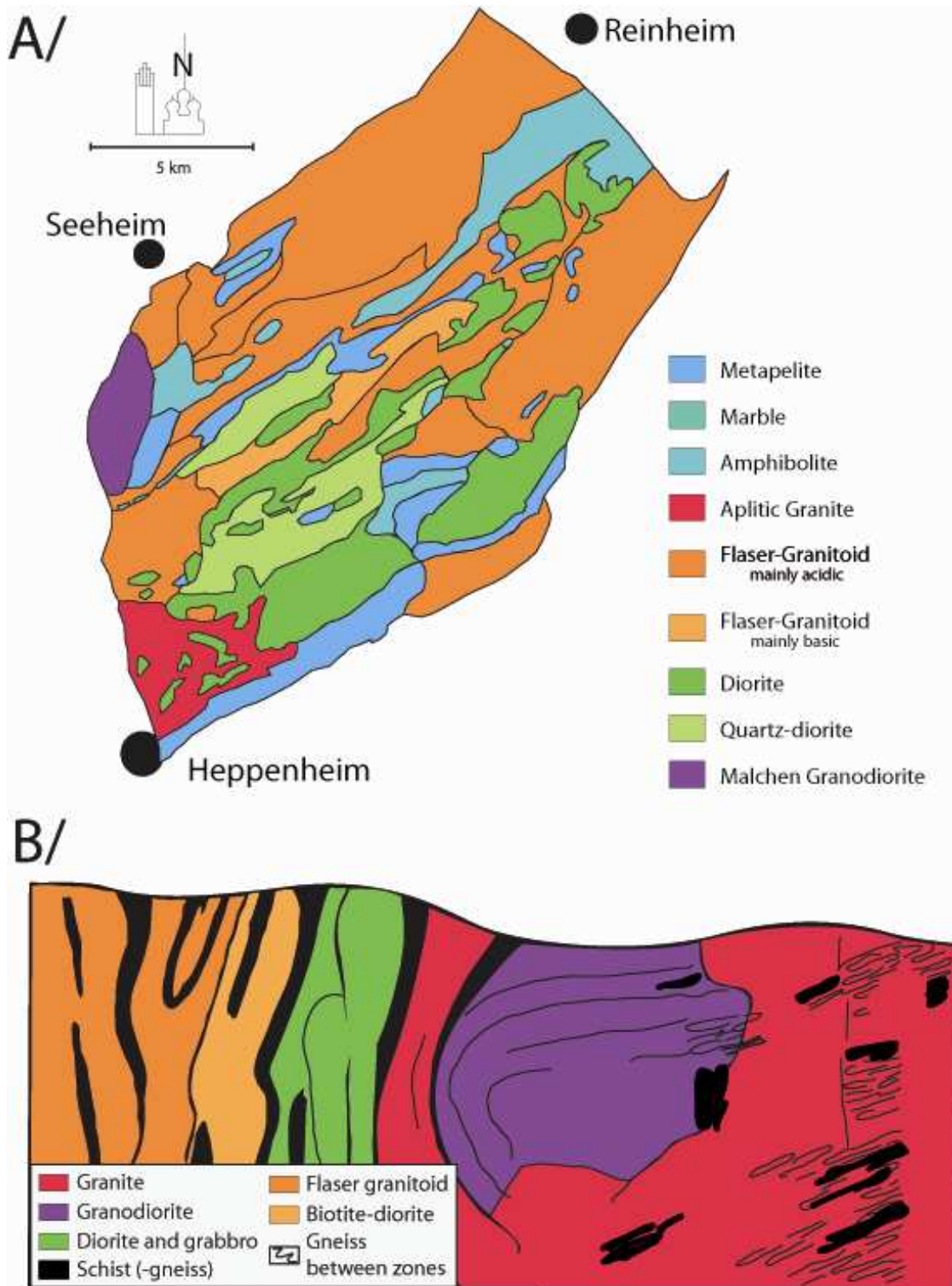


Figure V.6: A. Simplified geological map of the Flaser-granitoid Zone (Odenwald Crystalline Complex Germany, redrawn from Stein, 2001). B. General cross section sketch through the Flaser-granitoid Zone. Thank this cross section and the map view, some similarities are show with our diapir-in-diapir structures in experiment 5 with its rock screens and pendants enclosed within the vast majority of igneous rocks, which may have risen diapirically.

Irvine (1980). The model suggested by Shirley (1986) corresponds to Irvine's (1980) arguments that the rest fraction of the trapped interstitial melt in Muskox intrusion results from the last stage compaction of the crystal-melt mushy zone. Tharp et al (1998) developed a sophisticated numerical model for the compaction mechanism of olivine cumulates by incorporating simultaneously acting grain boundary diffusion creep and power law creep.

Using the numerical program described in the section IV.3, the time for the maximum compaction in Muskox intrusion using the hindered sedimentation mechanism has been estimated. From Irvine (1980) the estimated initial and residual melt fractions are 0.6 and 0.2, and these values have been used in numerical modeling. The density of crystals has been taken 2950 kg/cm^3 . The magma density and crystal size were taken from Irvine as 2700 kg/cm^3 and 0.3 mm, respectively. The viscosity used in calculations is 8 Pa.s (corresponding to 1272°C) which was calculated from chemical composition of melt by using the method of Bottinga and Weill (1972).

Using the numerical model of hindered sedimentation the evolution of the porosity decrease in a bottom layer with the thickness 1800 m (equal to the thickness of Muskox intrusion) has been calculated (Figure V.7). The results of numerical simulation demonstrated a distribution of porosity in cumulates as a function of the elapsed time. In order to compare the results of this study with the results obtained by Tharp (1998), the initial porosity has been taken 0.6 and the numerical simulation is stopped after 3000 years. The simulation with the use of hindered sedimentation mechanism demonstrates an exponential loss of porosity as a function of the elapsed time in cumulus layer, whereas the results of Tharp (1998) indicate on a linear decrease of porosity with time. Tharp's (1998) simulation considers the loss of porosity occurring due to compaction and precipitation. In the model here, the rate of porosity decrease with time is not constant. During the first 1000 years there is an important loss of porosity and at this stage the dominant process is the hindered sedimentation of crystals. Later, the thickness change of cumulus layer due to the compaction mechanism overwhelms the sedimentation mechanism. However, Tharp's (1998) model suggests that the volumetric fractions of liquid and crystals are both functions of temperature. In the model of hindered sedimentation, the temperature is not taken constant, and the sedimentation velocity is a function of a local crystal fraction.

Tharp (1998) adopts the equation presented by Irvine (1970) to model a deposition rate of cumulates:

$$X_{cum} = 2k_{cr} \Delta T t^{1/2} / \left[H \rho_{xl} (1 - \phi_i) (\pi k_{cr} / \rho_{cr} c_{cr})^{1/2} \right] \quad (\text{Eq. V.11})$$

where X_{cum} is the thickness of cumulate pile presented as a function of cooling time t . The constants k_{cr} , ρ_{cr} and c_{cr} are the thermal conductivity, density and heat capacity of the country rocks, ρ_{xl} is density of cumulates crystals, ϕ_i is initial porosity of the cumulates (melt fraction) and ΔT is the initial temperature difference between magma and country rocks. Eq. (V.11) may be simplified as $X_{cum} = \alpha t^{1/2}$, where α^2 is the effective temperature diffusion coefficient. Tharp (1998) has found that $\alpha = 42.4 \text{ m yr}^{-1/2}$ for the Muskox intrusion, it is cooled from one side. However, Eq. (V.11) assumes a deposition of crystal on a magma chamber floor with the same area as magma chamber roof. This is not the case for Muskox. This implies that a deposition rates in the lower part of intrusion, where the depositional surface is smaller in area, may exceed the calculated rate predicted by Eq. (V.11). Tharp et al. (1998) assumes that the whole intrusion accumulated at a rate twice that calculated from Eq. (V.11). Hence, $\alpha = 84.8 \text{ m yr}^{-1/2}$. The initial porosity is taken 60% and the critical packing of crystals is taken 20%. The porosity in the bottom layer as a function of time has been fitted to the time decay exponent $\phi = 0.4e^{-0.002^*t} + 0.2$, where time is in years (Figure V.7). The effective accumulation rate $(1800) * (0.002)^{0.5}$ has been estimated $80.5 \text{ m yr}^{-1/2}$, which is in agreement with that one found by Tharp et al. (1998).

The distribution of crystals in the cumulate layer calculated for different time steps is shown in Figure V.8. The diagram illustrates the porosity evolution along the intrusion height. In this simulation, the maximum crystallinity 0.8 or minimum porosity 0.2 is reached after 3000 years. This is in agreement with the calculations of Tharp (1998). This result differs significantly from the minimum cooling time 7000 years estimated by Irvine (1970) for Muskox intrusion. The present calculations demonstrate that the effect of hindered sedimentation of the thickness growth of cumulus layer is larger than compaction at the initial stage of intrusion cooling.

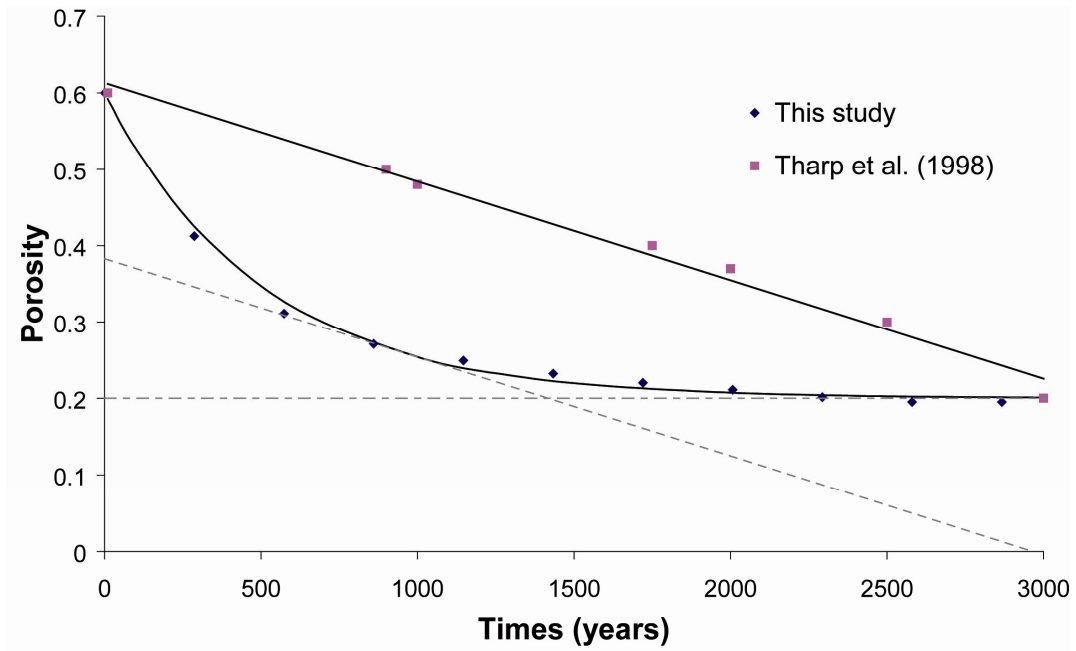


Figure V.7: Porosity loss in Muskox intrusion. The porosity in the bottom layer decreases linear with time according to Tharp's (1998) cooling-compaction model. According to the present calculations for the hindered sedimentation an exponential decrease of porosity in the bottom layer is expected ($\phi = 0.4e^{-0.002*t} + 0.2$). The straight line corresponds to the time moment when the rate of porosity decrease from hindered sedimentation is equal to the rate of porosity decrease from compaction. The intersection of this straight line with the horizontal axe defines the time, when the critical porosity in the bottom layer will be reached by combining hindered sedimentation and compaction models.

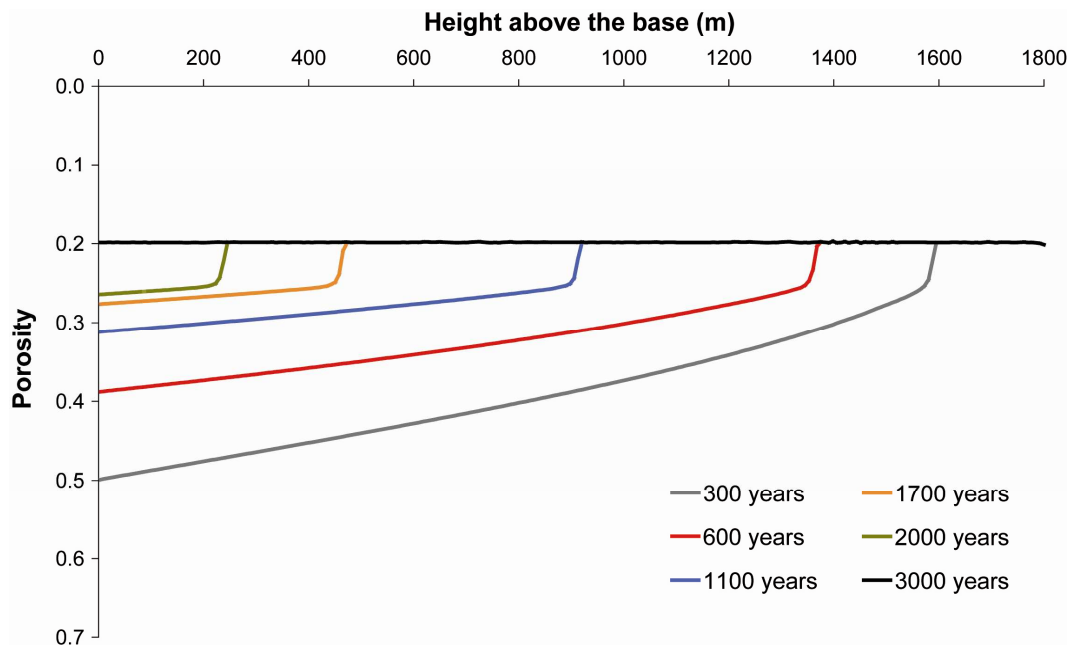


Figure V.8: Variations of porosity along the height of Muskox intrusion calculated from hindered sedimentation model with C=4.7.

Conclusion

The melt segregation from a solid matrix in the upper mantle is the first step in the formation of magmas. Mechanisms of melt segregation proposed in the literature are based on two different physical models: percolation of interstitial melt driven by a density difference between melt and matrix, associated with compaction and deformation of the matrix (McKenzie, 1984); or the suction of interstitial melt into fractures from a surrounding porous matrix (Nicolas and Jackson, 1982; Ribe, 1986; Sleep, 1988). The ability of granitic melt to segregate mechanically from its matrix is strongly dependent on its physical properties, among which viscosity and density are the most important. In numerous experiments it was established that viscosity of silicate melt is a strong function of composition, temperature and water content (Dingwell et al., 1993). With the help of different centrifuge experiments presented in this thesis, we have tried to better understand these mechanisms, especially crystal settling and compaction processes. The crystal-settling mechanism has been investigated in the chapter IV. The experiments show that during compaction, the melt composition evolved due to different processes: (i) dynamic dissolution of crystals during their movement, and (ii) expulsion of trapped melt in cumulus layer of crystals during pressure-solution processes. During the first stage of the compaction, the melt is separated in two zones, which have different chemical compositions and densities. This means that both zones have different viscosities, which results in layering inside a magma chamber. This layering could have a strong influence on the segregation and extraction mechanism of trapped melt in cumulus layer. However, this layering is not permanent in time. In fact, when the maximum compaction is reached, a homogenization of the melt composition in liquid phase is observed due to diffusion process. The second stage of hindered crystal settling or simultaneous settling and compaction mechanisms have been studied through the centrifuge experiments in the Chapter III. The conclusion of this study show that the settling velocity is fast and that mechanical settling alone of olivine yields crystal fractions not more than 0.48. The chemical compaction resulting from the lithostatic pressure in the crystal pile that is larger than the hydraulic pressure in the magma, is a mechanism of compaction which yields feasible time scales for a linear grain size dependence.

The magma ascent is provided by gravity, which is still the most viable driving force for large-scale vertical transport of melt in the continental crust. However, the traditional idea of buoyant granitic magma ascending through the continental crust may explain only slow-rising, models of hot Stokes diapirs or models of stopping of diapirs have been largely replaced by models involving the ascent of granitic magmas in narrow conduits, either as a self-propagating dykes (Clemens and Mawer, 1992; Clemens et al., 1997) along pre-existing faults (Petford, 1993) or as an interconnected network of active shear zones and dilational structures (D'Lemos, 1993; Collins and Sawyer, 1996). The emplacement of granitic magma within the continental crust marks the final stage in the granite forming process. Emplacement is defined here as the switch from preferably upward to horizontal flow, and it is controlled by a combination of mechanical interactions (either pre-existing or emplacement-generated wall rock structures), and density effects between the spreading flow and its surroundings (Hogan and Gilbert, 1995; Hutton, 1988). This final emplacement of granitic magma has been investigated in this thesis in the Chapter II. The conclusion may be formulated as follows, in the case of simultaneous ascending diapirs from different depths and positions, each diapir took a separate pathway and did not use the route taken by the diapir above to reach the surface. However, when the both protrusions are located above each other, the lower diapir grows along the broad deformation zone of its precursor and incorporates a lot of material of overburden units within it and forms a diapir-in-diapir structure.

From this work we may see that the centrifuge is a necessary tool to model structures whose formation is driven by gravity. In fact, by substituting the gravitational field through the radial centrifugal field, the centrifuge increases the density contrast between two materials and, hence, decreases the time necessary to complete processes under natural conditions. The conclusions of the three studies are formulated more in details below.

1. In the study on simultaneous ascending diapirs from different depths and positions, the analogue modeling shows clearly that each diapir took a separate pathway and did not use the route taken by the diapir above to reach the surface. Some experiments (experiment 2 to 4) give some clues to the formation of salt domes which originate from a basin with multiple salt

horizons as the Great Kavir Basin (Iran). The study shows also, that when both the protrusions were situated above each other, the lower diapir grows along the broad deformation zone of its precursor and incorporates a lot of material of overburden units within it and forms a diapir-in-diapir structure which looks very similar to the one achieved by Dietl and Koyi (2002). The diapir-in-diapir structure resembles the Flasergranitoid Zone within the Odenwald Crystalline Complex with its host rock screens and pendants enclosed within the vast majority of igneous rocks, which may have risen diapirically. During the different steps of the rise, multiple diapirs cause the overburden units to deform ductily. This results in the formation of rim synclines. The degree of deformation of overburden depends on the number of diapirs formed and, therefore, is related to the contrast of viscosity between PDMS and overburden units. A possibility for future work on these nested diapirs is to take into account the rheological modifications due to temperature variations during their rise and emplacement in the crust. For that, the construction of a thermo-mechanical model is necessary, but unfortunately, the centrifuge required to carry out this kind of experiments does not exist yet.

From the experiments on olivine crystal compaction in cumulus layer, four conclusions are drawn.

2. The settling velocity for a dense suspension with an olivine fraction of 0.34 is about 1/6 of the Stokes' velocity. For example, for an olivine with grain size of 5 mm, the suspension velocity will be approximately of 22 cm/h.
3. The "pure" mechanical settling of olivine yields maximum crystal fractions of 0.48.
4. Chemical compaction resulted from lithostatic pressure in the crystal pile of cumulus crystals which is larger than the hydrostatic pressure in magma, drives the mechanism of compaction which yields feasible time scales for a linear grain size increase in cumulus layers. In this case, the prevailing process of compaction is the dissolution of olivine at grain boundary contacts and precipitation of olivine on pore walls.
5. A typical formation times of ½ m thick olivine layer with 25-30% porosity at its basis is from 4 months to 3 years, which is a realistic time scale when it is

compared with a characteristic cooling times of magma sills of appropriate thickness. For crystal settling and compaction experiments, further future work is needed. For example, to conceive experiments in a deformation apparatus, like a Paterson press, in order to observe behaviour of crystals during their settling under conditions of deformation. Another way would be to perform the first step, static experiments, for a longer duration (~ weeks) in order to identify the role of deformation and the stability of the melt network in the olivine aggregates.

From the experiments and modeling of hindered crystal settling-floating process in a magma chamber, four conclusions are drawn:

6. The centrifuge experiments permit to calibrate numerical models and help to constraint some physical parameters which are difficult to access in normal gravity experiments. For example, in this study, centrifuge modeling and numerical simulation of hindered sedimentation highlighted the evolution of crystal-melt separation with time. The experiments at different compaction rates (differing centrifuge acceleration) have allowed to observe a spatial distribution of major and minor oxides in the silicate liquid and permit to derive the hindrance exponent $C=4.7$ for sedimentation velocity of concentrated suspension.
7. The experiments show that during compaction, the melt composition evolved due to different processes: (i) dynamic dissolution of crystals during their floating-settling; and (ii) expulsion of trapped melt from cumulus layer of crystals during increase of pressure due to the growing weight of overlying crystal pile. The layering in the top and bottom area has a strong influence on the segregation and extraction mechanism of trapped melt in cumulus layer. However, this layering is not permanent in time. In fact, when the maximum compaction is reached, a homogenization of the melt composition in liquid phase may be also observed due to diffusion process.
8. The evolution of the melt composition has also been studied through the increase of a partial melting degree by conducting the centrifuge experiments at two differing temperatures. The experiment at higher temperature and higher degree of partial melting has revealed the fact that the melt could be

separate in two liquids: one has the same chemical composition than that which has been obtained at lower temperature; the second melt composition has the same composition and density as non-melted plagioclase crystals from the experiment at lower temperature. A stepwise character of silicate melt evolution during separation of crystals and melt due to hindered sedimentation and dynamic dissolution of crystals in magma chambers should be considered in future as a potentially significant mechanism of the chemical stratification.

9. The numerical simulation has been applied to the Muskox intrusion. The results on the time formation of the intrusion as well as the porosity loss with time are in agreement with previous results of the compaction model (Tharp et al., 1998). The present results obtained with the use of hindered sedimentation model demonstrate an exponential decrease of cumulus layer porosity with time due to vanishing sedimentation velocity at high crystal concentrations. This last observation implies that the hindered sedimentation is the dominant mechanism of the porosity loss until an almost dense packing of crystals in cumulus is reached. The compaction is a prevailing mechanism for the porosity loss only at the last stage of cumulus formation. Assuming that at this stage the temperature decreases significantly, variations of cumulus layer thickness due to compaction alone may not be rather significant.

References

- Akaad, M. K., 1956a. The Ardara granitic diapir of County Donegal, Ireland. Geological Society of London Quarterly Journal, 112: 263-288.
- Akaad, M. K., 1956b. The northern aureole of the Ardara pluton of County Donegal. Geological Magazine, 93: 377-392.
- Akatsuka, T., Obata, M. and Yokose, H., 1999. Formation of layered structure in the Murotomisaki gabbroic complex, especially picrite gabbro, Kochi prefecture, Japan - qualitative evaluation of crystal accumulation. Journal of Geological Society of Japan, 105: 771-788 (in Japanese with English abstract).
- Allen, C.M., 1992. A nested diapir model for the reversely zoned Turtle pluton, southeastern California. Transactions of the Royal Society of Edinburgh, 83: 179-190.
- Alpert, L., 2006. Emplacement of three plutons by nested diapirism and stopping in Cactus Flat, San Bernardino County, Southern California. PhD Thesis. University of California, Los Angeles.
- Angevine, C.L. and Turcotte, D.L., 1983. Porosity reduction by pressure solution: A theoretical model for quartz arenites. Geological Society American Bulletin, 94: 1129-1134.
- Bagdassarov, N.S., A.M. Dorfman and D.B. Dingwell, 1996. Modeling of melt segregation processes by high-temperature centrifuging of partially molten granites - I. Melt extraction by compaction and deformation. Geophysical Journal International, 127: 616-626.
- Bagdassarov, N.S., A.M. Dorfman and D.B. Dingwell, 1996. Modeling of melt segregation processes by high-temperature centrifuging of partially molten granites - II. Rayleigh-Taylor instability and sedimentation. Geophysical Journal International, 127: 627-634.

- Barnes S.-J. and Francis D., 1995. The distribution of platinum-group elements, nickel, copper, and gold in the Muskox layered intrusion, Northwest Territories, Canada, *Economic Geology*, 90: 135-154.
- Basson, D.K., S. Berres and R. Bürger, 2009. On models of polydisperse sedimentation with particle-size-specific hindered-settling factors. *Applied Mathematical Modeling* 33: 1815-1835.
- Bateman, R.J., 1983. Structure, petrology and emplacement processes of the Cannibal Creek, Queensland. Ph. D. thesis, James Cook University of North Queensland (unpublished.). pp. 1-129.
- Bateman, R.J., 1985. Aureole deformation by flattening around a diapir during in-situ ballooning: the Cannibal Creek Granite. *Journal of Geology*, 93: 293-310.
- Bedard J.H.J., B.D. Marsh, T.G Hersum, H.R.Naslund and S.B Mukasa, 2007. Large-scale mechanical redistribution of orthopyroxene and plagioclase in the basement sill, ferrar dolerites, McMurdo Dry Valleys, Antarctica: Petrological, mineral-chemical and field evidence for channelized movement of crystals and melt. *Journal of Petrology*, 48 (12): 2289-2326.
- Berres S., R. Bürger and A. Kozakevicius, 2009. Numerical approximation of oscillatory solutions of hyperbolic-elliptic systems of conservation laws by multiresolution schemes. *Advances in Applied Mathematics and Mechanics*, 1: 581-614.
- Berres S., R. Bürger, K.H. Karlsen and E.M Tory, 2003. Strongly degenerate parabolic-hyperbolic systems modeling polydisperse sedimentation with compression. *SIAM Journal on Applied Mathematics*, 64 (1): 41-80.
- Berres, S. and R. Bürger, 2008. On the settling of a bidisperse suspension with particles having different sizes and densities, *Acta Mechanica*, 201 (1-4): 47-62
- Bishop, R. S., 1978. Mechanism for emplacement of piercement diapirs. *American Association of Petroleum Geologists Bulletin*, 62: 1561-1583.

- Bohlen, S.R., Essene, E.J. and Boettcher, A.J., 1980. Reinvestigations and applications of olivine-quartz-orthopyroxene barometry. *Earth and Planetary Science Letters*, 47: 1-10.
- Bose, K. and Ganguly, J., 1995. Quartz-coesite revisited: reversed experimental determinations at 500-1000°C and retrieved thermochemical properties. *American Mineralogist*, 80: 231-238.
- Bottinga, Y. and Weill, D.F., 1972. The viscosity of magmatic silicate liquids: a model for calculation. *American Journal of science*, 272: 438-475.
- Bottinga, Y., D. Weill and P. Richet, 1982. Density calculations for silicate liquids. I. Revised method for aluminosilicate compositions. *Geochimica et Cosmochimica Acta*, 46: 909-919.
- Botto, L., Narayanan, C., Fulgosi, M. and Lakehal, D., 2005. Effect of near-wall turbulence enhancement on the mechanisms of particle deposition. *International Journal of Multiphase Flow*, 31: 940-956.
- Boudreau, A. E. and McBirney, A. R., 1997. The Skaergaard layered series. Part III. Non-dynamic layering. *Journal of Petrology*, 38: 1003-1020.
- Bucky, B.P., 1931. The use of models for the study of mining problems, Technical Publication, American Institute of Mining Engineers, 425: 28.
- Bürger R. and A. Kozakevicius, 2007. Adaptive multiresolution WENO schemes for multi-species kinematic flow models. *Journal of Computational Physics*, 224: pp. 1190-1222.
- Bürger, R., K.H. Karlsen, E.M. Tory and W.L. Wendland, 2002. Model equations and instability regions for the sedimentation of polydisperse suspensions of spheres. *Zeitschrift für Angewandte Mathematik und Mechanik*, 82 (10): 699-722
- Cabane H., Laporte D. and Provost A., 2005. An experimental study of Ostwald ripening of olivine and plagioclase in silicate melts: implications for the growth and size of crystals in magmas. *Contributions to Mineralogy and Petrology*, 150: 37-53.

- Campbell I. H., P. L. Roeder and J. M. Dixon, 1978. Plagioclase buoyancy in basaltic liquids as determined with a centrifuge furnace. *Contributions of Mineralogy and Petrology*, 97: 369-377.
- Campbell, I. H., Naldrett, A. J., and Barnes, S. J., 1983. A model for the origin of the platinum-rich sulfide horizons in the Bushveld and Stillwater Complexes. *Journal of Petrology* , 24: 133-165.
- Castro, A., 1987, On granitoid emplacement and related structures: A review: *Geologische Rundschau*, 76: 101–124.
- Chen C.F. and Turner J.S., 1980. Crystallization in a double-diffusive convective system. *Journal of Geophysical Research*, 85: 2573–2593.
- Chipman, J., 1926. The Soret effect. *Journal of the American Chemical Society*, 48: 2577-2589.
- Clemens, J. D. and Mawer, C. K., 1992. Granitic magma transport by fracture propagation. *Tectonophysics*, 204: 339– 360.
- Clemens, J. D., Petford, N. and Mawer, C. K., 1997. *In* Deformation-Enhanced Fluid Transport in the Earth's Crust and Mantle (ed. Holness, M.) 145–172.
- Cobbold, P.R. and Jackson, M.P.A., 1992. Gum rosin (colophony); a suitable material for thermomechanical modeling of the lithosphere. *Tectonophysics*, 210: 255-271
- Collins, W. J and Sawyer, E. W., 1996. Pervasive granitoid magma transport through the lower-middle crust during non-coaxial compressional deformation. *Journal of Metamorphic Geology*, 14: 565– 579.
- Connolly, J.A.D. and Podladchikov, Y.Y., 2000. Temperature-dependent viscoelastic compaction and compartmentalization in sedimentary basins. *Tectonophysics*, 324 : 137-168.
- Connolly, J.A.D., Schmidt, M.W., Solferino, G., Bagdassarov, N., 2009. Permeability of asthenospheric mantle and melt extraction rates at mid-ocean ridges. *Nature*, 462: 209-212.

- Conrad, M.E. and Naslund H.R., 1989. Modally-graded rhythmic layering in the Skaergaard intrusion. *Journal of Petrology*, 30: 251-269
- Coulomb, C.A., 1776. Essai sur une application des règles des maximis et minimis a quelques problèmes de statique relatifs à l'architecture. *Mémoires de l'Académie Royale pres Divers Savants*, Vol. 7.
- Cruden A.R., Koji H., Schmeling H., 1995. Diapiric basal entrainment of mafic into felsic magma. *Earth and Planetary Science Letters*, 131: 321-340.
- Cygan, R.T. and Carrigan, C.R., 1992. Time-dependent Soret transport-Applications to brina and magma. *Chemical Geology*, 95: 201-212.
- Davy, P., and Cobbold, P.R., 1991. Experiments on shortening of a 4-layer model of the continental lithosphere. *Tectonophysics*, 188: 1-25.
- Day, J.M.D., Pearson, D.G. and L.J. Hulbert, 2008. Rhenium–osmium isotope and platinum-group element constraints on the origin and evolution of the 1.27 Ga Muskox layered intrusion. *Journal of Petrology*, 49 (7): 1255–1295
- Detloff, T. and D. Lerche, 2008. Centrifugal separation in tube and disc geometries: experiments and theoretical models. *Acta Mechanica*, 201: 83–94.
- Detloff, T., T. Sobisch and D. Lerche, 2007. Particle size distribution by space or time dependent extinction profiles obtained by analytical centrifugation (concentrated systems). *Powder Technology*, 174: 50–55.
- Dietl, C. and Koyi, H.A., 2002. Emplacement of nested diapirs: results of centrifuge modeling. In: Schellart, W. P. and Passchier, C. 2002, *Analogue modeling of large-scale tectonic processes*. *Journal of the Virtual Explorer*, 6: 81-88.
- Dietl, C. and Longo, A., 2007. Thermal aureole around the Joshua Flat – Beer Creek Pluton (California) requires multiple magma pulses: constraints from thermobarometry, infra-red spectroscopy and numerical modeling. *Geotectonic Research*, 95: 13-40.
- Dietl, C. and Stein E., 2001. The diapiric emplacement and related magmatic fabrics of the porphyritic Ludwigshöhe granite, Central Odenwald (Germany). *Mineralogy and Petrology*, 72: 185-207.

- Dimanov A., R. Wirth and G. Dresen, 2000. The effect of melt distribution on the rheology of plagioclase rocks. *Tectonophysics*, 328: 307-327.
- Dingwell D., Bagdassarov N., Bussod G., Webb S. L., 1993. *Magma Rheology*. Mineralogical Association of Canada, Short Course on Experiments at High Pressure and Applications to the Earth's Mantle, 131–196.
- Dixon, J.M., 1974. A new method of determining finite strain in models of geological structures. *Tectonophysics*, 24: 99-114.
- Dixon, J.M., 1975. Finite strain and progressive deformation in models of diapiric structures. *Tectonophysics*, 28: 89-124.
- Dixon, J.M., and Summers, J.M., 1985. Recent developments in centrifuge modeling of tectonic processes; equipment, model construction techniques and rheology of model materials, *Journal of Structural Geology*. 7: 83-102.
- D'Lemos, R. S., Brown, M. and Strachan, R. A., 1993. Granite magma generation, ascent and emplacement within a transpressional orogen. *Journal of the Geological Society London*, 149: 487–490.
- Doie, M. and Edwards S. F., 1978. Dynamics of concentrated polymer systems. Part 4. Rheological properties. *Journal of the Chemical Society, Faraday Transactions articles II.*, 74: 1802–1817.
- Dorfman A., Dingwell D.B. and Bagdassarov N.S., 1997. A rotating autoclave for centrifuge studies: Falling sphere viscometry. *European Journal of Mineralogy*, 9: 345-350.
- Eaton, J..P. and Murata, K.J., 1960. How volcanoes grow. *Science*, 132(3432): 925-938.
- Fowler, A.C. and Yang, X., 1999. Pressure solution and viscous compaction in sedimentary basins. *Journal of Geophysical Research B*, 104: 12989-12997.
- Gasquet D., Fernandez A., Mahé C. and Boullier A.M., 1995. Origine des rubanements dans les granitoïdes : exemple du monzogranite de Brignogan-Plouescat (NW du Massif armoricain), *Comptes Rendus de l'Académie des Sciences Series 2*, 321 : 369–376.

- Giordano D., J. K. Russel and D.B. Dingwell, 2008. Viscosity of magmatic liquids: A model. *Earth and Planetary Science Letters*, 271: 123 – 134.
- Goode, A.D.T., 1976. Small scale primary cumulus igneous layering in the Kalka layered intrusion, Giles Complex, central Australia. *Journal of Petrology* 17, 379-397
- Hanitzsch, E. and Kalhweit, M., 1969. Zur Umlösung aufgedampfter Metallkristalle, II. *Zeitschrift für Physikalische Chemie*, 65: 290–305
- Hibbard, M.J., 1987. Deformation of incompletely crystallized magma systems: granitic gneisses and their tectonic implications. *Journal of Geology*, 95: 543–561.
- Hillert, M, 1965. On the theory of normal and abnormal grain growth. *Acta Metallurgica*, 13: 227–238.
- Hiriga T., M. Anderson, M. E. Zimmerman, S. Mei and D. L. Kohlstedt, 2002. Structure and chemistry of the grain boundaries in deformed, olivine + basalt and partially molten lherzolite aggregates: evidence of the melt-free grain boundaries. *Contributions of Mineralogy and Petrology*, 144: 163-175.
- Hladil, J., M. Ruzička and L. Koptíková, 2006. Stromatactis cavities in sediments and the role of coarse-grained accessories. *Bulletin of Geosciences* 81 (2): 123-146
- Hogan, J. P. and Gilbert, M. C., 1995. The A-type Mount Scott granite sheet: importance of crustal magma traps. *Journal of Geophysical Research*. 100: 15799–15792.
- Holder, M. T. 1979. An emplacement mechanism for post tectonic granites and its implications for their geochemical feature. In: Atherton, M. P., and Tarney, J. (Eds.), *Origin of the Granite Batholiths. Geochemical Evidence*, Shiva, Orphington, Kent, United Kingdom, pp. 116-128.
- Holder, M. T., 1981. Some aspects of intrusion by ballooning: The Ardara pluton (abstract). In: Coward, M. P. (Eds.), *Diapirism and Gravity tectonics: Report of a Tectonic Studies Group Conference held at Leeds University, 25–26 March 1980*. *Journal of Structural Geology*, 3, pp. 93.

- Holness, M.B, Cheadle, M.J. and McKenzie, D., 2005. On the Use of Changes in Dihedral Angle to Decode Late-stage Textural Evolution in Cumulates. *Journal of Petrology*, 46 (8): 1565–1583.
- Horsfield, W., 1977. An experimental approach to basement-controlled faulting. *Geologie en Mijnbouw*, 56: 363-370
- Hort, M., Marsh, B.D. and Spohn, T., 1993. An oscillatory nucleation model for igneous layering. *Contributions to Mineralogy and Petrology*, 114: 425-440
- Hoshida, T., Obata, M. and Akatsuka, T., 2006. Crystal settling and crystal growth of olivine in magmatic differentiation - the Murotomisaki Gabbroic Complex, Shikoku, Japan. *Journal of Mineralogical and Petrological Sciences*, 101: 223-239.
- Hubbert, M.K., 1937. Theory of scale models as applied to the study of geologic structures. *Geological Society of America Bulletin*, 48: 1459-1520
- Hubbert, M.K., 1951. Mechanical basis for certain familiar geologic structures. *Geological Society of America Bulletin*, 62: 355-372.
- Huppert, H.E. and Sparks, R.S.J., 1984. Double - diffusion convection due to crystallization in magmas. *Annual Review of Earth and Planetary Sciences*, 12: 11.
- Hutton, D. H. W., 1988. Granite emplacement mechanisms and tectonic controls: inferences from deformation studies. *Transactions of the Royal Society of Edinburgh: Earth and Environmental Science*, 79: 245–255.
- Irvine, T. N., 1975. Crystallisation sequences in the Muskox intrusion and other layered intrusions-II. Origin of chromitite layers and similar deposits of magmatic ores. *Geochimica et Cosmochimica Acta* , 39: 991-1020.
- Irvine, T. N., 1977. Origin of chromitite layers in the Muskox intrusion: A new interpretation. *Geology* , 5: 273-277.
- Irvine, T.N., 1980. Magmatic infiltration metasomatism, double-diffusive fractional crystallization, and cumulative growth in the Muskox intrusion and other layered intrusions. In: R.B. Hargraves, Editor, *Physics of Magmatic Processes*, Princeton University Press, Princeton, N.J, pp. 325–384.

- Irvine, T.N., 1987. Layering and related structures in the Duke Island and Skaegaard intrusions: Similarities, differences, and origins. In: *Origins of Igneous Layering*, edited by Ian Parsons. Series C: Mathematical and Physical Sciences, 196: 666 p.
- Irvine, T.N., Keith, D.W. and Todd, S.G., 1983. The J-M platinum-palladium Reef of the Stillwater Complex, Montana: II. Origin by double-diffusive convective magma mixing and implications for the Bushveld Complex. *Economic Geology*, 78:1287–1334
- Ismail-Zadeh, A.T., Huppert, H. E. and Lister, J. R., 2001. Analytical modeling of viscous diapirism through a strongly non-Newtonian overburden subject to horizontal forces. *Journal of Geodynamics*, 31, 5: 447-458.
- Jackson, M. P. A., Cornelius, R. R., Craig, C. H., Gansser, A., Stocklin, K., and Talbot, C. J., 1990. Salt Diapirs of the Great Kavir, Central Iran. *Geological Society of America, Memoir 177*, pp. 140
- Jaupart, C. and Tait, S., 1995. Dynamics of differentiation in magma reservoirs, *Journal of Geophysical Research*, 100: 17615–17636.
- Kadik, A.A., E.B. Lebedev, A.M. Dorfman and N.S. Bagdasarov, 1989. Simulation of Crystal-Magma Separation in a Centrifuge. *Geochemistry International*, 26 (8): pp. 39–48.
- Kadik, A.A., Lebedev, E.B. and Dorfman. A.M., 1989. Modeling of separation process of magmatic melts from crystals using high-temperature centrifuge. *Geokhimiya*, 1: 43-54
- Kerr, R.C. and Turner, J.S., 1982. Layered convection and crystal layers in multicomponent systems. *Nature*, 298: 731–733.
- King, R. F., 1966. Magnetic fabric of the some Irish granite. *Geological Journal*, 5: 43-66.
- Koyi, H., 1988. Experimental modeling of role of gravity and lateral shortening in Zagros mountain belt, *AAPG Bulletin*, 72: 1381-1394.
- Koyi, H., 1997. Analogue modeling; from a qualitative to a quantitative technique; a historical outline, *Journal of Petroleum Geology*, 20: 223-238.

- Koyi, H.A. and Skelton, A., 2001. Centrifuge modeling of the evolution of low-angle detachment faults from high-angle normal faults, *Journal of Structural Geology*, 23: 1179-1185.
- Kukowski, N. and Neugebauer, H.J., 1990. On the ascent and emplacement of granitoid magma bodies—dynamic-thermal numerical models. *Geologische Rundschau.*, 79: 227-239.
- Kuritani T., T. Yokoyama and E. Nakamura, 2007. Rates of thermal and chemical evolution of magmas in a cooling magma chamber: A chronological and theoretical study on basaltic and andesitic lavas from Rishiri Volcano, Japan. *Journal of Petrology*, 48 (7): 1295-1319.
- Lange, R.L. and Carmichael, I.S.E., 1990. Thermodynamic properties of silicate liquids with emphasis on density, thermal expansion and compressibility. *Reviews in Mineralogy*, 24: 25 -64.
- Langmuir, C. H., 1989. Geochemical consequences of in situ crystallization. *Nature*, 340: 199–205.
- Lesher, C.E. and Walker, D., 1988. Cumulate maturation and melt migration in a temperature gradient. *Journal of Geophysical Research*, 93: 10295-10311.
- Lifshitz, I.M, and Slyozov, V.V., 1961. The kinetics of precipitation from supersaturated solid solutions. *Journal of Physics and Chemistry of Solids*, 19: 35–50
- Lister, J.R. and Kerr, R.C., 1991. Fluid-mechanical models of crack propagation and their application to magma-transport in dykes. *Journal of Geophysical Research*, 96: 10049-10077.
- Liu, S. and Dixon, J.M., 1991. Centrifuge modeling of thrust faulting; structural variation along strike in fold-thrust belts, *Tectonophysics*, 188: 39-62.
- Longo A., Vassalli M., Papale P. and Barsanti M., 2006. Numerical simulation of convection and mixing in magma chambers replenished with CO₂-rich magma. *Geophysical Research Letters*, 33, L21305: 6.

- Lucas, S.B. and St-Onge, M.R., 1995. Syn-tectonic magmatism and the development of compositional layering, Ungava Orogen (northern Québec, Canada). *Journal of Structural Geology*, 17: 475–491.
- McBirney A. R. and Murase, T., 1984. Rheological Properties of Magmas. *Annual Review of Earth and Planetary Sciences*, 12: 337-357.
- McBirney A. R. and Noyes R. M., 1979. Crystallization and layering of the Skaergaard Intrusion. *Journal of Petrology*, 20: 487–564.
- McBirney A. R., 1980. Mixing and unmixing of magmas. *Journal of Volcanology and Geothermal Research*, 7: 357-371.
- McBirney, A.R. and Nicolas, A., 1997. The Skaergaard Layered Series. Part II. Magmatic flow and dynamic layering. *Journal of Petrology*, 38: 569–580
- McKenzie, D., 1984. The Generation and Compaction of Partially Molten Rock. *Journal of Petrology*, 25: 713–765
- Meier, M. and G. H. Frischat, 1993. A high temperature centrifuge method to study ion exchange in glass melts avoiding convective processes. *Physics and Chemistry of Glasses*, 34: 71–76.
- Miller, C.F., Watson, M.E. and Harrison, T.M. 1988. Perspectives on the source, segregation and transport of granitoid magmas. *Royal Society of Edinburgh: Earth Sciences*, 79: 135–156.
- Molyneux, S.J. and Hutton, D.H.W, 2000. Evidence for significant granite space creation by the ballooning mechanism; the example of the Ardara Pluton, Ireland. *Geological Society of America Bulletin*, 112: 1543–1558.
- Montanari, D., Corti, G. and Simakin, A., 2010. Magma chambers and localization of deformation during thrusting. *Terra Nova*, 22: 390–395.
- Naslund H. R. and McBirney A. R., 1996. Mechanisms of formation of igneous layering. In: *Layered Intrusions - Cawthorn R. G., ed., Amsterdam Elsevier: 1-43.*
- Nelson, C. A., Oertel, G., Christie, J. M., and Sylvester, A. G., 1978. Geologic map of the Papoose Flat pluton, Inyo Mountains, California, with palinspastic map and

cross sections. Geological Society of America, Map sheet, MC-20, scale 1:32,000, 3 sheets.

Nelson, C.A., 1987. Papoose Flat pluton, Inyo Mountains, California: Boulder, Colorado. Geological Society of America, Centennial Field Guide, Cordilleran Section, 1: 157–160.

Nicolas, A. and Jackson, M., 1982. High temperature dikes in peridotites: Origin by hydraulic fracturing. *Journal of Petrology*, 23: 568–582.

Parsons I ed: *Origins of Igneous Layering*. NATO ASI Series, Reidel Publishing Co, Dordrecht: 287-312.

Paterson S. R. and Vernon R. H., 1995. Bursting the bubble of ballooning plutons: a return to nested diapirs emplaced by multiple processes. *Geological Society of America Bulletin*, 107: 1356-1380.

Petford, N., 1996. Dykes and diapirs? *Royal Society of Edinburgh, Earth Sciences*, 87: 105-114.

Petford, N., Kerr, R. C. and Lister, J. R., 1993. Dike transport of granitoid magmas. *Geology*, 21: 845–848.

Pitcher, W. S. and Berger, A. R., 1972. *The Geology of Donegal: A Study of Granite Emplacement and Unroofing*. In: Wiley-Interscience, London, pp. 435.

Ramberg, H., 1967. Model experimentation of the effect of gravity on tectonic processes, *The Geophysical Journal of the Royal Astronomical Society*, 14: 307-329.

Ramberg, H., 1970. Model studies in relation to intrusion of plutonic bodies, in *Mechanism of igneous intrusion*, edited by G. Newall, and N. Rast, pp. 261-286.

Ramberg, H., 1981. *Gravity, Deformation and the Earth's Crust (2nd Edition)*. Academic Press, London, pp. 452.

Ramsay, J. G., 1989. Emplacement kinematics of a granite diapir: The Chindamora batholith, Zimbabwe. *Journal of Structural Geology*, 11: 191-209.

- Ribe N. M., 1986. Melt segregation driven by dynamic forcing. *Geophysical Research Letters*, 13:1462-1465.
- Richard, P., 1991. Experiments on faulting in a two-layered cover sequence overlying a reactivated basement fault with oblique-slip. *Journal of Structural Geology*, 13: 459-469.
- Richardson, J.F. and W. N. Zaki, 1954. Sedimentation and fluidization: Part I. *Transactions of the Institution of Chemical Engineers (London)*, 32: 35–53.
- Robins, B., Haukvik, L. and Jansen, S. 1987. The organization and internal structure of cyclic units in the Honningsvåg intrusive suite, North Norway: implications for intrusive mechanisms, double-diffusive convection and pore-magma infiltration. In: Parsons I ed: *Origins of Igneous Layering*. NATO ASI Series, Reidel Publishing Co, Dordrecht: 287-312.
- Roeder, P.L. and Dixon, J.M., 1977. A centrifuge furnace for separating phases at high temperature in experimental petrology. *Canadian Journal of Earth Sciences*, 14: 1077-1084.
- Römer, M. and Neugebauer, H., 1991. The salt dome problem: a multilayered approach. *Journal of Geophysical Research*, 96: 2389–2396
- Sanderson D.J. and Meneilly A.W., 1981. Analysis of three-dimensional strain modified uniform distributions: andalusite fabrics from a granite aureole. *Journal of Structural Geology*, 3: 109–116.
- Schmeling H., 1987. On the relation between initial conditions and late stages of Rayleigh-Taylor instabilities. *Tectonophysics*, 133: 65–80.
- Schmidt, M.W., Connolly, J.A.D., Günter, D. and Bogaerts, M., 2006. Element Partitioning: The Role of Melt Structure and Composition. *Science*, 312: 1646-1650.
- Schwindinger, K.R., 1999. Particle dynamics and aggregation of crystals in a magma chamber with application to Kilauea Iki olivines. *Journal of Volcanology and Geothermal Research*, 88: 209-238.

- Shaw, H. R., 1972. Viscosities of magmatic silicate liquids: an empirical method of prediction. *American Journal of Science*, 272: 870-893.
- Shemenda, A.I., 1983. Similarity criteria in mechanical modeling of tectonic processes. *Soviet Geology and Geophysics*, 24: 8-16.
- Shimizu, L., 1995. Kinetics of pressure solution creep in quartz. *Tectonophysics*, 245: 121-134.
- Shirley, D.N., 1986. Compaction of igneous cumulates. *Journal of Geology*, 94: 795-809.
- Simura, R. and K. Ozawa, 2006. Mechanism of crystal redistribution in a sheet-like magma body: Constraints from the Nosappumisaki and other shoshonite intrusions in the Nemuro peninsula, Northern Japan. *Journal of Petrology*, 47 (9): 1809-1851.
- Sleep N. H., 1988. Tapping of melt by veins and dikes. *Journal of Geophysical Research*, 93:10255-10272
- Smith, C. H., 1962. Notes on the Muskox intrusion, Coppermine River area, District of Mackenzie, Geological Survey of Canada, Papers; 61-25:1-16.
- Smith, C. H., Irvine, T.N. and Findlay, D.C., 1963. Geology of the Muskox intrusion. Geological Survey of Canada, Maps: 1213A-1214A.
- Sparks, R. S. J. and L. A. Marshall, 1986. Thermal and mechanical constraints on mixing between mafic and silicic magmas. *Journal of Volcanology and Geothermal Research*, 29: 99 – 124.
- Spera, F.J., 1980. Aspects of magma transport. In: Hargraves, RB (Eds.), *Physics of magmatic processes*. Princeton University Press, 265-324.
- Stein, E., 2001. The geology of the Odenwald Crystalline Complex. *Mineralogy and Petrology*, 72: 7-28.
- Stokes, G.G., 1851. On the effects of the internal friction on the motion pendulumus. *Transaction of Cambridge Philosophical Society*, 9 (2): 8-106.

- Sylvester, A. G., Oertel, G., Nelson, C.A. and Christie, J.M., 1978. Papoose Flat pluton: a granitic blister in the Inyo Mountains, eastern California. *Geological Society of America Bulletin*, 89: 1205-1219
- Tada, R. and Siever, R., 1989. Pressure solution during diagenesis. *Annual Reviews of Earth and Planetary Science*, 17: 89-118.
- Talbot, C.J., 1977. Inclined and asymmetric upward-moving gravity structures, *Tectonophysics*, 42: 159-181.
- Tatum, J.A., Finnis, M.V., Lawson, N.J. and Harrison, G.M., 2005. 3-D particle image velocimetry of the flow field around a sphere sedimenting near a wall Part 2. Effects of distance from the wall. *Journal of Non-Newtonian Fluid Mechanics*, 127: 95-106.
- Tharp, T. M., Loucks, R.R. and Sack, R. O., 1998. Modeling compaction of olivine cumulates in the Muskox intrusion. *American Journal of Science*, 298:758-790.
- Tomkins, M. R., Baldock T. E. and Nielsen, P., 2005. Hindered settling of sand grains, *Sedimentology*, 52: 1425-1432.
- Tory, E.M. and Pickard, D.K., 1977. A three-parameter Markov model for sedimentation. *Canadian Journal of Chemical Engineering*, 55: 655-665.
- Tory, E.M. and Pickard, D.K., 1986. Experimental evidence for a stochastic approach to sedimentation. In: B.M. Moudgil, P. Somasundaran (Eds.), *Flocculation, Sedimentation and Consolidation*. AIChE, NY, The Cloister, Sea Island, GA Jan 27–Feb 1, 1985: 297–306.
- Turcotte, D.L. and Schubert, G., 1982. *Geodynamics: application of continuum physics to geological problems*, 450 pp., John Wiley & Sons.
- Wager, L. R., 1959. Differing powers of crystal nucleation as a factor producing diversity in layered igneous intrusions. *Geological Magazine*, 96:75-80.
- Wager, L. R., Brown, G.M. and Wadsworth, W.J., 1960. Types of Igneous Cumulates. *Journal of Petrology*, 1: 73-85.

- Wager, L.R. and Brown, G.M., 1968. Layered Igneous Rock. Edited by Oliver and Boyd, Edinburgh and London, p. 588
- Wagner, C., 1961. Theorie der Alterung von Niederschlägen durch Umlösen. *Zeitschrift für Elektrochemie*, 65: 581–591
- Weijermars, R. and Schmeling, H., 1986. Scaling of Newtonian and non-Newtonian fluid dynamics without inertia for quantitative modeling of rock flow due to gravity (including the concept of rheological similarity). *Physics of the Earth and Planetary Interiors* 43: 316–330.
- Weinberg, R.F. and Podladchikov, Y., 1994. Diapiric Ascent of Magmas through Power-Law Crust and Mantle. *Journal of Geophysical Research-Solid Earth*, 99 (B5): 9543-9559.
- Weinberg, R.F. and Podladchikov, Y., 1995. The rise of the solid-state diapirs. *Journal of Structural Geology*, 17 (8): 1183-1195.
- Wiebe, R. A., 1988. Structural and magmatic evolution of a magma chamber: the Newark Island layered intrusion, Nain, Labrador. *Journal of Petrology*, 29: 383-411.
- Wilkinson, D. S., and Ashby, M. F., 1975. Pressure sintering by power law creep. *Acta Metallurgica* 23(11): 1277 -1285.
- Wilson J.R. and Larsen S.B., 1985. Two-dimensional study of a layered intrusion: the Hyllingen Series. Norway. *Geological Magazine*, 122: 97- 124.
- Wilson, J.R., Menuge, J.F., Pedersen, S. and Engell-Sorensen, O., 1987. The southern part of the Fongen-Hyllingen layered mafic complex, Norway: emplacement and crystallization of compositionally stratified magma. In: Parsons I ed: *Origins of Igneous Layering*. NATO ASI Series, Reidel Publishing Co, Dordrecht: 145-184.
- Woidt, W.-D., 1978. Finite element calculations applied to salt dome analysis. *Tectonophysics*, 50: 369–386
- Yang, X., 2000. Pressure solution in sedimentary basins: effect of temperature gradient. *Earth and Planetary Science Letters*, 176: 233-243.

Yang, X., 2001. Density driven compactional flow in porous media. *Journal of Computational and Applied Mathematics*, 130: 245-257



LEBENS LAUF

Mélanie Forien

Institut für Meteorologie und Geophysik
J.-W. Goethe Universität Frankfurt
Altehöferallee 1
60438 Frankfurt a. Main, Germany

Tel.: +49(0)69-79840116

Fax: +49(0)69-79840131

Email: forien@geophysik.uni-frankfurt.de

PERSÖNLICHE DATEN

Geburtsdatum/-ort: 20. Januar 1984 in Gien, Frankreich

Nationalität: Französisch

Familienstand: ledig

Heimatadresse: Untergasse 4, D-61184 Karben

Email: melforien@hotmail.com

SCHULAUSSBILDUNG

1995 – 1999 Grundschule „La Sologne“, Tigy, Frankreich

1999 – 2002 Gymnasium „Voltaire“, Orléans, Frankreich; Abschluss: Abitur

STUDIUM

2002 – 2005 Geologie, Université Orléans, Frankreich
Abschluss: licence (Bachelor) Geologie
Diplomarbeitsthema: Strurgeologie, Prospektion (Metalle), organische und anorganische Chemie, Biologie, Mineralogie

2005 – 2007 Geologie, Université Orléans, Frankreich
Abschluss: Master Geologie
Diplomarbeitsthema: Thermodynamik und Kinetik von geochemischen Prozessen, Geodynamik der Erdkruste mit einer Fallstudie, Vulkanologie und Magmen Dynamik

2007– laufend Geologie, Goethe Universität, Frankfurt am Main, Deutschland
Abschluss: Promotion

Diplomarbeitsthema: „From melt segregation to pluton emplacement: centrifuge experiments concerning magmatic systems“

ARBEITSERFAHRUNG

15.08.04 – 15.09.04 Praktikum

Bureau de Recherches Geologique et Minière (BRGM), Cayenne, Frankreich

01.04.05 – 29.04.05 Praktikum

Norisko Environnement, Orléans, Frankreich

09.05.06 – 30.09.06 Praktikum

Institut des Sciences de la Terre d'Orléans (ISTO), Orléans, Frankreich

SONSTINGES

Freundsprachen: Französisch – Muttersprache

English – gut

Deutsch – Grundlagen

Führerschein (2002) Klasse 3

ZUSÄTZLICHE QUALIFIKATIONEN

- Sehr gute EDV- Kenntnisse in Office, Adobe Illustrator, Photoshop, Golden Software Grapher, GIMP, SPO2003, ImageJ

Erfahrung an wissenschaftlichen Großgeräten:

- Paterson Press. Institut des Sciences de la Terre d'Orléans (ISTO), Orléans, Frankreich
- Single stage centrifuging piston cylinder. Institut für Mineralogie und Petrologie, ETH Zürich, Schweiz.
- End-loaded piston cylinder press. Institut für Mineralogie und Petrologie, ETH Zürich, Schweiz.
- Scanning Electron Microprobe (JEOL JSM 6400). Institut des Sciences de la Terre d'Orléans (ISTO), Orléans, Frankreich
- Scanning Electron Microprobe. Institut für Meteorologie und Geophysik, Goethe University, Deutschland.

PUBLIKATIONEN

Publizierte Artikel in internationalen Zeitschriften:

Forien, M. and C. Dietl (2009). Simultaneously ascending diapirs from different depths and different positions: a centrifuge study. *Geotectonic Research*, vol. 96:39-52.

Eingereichte Publikationen in internationalen Zeitschriften:

Forien, M., Berres, S., Bagdassarov, N., Dingwell, D. und Dorfman A.(2010). Crystal-melt settling in a magma-chamber. Submitted to *Physics of the Earth and Planetary Interiors*.

Forien, M., Arbaret, L., Burgisser, A. and Champallier, R. (2010). Experimental study of crystal fragmentation in concentrated magmatic suspensions. In preparation to *Journal of Volcanology and Geothermal Research*.

Forien, M., Schmidt, M. W., Solferino, G. und Bagdassarov, N. (2010). Olivine settling and compaction in basaltic magma and time scales of cumulate formation. In preparation for *Physics of the Earth and Planetary Interiors*

Veröffentliche Abstracts in internationalen Zeitschriften:

Forien, M. and C. Dietl (2009). Simultaneously ascending diapirs from different depths and different positions: a centrifuge study. *Geotectonic Research*, 95, Special Issue 1, p. 187.

Beiträge auf internationalen Tagungen

Forien, M., Arbaret, L., Burgisser, A. and Champallier, R. (2008). Experimental study of intragranular fracturing in concentrated magmatic suspensions (oral Präsentation). 12th Symposium "Tektonik, Struktur- und Kristallingeologie", 2. -4. April 2008, Karlsruhe, Deutschland.

Forien, M., Arbaret, L., Burgisser, A. and Champallier, R. (2008). Experimental constrains on crystal fragmentation in deformed concentrated magmatic suspensions (oral Präsentation). European Geosciences Union, General Assembly, 13 – 18 April 2008, Vienna, Österreich.

G. Solferino, M.W. Schmidt, N. Bagdassarov, **M. Forien** (2008). The settling and compaction of olivine from basaltic melt: a centrifuge study on cumulate formation (Oral Präsentation). Experimental Mineralogy Petrology Geochemistry XII, 8-10 September 2008, Innsbruck, Österreich.

Forien, M. and Dietl, C. (2008). Simultaneously ascending diapirs from different depths and different positions: a centrifuge study. Geodynamics Workshop, 30.September – 02.Oktober 2008, Neustadt a.d. Weinstraße, Deutschland.

Forien, M. and Dietl, C. (2009). Simultaneously ascending diapirs from different depths and different positions: a centrifuge study. European Geosciences Union, General Assembly, 19 – 24 April 2008, Vienna, Österreich

Forien, M. Bagdassarov, N. und Schmidt, M. W. (2009). Compaction of olivine in basaltic melt. Conférence Internationale sur la Lithosphère (ILP Joint Task Force Meeting), 5 – 9 Oktober 2009, Clermont-Ferrand, Frankreich.

- Forien, M.** Bagdassarov, N. und Schmidt, M. W. (2009). Experimental constraints of the olivine crystals compaction in cumulus layer. AGU Fall meeting, 14 – 18 Dezember 2009, San Francisco, USA.
- Forien, M.**, Berres S. und Bagdassarov, N. (2010). Crystal sedimentation: analogue and numerical modeling. New Advances in Geophysics Meeting, 11 – 12 Februar 2010, London, England.
- Forien, M.** Dietl, C. und Koyi. H. (2010). Interactions between pre-existing plutons and their host rocks during shortening: a centrifuge study. 13th Symposium “Tektonik, Struktur- und Kristallingeologie”, 6. -9. April 2010, Frankfurt am Main, Deutschland.
- Forien, M.**, Berres S. und Bagdassarov N. (2010). Model of crystal settling in a magma chamber. Experimental Mineralogy Petrology Geochemistry XIII, 12 – 14 April 2010, Toulouse, Frankreich.
- Forien, M.**, Arbaret, L., Burgisser, A. and Champallier, R. (2010). Experimental constrains on crystal fragmentation in deformed concentrated magmatic suspensions (oral Präsentation). Experimental Mineralogy Petrology Geochemistry XIII, 12 – 14 April 2010, Toulouse, Frankreich.

Seminare

- Forien, M.** and Dietl, C. (2008). Simultaneously ascending diapirs from different depths and different positions: a centrifuge study. Presented at the Institute of Earth Sciences by University of Frankfurt am Main, Germany, the 25th November 2008
- Forien, M.**, Arbaret, L., Burgisser, A. and Champallier, R. (2007). Presented at the Institute of Earth Sciences by University of Frankfurt am Main, Germany, the 27th November 2007